AD-A077 336 PENNSYLVANIA STATE UNIV UNIVERSITY PARK ORDNANCE RES--ETC F/G 20/4
MEASUREMENT OF TIME-DEPENDENT PROPELLER THRUST AND CORRELATION --ETC(U)
JUL 72 D E THOMPSON N00017-70-C-1407
UNCLASSIFIED TM-72-116 NL

1 OF 2
AD-
A077336

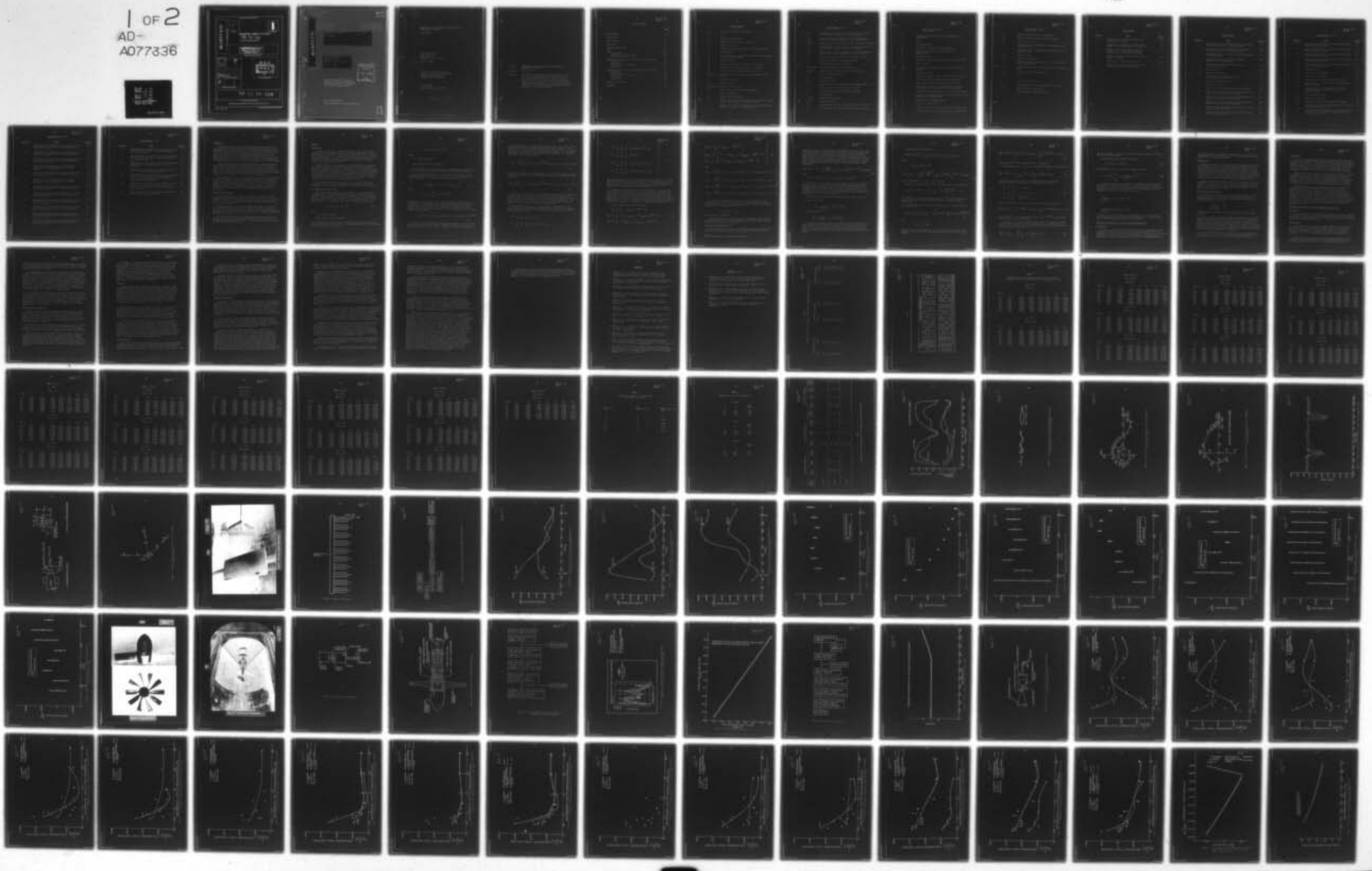

PHOTOGRAPH THIS SHEET

AD A077336

DTIC ACCESSION NUMBER

II

LEVEL

[redacted]

INVENTORY

Contract No. N00017-70-C-1407

TM-72-116

DOCUMENT IDENTIFICATION

DISTRIBUTION STATEMENT A
Approved for public release;
Distribution Unlimited

DISTRIBUTION STATEMENT

ACCESSION FOR		
NTIS	GRA&I	☒
DTIC	TAB	☐
UNANNOUNCED		☐
JUSTIFICATION		
BY		
DISTRIBUTION /		
AVAILABILITY CODES		
DIST	AVAIL AND/OR SPECIAL	
A		

DISTRIBUTION STAMP

DDC
RECEIVED
NOV 29 1979
D

DATE ACCESSIONED

79 11 23 533

DATE RECEIVED IN DTIC

PHOTOGRAPH THIS SHEET AND RETURN TO DTIC-DDA-2

DTIC FORM OCT 79 70A

DOCUMENT PROCESSING SHEET

MEASUREMENT OF TIME-DEPENDENT PROPELLER THRUST AND CORRELATION WITH THEORY

D. E. Thompson

Technical Memorandum
File No. TM 72-116
July 10, 1972
Contract No. N00017-70-C-1407

Copy No. 64

The Pennsylvania State University
Institute for Science and Engineering
APPLIED RESEARCH LABORATORY
University Park, Pennsylvania

NAVY DEPARTMENT

NAVAL ORDNANCE SYSTEMS COMMAND

MEASUREMENT OF TIME-DEPENDENT PROPELLER THRUST AND CORRELATION WITH THEORY

D. E. Thompson

Technical Memorandum
File No. TM 72-116
July 10, 1972
Contract No. N00017-70-C-1407

Copy No. 64

The Pennsylvania State University
Institute for Science and Engineering
ORDNANCE RESEARCH LABORATORY
University Park, Pennsylvania

NAVY DEPARTMENT

NAVAL ORDNANCE SYSTEMS COMMAND

Subject: Measurement of Time-Dependent Propeller Thrust and Correlation With Theory

References: See Page 30

Abstract:

The blade-rate time-dependent thrust generated by a two-, five-, and ten-bladed propeller operating in the wake shed by a strut has been measured for a range of propeller operating conditions. Predictions of the time-dependent thrust have been made based on two theoretical approaches; a two-dimensional strip theory, and a lifting surface theory. Comparisons of the predicted values and measured values of time-dependent thrust have been made.

TABLE OF CONTENTS

LIST OF SYMBOLS

A_n	real part of n^{th} Fourier coefficient
a	Ω/U
B	number of propeller blades
B_n	imaginary part of n^{th} Fourier coefficient
b	semi-chord of airfoil
b_j	semi-chord of propeller blade at the j^{th} spanwise element
C_L	lift coefficient
C_{nj}	n^{th} complex Fourier coefficient of the inflow to the propeller at the j^{th} spanwise element
D_p	propeller diameter
$\tilde{F}_x$	unsteady transverse force generated by the propeller
$\tilde{F}_y$	unsteady transverse force generated by the propeller
$\tilde{F}_z$	unsteady axial force generated by the propeller
$f_m(q,\phi_\alpha)$	function which results from separating ϕ_α from the kernel function
J	advance ratio, V_∞/ND_p
$K(k)$	Sears' function
$K(r,\phi_o;\rho,\theta_o;q)$	kernel of integral equation
$\overline{K}(\quad)$	kernel after θ_α-integration and ϕ_α-integration
k	reduced frequency, $\omega b/U$
k_{nj}	reduced frequency, nNb_j/U_{Rj}
L_u	unsteady lift on an airfoil operating in a sinusoidally varying velocity field parallel to the airfoil's surface
L_v	unsteady lift on an airfoil operating in a sinusoidally varying velocity field normal to the airfoil's surface

LIST OF SYMBOLS (Cont'd)

$\tilde{L}_{nj}$	unsteady lift on the j^{th} element of a propeller blade due to the n^{th} harmonic component of the propeller inflow
$\tilde{L}_{\ell jn}$	unsteady lift on the j^{th} element of the ℓ^{th} propeller blade due to the n^{th} harmonic component of the propeller inflow
$\tilde{L}^{(\bar{n})}(\rho)$	spanwise loading components (coefficients of Birnbaum distribution)
$\tilde{M}_{nj}$	unsteady moment on the j^{th} element of a propeller blade due to the n^{th} harmonic component of the propeller inflow
$\tilde{M}_{\ell jn}$	unsteady moment on the j^{th} element of the ℓ^{th} propeller blade due to the n^{th} harmonic component of the propeller inflow
N	propeller rotational frequency in revolutions per second
n	order of the harmonic of the propeller inflow
P	number of spanwise elements per blade
$\Delta P(\xi,\rho,\theta_o)$	perturbation pressure at the loading point
$Q_{m-1/2}(\ \ )$	Legendre spherical function of half odd-integer order
q	order of blade harmonic, ω/Ω
R	Descartes distance
R_{tip}	propeller tip radius
r	radial coordinate in cylindrical polar coordinate system
r_j	radial location of the j^{th} spanwise blade element
Δr_j	spanwise extent of the j^{th} spanwise blade element
S	lifting surface
$S(\rho,\theta_o)$	blade loading distribution
$T(k)$	Horlock's function
$\tilde{T}_x$	unsteady moment about the x-axis generated by the propeller
$\tilde{T}_y$	unsteady moment about the y-axis generated by the propeller

LIST OF SYMBOLS (Cont'd)

$\tilde{T}_z$	unsteady moment about the z-axis (torque) generated by the propeller
t	time
U	free-stream velocity
U_L	local steady velocity in the axial direction
U_{Rj}	resultant steady velocity at the j^{th} element of a propeller blade
U_∞	free-stream velocity
u_o	amplitude of unsteady velocity parallel to airfoil's surface
V_a	speed of advance
$V_N^n(r)$	known amplitude of relative velocity normal to helicoidal surface
V_∞	free-stream velocity
W	amplitude of unsteady velocity normal to airfoil's surface
χ	axial coordinate in cylindrical polar coordinate system
α	steady angle of attack measured from zero lift line
α_j	steady angle of attack at the j^{th} element of a propeller blade measured from the zero lift line of that section
β	one-half of the spanwise extent of a typical spanwise element
β_j	angle between resultant velocity vector and rotational velocity vector at the j^{th} blade element
η_ℓ	phase angle due to blade separation
Θ	$\overline{\theta}_n + \theta_o - \phi_o - a(\tau - \chi + \xi)$
θ	angular coordinate in the cylindrical polar coordinate system
θ_o	initial angular position of loading point in propeller plane

LIST OF SYMBOLS (Cont'd)

θ_α	angular chordwise location of loading point
θ_b	projected propeller semi-chord length, in radians
$\overline{\theta}_n$	$2\pi(n-1)/N;\ n = 1,2,\ldots N$
ξ	axial coordinate of loading point in the cylindrical polar coordinate system
ρ	radial coordinate of loading point in the cylindrical polar coordinate system
ρ_f	density of fluid
τ,τ'	variables of integration
ϕ	angular coordinate of the control point in the cylindrical polar coordinate system
ϕ_o	initial angular position of the control point in the propeller plane
ϕ_j	phase angle of the j^{th} blade element
$\phi_{\ell j}$	$\psi_j + \eta_\ell$
χ	$[\Theta - \overline{\theta}_n + \phi_o - \theta_o]/a - (\chi - \xi)$
ψ_j	phase angle of the j^{th} blade element due to blade skew
Ω	angular velocity of the propeller
ω	angular frequency of the blade loading

LIST OF TABLES

LIST OF FIGURES

LIST OF FIGURES (Cont'd)

LIST OF FIGURES (Cont'd)

LIST OF FIGURES (Cont'd)

INTRODUCTION

Propeller-induced ship vibrations have become increasingly important in recent years due to the increased size and horsepower per shaft of new ships. Ship vibrations are caused by the vector sums of several time-dependent forces and moments which are due to the operation of the propeller in the wake of the ship. The components of the vector sums of the time-dependent forces and moments may be thought of as (1) those transmitted by the bearings of the propeller shaft which are due to time-dependent propeller loads, and (2) those transmitted by the hull near the propeller, by bossings, and by appendages near the propeller which are due to the near-field pressures induced by the propeller.

The time-dependent forces and moments generated by a propeller operating in the wake of a ship are due to variations in the propeller inflow velocity field. The velocity variations can be thought of as composed of temporal variations, such as turbulence, and spatial variations of the steady velocity field. This report will be concerned with the time-dependent forces and moments generated by a propeller operating in a spatially varying steady velocity field. A typical spatial distribution of velocity is shown in Figure 1.

Various aspects of this area of propeller time-dependent forces and moments have been investigated. Several analytical methods exist for the prediction of propeller time-dependent forces and moments due to operation in a spatially varying velocity field, References (1), (2), and (3). In addition, the time-dependent forces and moments generated by various propellers, operating over a range of conditions, e.g., advance ratio, due to operating in a variety of spatially varying velocity fields have been measured, References (3), (4), (5), and (6).

PURPOSE OF INVESTIGATION

The purpose of this investigation is twofold: (1) to measure the time-dependent thrust generated by a series of propellers operating in a number of different spatially varying velocity fields over a range of operating conditions, and (2) to correlate some representative measured values with values predicted by two analytical approaches.

Propellers having two, five, and ten blades were tested. Each propeller was operated in the wake shed by a strut, located at a number of distances between the strut and the propeller. For each of the strut positions considered, measurements were made for each propeller operating over a range of advance ratios and free-stream velocities.

Correlations are made between representative measured values and values predicted by two analytical methods. The first analytical method is based on two-dimensional unsteady airfoil theory. The second analytical method is based on unsteady lifting surface theory.

THEORY

Introduction

A number of fundamentally different theories for predicting the time-dependent forces and moments generated by a propeller operating in a spatially varying velocity field exist. These theoretical approaches can be divided into the following categories: (1) quasi-steady using uniform flow tests, (2) quasi-steady using steady-state lifting-line theory, (3) two-dimensional unsteady, (4) combination quasi-steady and two-dimensional unsteady, and (5) three-dimensional, unsteady lifting surface.

Boswell, Reference (6), has measured the time-dependent forces generated by a series of propellers operating in a spatially varying velocity field. Correlations between the measured values and each of the above theories showed that the three-dimensional, unsteady lifting surface theory gave good agreement with the magnitude of the measured values. In addition, the proper trends with variations in propeller advance ratio and expanded area ratio were predicted. The two-dimensional unsteady theory predicted the correct trend for variations in propeller expanded area ratio but the magnitude was too large. The other theories predicted neither the correct magnitude nor trends.

As a consequence of Boswell's results, the two theoretical approaches considered here will be the two-dimensional, unsteady theory and the three-dimensional, unsteady lifting surface theory. Each theory is described briefly.

Two-Dimensional Unsteady Theory

The two-dimensional unsteady theory assumes that the propeller blades are two-dimensional, isolated airfoils with small camber (i.e. lightly loaded). The fluid in which the propeller operates is assumed to be incompressible and inviscid. Sears, Reference 7, has determined the unsteady lift on an airfoil which operates in a free-stream velocity with a superposed sinusoidal velocity which is normal to the airfoil surface, Figure 2. The result is given as

$$L_v = 2\pi\rho_f \, b \, U \, W \; K(k) \, e^{i\omega t} \qquad (1)$$

where

$L_v \equiv$ lift per unit span

$K(k) \equiv$ Sears' function, see Figure 3.

Horlock, Reference 8, has shown that the unsteady lift on an airfoil operating in a uniform velocity field upon which is superposed sinusoidal velocity variations along the airfoil surface is given by

$$L_u = 2\pi\rho_f \; U \; u_o \; b \; \alpha \; T(k) \; e^{i\omega t} \qquad (2)$$

where

$L_u \equiv$ lift per unit span

$T(k) \equiv$ Horlock function, see Figure 4.

A brief description of the application of two-dimensional, unsteady airfoil theory to a propeller operating in a spatially non-uniform inflow is given.

A typical spatial distribution of the propeller inflow velocity for this investigation is shown in Figure 5. At a constant radius, the circumferential velocity distribution can be decomposed into Fourier components, i.e.,

$$U_L/U_\infty \left(\frac{r_j}{R_{tip}} , \theta \right) = U_L/U_\infty(\theta)_j = \sum_{n=-\infty}^{\infty} C_{nj} \; e^{in\theta} \qquad (3)$$

where

$$C_{nj} = \frac{1}{2\pi} \int_o^{2\pi} U_L/U_\infty(\theta)_j \; e^{-in\theta} \; d\theta \; .$$

Consequently, a typical radial element of a propeller blade can be thought of as operating in an infinite number of superposed sinusoidal gust velocities with magnitude C_{nj}. One can therefore apply the results of Sears and Horlock to determine the unsteady lift of a radial element of a propeller blade. The unsteady lift on a typical blade element due to the n^{th} component of the propeller inflow, shown in Figure 6, is

$$\tilde{L}_{nj} = 2\pi\rho_f \; b_j \; U_{Rj} \; U_\infty \Delta r_j \; C_{nj} \; \{K(k_{nj}) \cos \beta_j - \alpha_j \; T(k_{nj}) \sin \beta_j\} e^{in(\Omega t+\phi_j)} \qquad (4)$$

Equation (4) was derived from the equations for unsteady lift on an isolated airfoil operating in sinusoidal velocity disturbances normal to the airfoil's surface and along the airfoil's surface. Equation (4), however, is to be applied to a propeller where, for a large number of blades, the isolated airfoil concept will be invalid. The 2π component of Equation (4) may be thought of as the lift curve slope, $(\partial C_L/\partial\alpha)$ for the two-dimensional isolated airfoil. To include the effects of adjacent blades on unsteady forces and moments, let us substitute the value of $(\partial C_L/\partial\alpha)$ for 2π at each blade segment considered, i.e., replace 2π in Equation (4) by $(\partial C_L/\partial\alpha)_j$, hence,

$$\tilde{L}_{nj} = \left(\frac{\partial C_L}{\partial\alpha}\right)_j \rho_f\, b_j\, U_{Rj}\, U_\infty\, C_{nj}\, e^{in(\Omega t+\phi_j)}\{K(k_{nj})\cos\beta_j - \alpha_j\, T(k_{nj})\sin\beta_j\}\Delta r_j \tag{5}$$

Using similar arguments, the unsteady moment on the j^{th} blade element, about the center of the propeller, due to the n^{th} Fourier component of the propeller inflow is given by

$$\tilde{M}_{nj} = \left(\frac{\partial C_L}{\partial\alpha}\right)_j \rho_f\, b_j\, r_j\, U_{Rj}\, U_\infty\, C_{nj}\, e^{in(\Omega t+\phi_j)}\{K(k_{nj})\cos\beta_j - \alpha_j\, T(k_{nj})\sin\beta_j\}\Delta r_j \tag{6}$$

The $(\partial C_L/\partial\alpha)_j$ term should then be determined from experimental or theoretical data which reflects the cascade effects and airfoil section characteristics at each blade segment in steady flow. In this investigation, the values of $(\partial C_L/\partial\alpha)_j$ were determined from experimental data for airfoil cascades, Reference 9. The radial variations of $\partial C_L/\partial\alpha$ for the two-, five-, and ten-bladed propellers as calculated from the data in Reference 9 are given in Table 1.

Adopting the coordinate system shown in Figure 7, and summing over all Fourier components corresponding to positive propeller rotation and then summing over all blade elements, the following components of unsteady force and moment act on the propeller shaft:

$$\begin{aligned} \tilde{F}_z &= \sum_{j=1}^{p} \sum_{\ell=1}^{B} \sum_{n=1}^{\infty} \tilde{L}_{\ell jn} \cos\beta_j \\ \tilde{F}_x &= \sum_{j=1}^{p} \sum_{\ell=1}^{B} \sum_{n=1}^{\infty} \tilde{L}_{\ell jn} \sin\beta_j \sin(\theta + \phi_{\ell j}) \end{aligned} \tag{7}$$

$$\left.\begin{aligned}
\tilde{F}_y &= \sum_{j=1}^{p} \sum_{\ell=1}^{B} \sum_{n=1}^{\infty} \tilde{L}_{\ell jn} \sin \beta_j \cos (\theta + \phi_{\ell j}) \\
\tilde{T}_z &= \sum_{j=1}^{p} \sum_{\ell=1}^{B} \sum_{n=1}^{\infty} \tilde{M}_{\ell jn} \sin \beta_j \\
\tilde{T}_x &= \sum_{j=1}^{p} \sum_{\ell=1}^{B} \sum_{n=1}^{\infty} -\tilde{M}_{\ell jn} \cos \beta_j \sin (\theta + \phi_{\ell j}) \\
\tilde{T}_y &= \sum_{j=1}^{p} \sum_{\ell=1}^{B} \sum_{n=1}^{\infty} -\tilde{M}_{\ell jn} \sin \beta_j \cos (\theta + \phi_{\ell j})
\end{aligned}\right\} \qquad (7)$$

In Equation (7), the sum over the blade elements has been separated into a sum over p elements per blade and a sum over B blades. The quantity $\phi_{\ell j} = \Psi_j + \eta_\ell$, where Ψ_j is the phase angle due to blade skew and η_ℓ is the phase angle due to blade separation. The quantities $L_{\ell jn}$ and $M_{\ell jn}$ are the same as given in Equations (5) and (6) except that ϕ_j is replaced by $\phi_{\ell j}$.

It is shown in Reference 3 that only certain harmonics of the propeller inflow contribute to the unsteady forces and moments on the propeller. Only those harmonics of the inflow which are integer multiples of the number of propeller blades (mB) contribute to the unsteady thrust F_z and torque $\tilde{T}_z$. Only those harmonics of the inflow which are adjacent to the multiples of the number of propeller blades $(mB \pm \ell)$ contribute to the unsteady side forces, $\tilde{F}_x$ and $\tilde{F}_y$, and bending moments, T_x and T_y. A summary of the sensitivity of various propellers to the harmonic components of the propeller inflow is given in Table 2.

It can be shown that Equations (7) reduce to

$$\begin{aligned}
(\tilde{F}_z)_m &= B \sum_{j=1}^{p} \{ |\tilde{L}_{j(mB)}|_1 \, e^{imB(\Omega t + \Psi_j)} \} \\
(\tilde{F}_x)_m &= \frac{B}{2} \sum_{j=1}^{p} \{ i \, [-|\tilde{L}_{j(mB-1)}|_2 + |\tilde{L}_{j(mB+1)}|_2] \, e^{imB(\Omega t + \Psi_j)} \} \qquad (8) \\
(\tilde{F}_y)_m &= \frac{B}{2} \sum_{j=1}^{p} \{ [|\tilde{L}_{j(mB-1)}|_2 + |\tilde{L}_{j(mB+1)}|_2] \, e^{imB(\Omega t + \Psi_j)} \}
\end{aligned}$$

$$\left.\begin{aligned}
(\tilde{T}_z)_m &= B \sum_{j=1}^{p} \{ \, | \tilde{M}_{j(mB)} |_1 \; e^{imB(\Omega t + \Psi_j)} \} \\
(\tilde{T}_x)_m &= -\frac{B}{2} \sum_{j=1}^{p} \{ i \, [- |\tilde{M}_{j(mB-1)}|_2 + |\tilde{M}_{j(mB+1)}|_2] \; e^{imB(\Omega t + \Psi_j)} \} \\
(\tilde{T}_y)_m &= -\frac{B}{2} \sum_{j=1}^{p} \{ \, [|\tilde{M}_{j(mB-1)}|_2 + |\tilde{M}_{j(mB+1)}|_2] \; e^{imB(\Omega t + \Psi_j)} \}
\end{aligned}\right\} \quad (8)$$

where

$$\left.\begin{aligned}
|\tilde{L}_{jn}|_1 &= \left(\frac{\partial C_L}{\partial \alpha}\right)_j \rho_f \, b_j \, \Delta r_j \, U_{Rj} \, U_\infty \, C_{nj} \, \{K(k_{nj}) \cos \beta_j - \alpha_j \, T(k_{nj}) \sin \beta_j\} \cos \beta_j \\
|\tilde{L}_{jn}|_2 &= \left(\frac{\partial C_L}{\partial \alpha}\right)_j \rho_f \, b_j \, \Delta r_j \, U_{Rj} \, U_\infty \, C_{nj} \, \{K(k_{nj}) \cos \beta_j - \alpha_j \, T(k_{nj}) \sin \beta_j\} \sin \beta_j \\
|\tilde{M}_{jn}|_1 &= \left(\frac{\partial C_L}{\partial \alpha}\right)_j \rho_f \, b_j \, r_j \, \Delta r_j \, U_{Rj} \, U_\infty \, C_{nj} \, \{K(k_{nj}) \cos \beta_j - \alpha_j \, T(k_{nj}) \sin \beta_j\} \sin \beta_j \\
|\tilde{M}_{jn}|_2 &= \left(\frac{\partial C_L}{\partial \alpha}\right)_j \rho_f \, b_j \, r_j \, \Delta r_j \, U_{Rj} \, U_\infty \, C_{nj} \, \{K(k_{nj}) \cos \beta_j - \alpha_j \, T(k_{nj}) \sin \beta_j\} \cos \beta_j
\end{aligned}\right\} (9)$$

The quantity n in Equations (9) takes on the values mB, mB+1, or mB-1 according to their use in Equations (8). Also, since the values of C_{nj} are for positive values of n only, C_{nj} may be written in terms of the real and imaginary components of the complex Fourier coefficient as

$$C_{nj} = \frac{1}{2} \, (A_{nj} - i \, B_{nj})$$

for the purpose of computation.

A computer program has been written which calculates the unsteady forces and moments, generated by a propeller operating in a spatially varying velocity field, as given by Equations (8) and (9).

Unsteady Lifting Surface Theory*

Hanaoka, Reference (10), developed a linearized, unsteady, lifting-surface theory for calculating the unsteady loading developed by a propeller. The

---

*Parts of this section are taken from Reference (1).

propeller is assumed to be operating in an incompressible, potential flow. Both the lifting-surface and trailing vorticity are assumed to lie on a predetermined helicoidal surface of constant pitch and any deviation from this surface by either the flow or the lifting surface is considered as a small perturbation. Under consideration here is the case of a rigid propeller operating at a constant advance velocity and rotational velocity in a spatially varying inflow velocity field. Hanaoka derived the following integral equation which relates the known unsteady downwash distribution on the blades to the unknown unsteady loading distribution:

$$V_N^n(r)\, e^{in(\Omega t - \phi_o)} = \sum_{n=1}^{B} \frac{e^{iq\Omega t}}{4\pi\rho_f V_a} \int\!\!\int_S \Delta p(\xi,\rho,\theta_o) \frac{\partial}{\partial n'} \int_{-\infty}^{x} e^{iq[a(\tau'-x)-\overline{\theta}_n]} \frac{\partial}{\partial n} \left(\frac{1}{R}\right) d\tau'\, dS \tag{10}$$

where

$$R = \{(\tau' - \xi)^2 + r^2 + \rho^2 - 2r\rho \cos [\theta_o - \phi_o + \overline{\theta}_n - a(\tau'-x)]\}^{1/2} \quad .$$

In a series of investigations conducted at Stevens Institute of Technology, References (11), (12), (13), and (1), the unsteady lifting-surface equation has been numerically evaluated under successively less restrictive assumptions regarding the propeller geometry and the chordwise loading distribution. The techniques of evaluation used in the most recent investigation, Reference (1), are reviewed here, since this method has been employed to predict time-dependent propeller thrust in the present investigation.

The directional derivatives normal to the helicoidal surface are given by:

At the control point,

$$\frac{\partial}{\partial n'} = \frac{r}{\sqrt{1 + a^2 r^2}} \left[a \frac{\partial}{\partial x} - \frac{1}{r^2} \frac{\partial}{\partial \phi_o} \right]$$

At the loading point

$$\frac{\partial}{\partial n} = \frac{\rho}{\sqrt{1 + a^2 \rho^2}} \left[a \frac{\partial}{\partial \xi} - \frac{1}{\rho^2} \frac{\partial}{\partial \theta_o} \right] \quad .$$

A high order singularity exists in the kernel of the integral equation. In order to circumvent this problem, the integral is evaluated over the projection of the blade in the propeller plane instead of over the actual blade surface. After the mathematical manipulations have been performed on the slightly shifted surface, the projected surface is brought back into coincidence with the actual surface.

Equation (10) can be written as

$$\frac{V(r)}{U} e^{iq(\Omega t-\phi_o)} = \int_o^{\pi} \int_{\rho} S(\rho,\theta_o)\, K(r,\phi_o;\rho,\theta_o;q) \sin \theta_\alpha\, d\theta_\alpha\, d\rho$$

where

$$S(\rho,\theta_o) = \Delta p(\rho,\theta_o)\, \rho\, \theta_b^{\rho}$$

$$K(r,\phi_o;\rho,\theta_o;q) = -\frac{e^{iq\Omega t}}{4\pi\rho_f U^2} \left[\frac{\sqrt{1+a^2\rho^2}}{a\rho} \right] \lim_{\hat{\delta} \to o} \sum_{n=1}^{N} e^{-iq\bar{\theta}_n} \frac{\partial}{\partial n'} \int_{-\infty}^{x} e^{iqa(\tau'-x)} \frac{\partial}{\partial n} \left(\frac{1}{R}\right) d\tau', \tag{13}$$

and the transformation $\theta_o = \theta_b^{\rho} \cos \theta_\alpha$ has been used.

The unknown loading function $S(\rho,\theta_o)$ is approximated by a Birnbaum series

$$S(\rho,\theta_o) = \frac{1}{\pi} \left\{ L^{(1)}(\rho) \cot \frac{\theta_\alpha}{2} + \sum_{\bar{n}=2}^{\infty} L^{(\bar{n})}(\rho) \frac{\sin (\bar{n}-1)\theta_\alpha}{\bar{n}-1} \right\} \tag{14}$$

where $L^{(\bar{n})}(\rho)$ are the spanwise loading components. This series reproduces the proper leading edge singularity and fulfills the Kutta condition along the trailing edge.

The inverse Descartes distance is expanded in terms of Legendre functions of the second kind

$$\frac{1}{[\chi^2 + r^2 + \rho^2 - 2r\rho \cos \Theta]^{1/2}} = \sum_{m=0}^{\infty} \epsilon_m \cos m\Theta \frac{1}{\pi \sqrt{r\rho}} Q_{m-1/2}\left(\frac{\chi^2 + r^2 + \rho^2}{2r\rho} \right) \tag{15}$$

where

$$\epsilon_m = \begin{cases} 1 \text{ , } m=0 \\ 2 \text{ , } m\neq 0 \end{cases}$$

The kernel is now in separable form, so that the chordwise integration can be performed, whereby, the surface integral equation is reduced to a line integral equation

$$\frac{V(r)}{U} \; e^{iq(\Omega t-\phi_o)} = \int_\rho L^{(1)}(\rho)\, \overline{K}^{(1)}(r,\rho,\phi_o;q)d\rho + \int_\rho \sum_{\overline{n}=2}^{\infty} L^{(\overline{n})}(\rho)\overline{K}^{(\overline{n})}(r,\rho,\phi_o;q)d\rho \; . \tag{16}$$

The new kernels $\overline{K}^{(\overline{n})}$ are the result of the θ_α - integration.

The transformation $\phi_o = -\theta_b^r \cos \phi_\alpha$ is made and the integral equation becomes

$$\frac{V(r)}{U} \; e^{iq\theta_b^r \cos \phi_\alpha} = \int_\rho \sum_{\overline{n}=1}^{\infty} L^{(\overline{n})}(\rho) \sum_{m=-\infty}^{\infty} f_m(q,\phi_\alpha)\; \overline{K}_m^{(\overline{n})}(r,\rho;q)d\rho \; . \tag{17}$$

The chordwise boundary conditions are satisfied for each of the chordwise loading modes by use of the series of "generalized lift operators"

$$\begin{aligned} &m=1, \quad \frac{1}{\pi} \int_o^\pi \{ \quad \} (1 - \cos \phi_\alpha)\, d\phi_\alpha \\ &m=2, \quad \frac{1}{\pi} \int_o^\pi \{ \quad \}(1 + 2 \cos \phi_\alpha)\, d\phi_\alpha \\ &m>2\,, \quad \frac{1}{\pi} \int_o^\pi \{ \quad \} \frac{\cos\,(m-1)\phi_\alpha}{m-1}\, d\phi_\alpha \; . \end{aligned} \tag{18}$$

Application of the lift operators to both sides of equation (17) results in

$$\frac{V(r)}{U}\, I^{(\overline{m})}\, (q\theta_b^r) = \int_\rho L^{(1)}(\rho)\overline{K}^{(\overline{m},1)}(r,\rho,q)\; d\rho + \sum_{\overline{n}=2}^{\infty} \int_\rho L^{(\overline{n})}(\rho)\overline{K}^{(\overline{m},\overline{n})}(r,\rho;q)\; d\rho \tag{19}$$

where $I^{(\overline{m})}(q\theta_b^r)$ is of the form given in Equation (18), and $\overline{K}^{(\overline{m},\overline{n})}$ are the kernels after both the θ_α and ϕ_α integrations.

The number of resulting integral equations is $\overline{m} = \overline{n}$. The solution of these integral equations is obtained by the collacation method. The blade is divided into i-strips, of length 2β along the span, which reduces the $\overline{m}$ integral equations to a set of algebraic equations

$$\frac{V(r_i)}{U}\; I^{(\overline{m})}(q\theta_b^{r_i}) = \sum_{\overline{n}=1}^{\overline{n}_{max}} \sum_{j=1}^{p} L^{(\overline{n})}(\rho_j)K_{ij}^{(\overline{m},\overline{n})}\; (r_i,\rho_i) \; . \tag{20}$$

This set of equations is solved for the spanwise loading components $L^{(\bar{n})}(\rho_j)$ by the use of a digital computer.

The resulting spanwise loading distribution is

$$L(r) = L^{(1)}(\rho_j) + \frac{1}{2} L^{(2)}(\rho_j) \quad . \tag{21}$$

The time-dependent thrust at blade rate frequency is given by

$$T_q = - \text{Re} \left[B \int_{R_{hub}}^{R_{tip}} L(r) \frac{ar}{\sqrt{1 + a^2 r^2}} \, dr \right] e^{iq\Omega t} \quad . \tag{22}$$

A computer program which calculates the time-dependent forces and moments generated by a propeller as predicted by the unsteady lifting surface theory was obtained from the Naval Ship Research and Development Center. This program approximates the directional derivatives normal to the helicoidal surface by directional derivatives in the axial direction, i.e.,

$$\frac{\rho}{\sqrt{1 + a^2 \rho^2}} \left(a \frac{\partial}{\partial \xi} - \frac{1}{\rho^2} \frac{\partial}{\partial \theta_o} \right) \rightarrow \frac{\partial}{\partial \xi}$$

$$\frac{r}{\sqrt{1 + a^2 r^2}} \left(a \frac{\partial}{\partial x} - \frac{1}{r^2} \frac{\partial}{\partial \phi_o} \right) \rightarrow \frac{\partial}{\partial x} \quad .$$

In addition, the helicoidal surface of integration, both on the blades and in the downstream wakes, is approximated in a staircase manner. The calculations made for this investigation used five chordwise modes.

EXPERIMENTAL DETERMINATION OF SPATIAL VELOCITY DISTRIBUTIONS

Introduction

As shown in Equation (9), the theoretical value of the time-dependent thrust generated by a propeller operating in a spatially varying velocity field is proportional to the radial distribution of the harmonic content of the circumferential variation of the axial velocity. These quantities must be determined from experimental velocity distributions. The first part of the experimental program involved measuring the circumferential distribution of axial velocity in the propeller leading edge plane for each of the test conditions at which unsteady propeller thrust was measured.

Test Apparatus

The spatial variations in the propeller inflow were generated by a strut with a symmetrical airfoil cross-section having an eight-inch chord and a one-inch maximum thickness. In order to measure time-dependent propeller thrust in velocity fields having different spatial variations, the strut-to-propeller spacing was adjustable from four inches to thirty-two inches. The strut was placed at zero angle of attack and, therefore, the wake width was proportional to $\chi^{1/2}$ and the maximum velocity deficit was proportional to χ^{-1}, where χ is the distance from the strut trailing edge, Reference (14). A typical velocity distribution behind the strut is shown in Figure 5.

In order to determine the harmonic content of the propeller inflow, the circumferential distributions of axial velocity at a number of radii were measured. A wake rake, i.e., a series of radially distributed pitot total and static tubes, Figure 8, was employed for these measurements. The wake rake is shown schematically in Figure 9.

Data Acquisition and Reduction

The rake was rotated about its center-line through 180° and, since the rake was symmetric about the center-line, a survey over 360° was made. Measurements were made at each of the following angular increments, where zero is perpendicular to the strut:

θ	$\Delta\theta$
0° - 70°	5°
70° - 110°	1°
110° - 180°	5°

A typical velocity distribution as measured with the wake rake is shown in Figure 5.

The data acquisition and reduction system used in measuring the velocity distributions is shown in the block diagram of Figure 10. At each angular position considered, the values of total and static pressures measured by the wake rake pitot tubes were recorded on paper tape. In addition, the free-stream total and static pressures were recorded. Based on these data, the free-stream velocity and the radial distribution of velocity at each angular position considered were calculated. Thereby, the circumferential distribution of axial velocity at various radii were determined.

The velocity distributions were determined for a free-stream velocity of 15, 18, and 21 ft/sec at each of the following distances downstream of the strut trailing edge: 4, 5, 6, 7, 8, 10, 12, 16, 24, and 32 inches.

Data Analysis

For each free-stream velocity and strut position considered, the harmonic content of the circumferential distribution of axial velocity at each radius considered was determined. Standard Fourier analysis techniques were used with numerical integration being performed by the trapezoidal rule. The resulting real and imaginary parts of the Fourier coefficients are listed in Table 3. Since the time-dependent thrust on a 2-, 5-, and 10-bladed propeller were considered, only harmonics of order 0, 2, 5, and 10 are listed in the table.

As previously indicated, the object of positioning the strut at a number of upstream distances was to alter the spatial variation of the inflow at the propeller leading edge. Figures 11, 12 and 13 show the second, fifth and tenth complex Fourier coefficient, non-dimensionalized by the free-stream velocity, versus the radial position, non-dimensionalized by the propeller tip radius, for two values of non-dimensional strut position. It is seen in these figures that the Fourier coefficients do vary with strut position.

Since the harmonic content of the propeller inflow is calculated from experimentally determined velocity distributions, there will be some experimental error involved, Reference (15). In order to determine the repeatability of the Fourier coefficients, a series of eight wake surveys were performed with a free-stream velocity of 15 ft/sec and a non-dimensional distance $\chi/D_p = 0.625$ between the strut trailing edge and the wake rake. The Fourier coefficients were calculated for each of the tests at each radius considered. The mean and standard deviation of each set of Fourier coefficients was calculated. Figures 14 through 20 show the mean and standard deviation of the zeroth, second, fifth, and tenth Fourier coefficient versus the non-dimensional radius.

EXPERIMENTAL DETERMINATION OF TIME-DEPENDENT PROPELLER THRUST

Introduction

The time-dependent thrust generated by three different propellers operating in the wake of a strut was measured. Measurements were made for each propeller operating at various advance ratios, for a range of strut-to-propeller distances and for various free-stream velocities.

Test Apparatus

The propellers used in the test are shown in Figure 21. The same blades were used for each of the propellers, the blade number differences being achieved by using different sized spacers on a common hub. Each blade has a constant chord of one inch, no camber, and a span of three inches with a hub-to-tip ratio of 0.25. The design advance ratio of each propeller is $J_D = 1.17$.

The propellers were driven by a dynamometer located downstream as shown in Figure 22. As seen, the forward part of the dynamometer shell was made as small in diameter as possible in order to minimize its effect on the propeller. By placing the propeller drive mechanism downstream, the presence of a boundary layer inflow, with its radial variation in velocity, was avoided. Thus, the generation of time-dependent propeller thrust due only to operation in the strut wake could be studied.

The time-dependent thrust generated by the propeller was measured with a dynamic thrust balance which utilizes a piezo-electric crystal as a sensing element. The balance is located in the propeller drive shaft and is placed as close to the propeller as possible, Figure 23. The crystal generates an electrical signal due to the deformation caused by the time-dependent propeller forces and moments. The time-dependent forces and moments are transmitted to the crystal by a hemi-spherical ball which is aligned with the drive shaft center-line. The piezoelectric crystal is also aligned with the center-line of the drive shaft, see Figure 24. By positioning the hemi-spherical ball and crystal in this way, the sensitivity of the balance to a bending moment is low when compared to the sensitivity to an axial force.

A mass was placed on the drive shaft between the balance and the drive motor. This mass is large when compared to the combined mass of the propeller and short section of drive shaft forward of the balance. Thus, the system is considered to be a lumped mass-spring system, with the compliance provided by a thin walled section on the shaft, see Figure 24. A trade-off was made in the design of the compliant section since it is desired to have a high natural frequency of the system, i.e., large stiffness, and a high balance sensitivity, i.e., small stiffness.

Data Acquisition and Reduction

A block diagram of the data acquisition and reduction system is shown in Figure 25. An electric signal is generated by the piezoelectric crystal due to the deformation caused by the propeller time-dependent forces and moments. Since the balance rotates along with the shaft, the signal is passed through a set of slip-rings. Since slip-rings are a source of noise, the signal is amplified before passing through the slip-rings in order to have a good signal-to-noise ratio.

The signal from the slip-rings was then passed through a set of variable filters, two high pass and one low pass. The low pass filter was set at 1 kHz for all tests and the cut-off frequency of the two high pass filters was set at 50 percent above the shaft rate frequency for each particular test.

The spectrum of the time-dependent thrust was obtained by passing the filtered signal through a wave analyzer. A typical spectrum is shown in Figure 26. The time-dependent thrust of interest here is that occurring at blade-rate frequency, i.e., number of blades times shaft RPS. To measure this, the center frequency of the wave analyzer was set at the blade-rate frequency of the particular test and the level at this frequency was recorded. A typical level of time-dependent thrust at blade-rate frequency is shown in Figure 26.

To determine the amplitude of the blade-rate frequency time-dependent thrust in pounds, the recorded level was compared to the level of a calibration signal. The calibration signal was sinusoidal with an amplitude corresponding to a given force and a frequency equal to the blade-rate frequency of the test under consideration. This calibration signal was passed through the high and low pass filters and through the wave analyzer and the level recorded. The force amplitude of the blade-rate time-dependent thrust was then determined by comparing its signal level with the calibration signal level. A calibration curve is shown in Figure 27. A typical blade-rate time-dependent thrust signal level and calibration signal level are shown on Figure 26.

Calibration

The time-dependent thrust balance was calibrated by applying a known sinusoidal axial force to the propeller shaft and recording the output of the balance. Figure 28 shows the calibration test set-up. The sinusoidal axial force was applied with a fifty-pound electro-magnetic shaker. The amplitude of the force was measured with a force cube located between the shaker and the propeller drive shaft. The balance output was recorded both on the wave analyzer level recorder and on a voltmeter in terms of peak voltage for various known values of applied axial force. Figure 27 shows applied force versus balance output for a range of applied force. It is seen that the balance output is linear with force.

Since the calibration was performed at a frequency of 150 Hz and the blade-rate frequencies of interest ranged from 35 Hz to 298 Hz, the frequency response of the balance for a constant amplitude applied force was determined. The electromagnetic shaker was driven with a white noise generator and the spectrum of the balance output was obtained with the wave analyzer. The frequency response of the balance is shown in Figure 29. As seen, the response is flat with frequency in the range of interest.

The calibration was performed with no steady axial force applied to the shaft. However, during the measurement of the time-dependent thrust generated by a propeller, a steady axial force is applied to the shaft due to the steady thrust generated by the propeller. Tests were performed where the balance output due to a time-dependent axial force was measured when various levels of steady axial force were applied to the shaft. A sketch of the test set-up is shown in Figure 30. The test results are shown in Table 4. The steady thrusts expected during the measurement of time-dependent thrust are shown in Table 5. It is seen that the steady thrust has only a small effect on the measured values of time-dependent thrust.

Tests Conducted

The time-dependent thrust at blade rate frequency generated by a series of propellers operating in the wake of a strut was measured. For each propeller considered, measurements were made with the strut at the following strut trailing edge-to-propeller spacings: 4, 5, 6, 7, 8, 10, 12, 16, 24 and 32 inches.

For each of the strut positions considered, measurements were made for each propeller operating at its design advance ratio, at design advance ratio plus ten percent, and at design advance ratio minus ten percent. Each of these propeller advance ratio conditions was repeated for free-stream velocities of 15, 18, and 21 ft/sec.

The time-dependent thrust at blade-rate frequency is a multiple of shaft-rate frequency. Due to the presence of rotating parts and their supports, the balance will generate signals at shaft-rate frequency and its multiples. The signal generated by the rotating components of the propeller drive system should be lower than the signal generated due to the time-dependent propeller thrust. To obtain the signal level due to the rotating parts, tests were conducted to measure the spectrum of the signal level due to the propellers operating in a spatially uniform inflow, i.e., with no strut mounted in the test section. Spectrum levels were obtained for the two- and ten-bladed propellers operating at various advance ratios and free-stream velocities, and it was shown that the shaft rate signal levels were at least 10 dB lower than the blade rate signals.

RESULTS AND CONCLUSIONS

The results of the investigation are shown in Figures 31 to 46. Figures 31 to 45 are plots of the time-dependent thrust coefficient versus non-dimensional strut-to-propeller distance. Each of these figures represents the experimental and theoretical results obtained with one of the propellers operating at a given advance ratio for a particular free-stream velocity. Figure 46 is a plot of the time-dependent thrust coefficient versus advance ratio for a given strut position and free-stream velocity. Table 6 shows the various conditions under which experiments and theoretical predictions were made for each propeller considered.

The experimentally obtained data have inherent errors associated with them due to the usual sources of experimental error. The values predicted by the theoretical methods also have errors associated with them, since the theories employ the experimentally determined harmonic content of the propeller inflow velocity field. These errors are evident by the inspection of Figures 31 to 45 which show the scatter of the data.

In order to be able to compare the magnitude and trends of the experimental and theoretical values, a least squares polynomial technique was used to fit curves to the data points. The data points comprising any one of the curves has a given shape due to the trend of the data, but also has scatter about the true trend line. The problem is then to select the "correct" degree of the polynomial to fit the data points such that a "true" representation of the curve is obtained while minimizing the effects of the random scatter of the data points. A method of accomplishing this has been developed by Dylewski (16). The general approach taken is to accept that type of curve for representation of the data for which residual deviations show the lease bias, where bias is defined to be systematic discrepancy between the true and the assumed curve types. This minimum bias criterion has been used to choose the degree of the polynomial curve fits shown in Figures 31 to 45. Those plots with no curves fit to the data had insufficient data points to apply the minimum bias criterion.

Predictions of the time-dependent thrust coefficients, based on the two-dimensional unsteady airfoil theory, have been made for the five-, and ten-bladed propellers operating at each of three advance ratios in a free-stream velocity of 18 ft/sec for all of the strut positions considered. Predictions of the time-dependent thrust coefficients, based on unsteady lifting surface theory, have been made for the same test conditions. Comparisons of the results are shown in Figures 37, 38, 39, 43, 44, and 45. It is seen that there is good agreement between the curve fits to the distributions of time-dependent thrust coefficients predicted by the two analytical methods. The maximum difference between the two theories occurs at $\chi/D_p = 0.5$ in Figure 39 where the method based on two-dimensional, unsteady airfoil theory predicts values approximately 15% lower than the values predicted by the method based on unsteady lifting surface theory.

In order to be able to compare experimental results with those obtained from an analytical method, the time-dependent thrust was predicted by the method based on two-dimensional unsteady airfoil theory for all of the test conditions at which propeller time-dependent thrust was measured. A comparison of the predicted and measured values of the propeller thrust can be seen in Figures 31 to 45.

Figures 31 to 45 show that the trend of the time-dependent thrust coefficient versus non-dimensional strut-to-propeller distance as predicted by the analytical method is essentially the same as that of the measured values for non-dimensional distances greater than 1.50. The trends of the analytical and experimental data diverge for values of non-dimensional distances less than 1.50. This can be ascribed to the effects of potential interaction between the propeller blades and the strut, which are present in the case of the measured values, but whose effects are not included in the development of the analytical method.

Although the trends of the experimental and analytical curves are similar for variations in non-dimensional strut position greater than 1.50, there is some difference in the magnitudes of the curves obtained from the experimental data when compared to the curves obtained from the data based on the analytical methods. This difference can be ascribed to the exclusion of certain physical phenomena from the theoretical treatment of the problem, for instance, the effects of the viscous boundary layer formed on the surface of the blades and the effects of blade thickness is ignored.

Figure 46 shows the variation of time-dependent thrust coefficient with advance ratio for the ten-bladed propeller as predicted by the two-dimensional strip theory and as measured experimentally. It is seen that the trends of the two curves are not the same.

As noted previously, the predicted values of the time-dependent thrust, shown in Figures 31 to 45, do not include the contributions due to velocity variations parallel to the surface of the blades. These contributions are neglected altogether in the lifting surface approach and, therefore, have also been neglected, by setting $\alpha_j = 0$ in Equation (9), in the approach based on two-dimensional, unsteady airfoil theory in order that comparisons between the two approaches might be made.

In order to ascertain the effect of velocity fluctuations parallel to the blades, computations of time-dependent thrust coefficient based on two-dimensional strip theory including the Horlock function were made and compared to experimental values and computations based on two-dimensional strip theory excluding the Horlock function. The comparison was made for the ten-bladed propeller operating at an advance ratio of 1.17 in a free-stream velocity of 18 ft/sec. Figure 47 shows the radial variation of the local angle of attack of the blades for the ten-bladed propeller operating at an advance ratio of 1.17. These values of local angle of attack were used in the computations which include the effects of velocity fluctuations parallel to the blades.

The effect of velocity fluctuations parallel to the blades on the time-dependent thrust coefficient is seen in Figure 48. This figure shows the time-dependent thrust coefficient versus the non-dimensional strut-to-propeller distance as determined by experiments, by the two-dimensional theory excluding the Horlock function and by the two-dimensional theory including the Horlock function. It is seen that the inclusion of the effects due to the velocity fluctuations parallel to the blades yields an improvement in the predicted values when compared to the experimental values.

Figure 49 shows the time-dependent thrust coefficient versus the advance ratio as determined by experiment and by the two-dimensional strip theory excluding the effect of velocity fluctuations parallel to the blades. Including the effect of velocity fluctuations parallel to the blades in the two-dimensional strip theory yields the point shown at an advance ratio of 1.17. Although no computations including the effect of velocity fluctuations parallel to the blades were made for advance ratios higher or lower than 1.17, let us consider what occurs for these advance ratios. The steady thrust is developed due to operating the propeller blades at an angle of attack relative to the resultant velocity at the blade leading edges. The variation of the steady thrust with advance ratio is shown in Figure 50. It is seen from this figure that the relative angle of attack of the blades increases as the advance ratio at which the propeller operates decreases. Therefore, the effect of the velocity fluctuations parallel to the blades will increase as the advance ratio at which the propeller operates decreases. Since the velocity fluctuations parallel to the blades reduce the time-dependent thrust of the propeller, at the particular reduced frequency considered here, then the total time-dependent thrust will decrease as the advance ratio decreases. Applying this reasoning to the theoretical curve of Figure 49, it is seen that the trend of the variation of time-dependent thrust coefficient with advance ratio due to theory and experiment will be about the same if the theory includes the effect of velocity fluctuations parallel to the blades.

The conclusion is that the effect of velocity fluctuations parallel to the propeller blades can become appreciable for blades operating at an angle of attack. Naumann, Reference 17, reached the same conclusion in a theoretical analysis and also showed that velocity fluctuations parallel to blades with camber can have a large effect on the time-dependent forces.

REFERENCES

1. Tsakonas, S., W. R. Jacobs, and P. H. Rank, "Unsteady Propeller Listing Surface Theory with Finite Number of Chordwise Modes," Stevens Institute of Technology, DL Report 1133, December 1966.
2. McCarthy, J. H., "On the Calculation of Thrust and Torque Fluctuations of Propellers in Nonuniform Wake Flow," David Taylor Model Basin, Report No. 1533, October 1961.
3. Wereldsma, R., "Dynamic Behavior of Ship Propellers," Publ. No. 255, The Netherlands Ship Model Basin, Wageningen, The Netherlands.
4. Wereldsma, R., "Further Research on Propeller Vibratory Forces," Report No. 66-172-As, The Netherlands Ship Model Basin, Wageningen, The Netherlands.
5. Wereldsma, R., "Research on Propeller Vibratory Forces, Final Report," The Netherlands Ship Model Basin, Report 193, Wageningen, The Netherlands.
6. Boswell, R. J., "Measurement, Correlation with Theory and Parametric Investigation of Unsteady Propeller Forces and Moments," M.S. Thesis, The Pennsylvania State University, August 1967.
7. Sears, W. R., "Some Aspects of Non-Stationary Airfoil Theory and Its Practical Application," J. Aero. Sci., Vol. 8, No. 3, 1941.
8. Horlock, J. H., "Fluctuating Lift Forces on Aerofoils Moving Through Transverse and Chordwise Gusts," Trans. ASME, J. Basic Engr., 68-FE-28, 1968.
9. Emery, J. C., L. J. Herrig, J. R. Erwin, and A. R. Felix,"Systematic Two-Dimensional Cascade Tests of NACA 65-Series Compressor Blades at Low Speeds," NACA TR-1368.
10. Hanaoka, T., "Hydrodynamics of an Oscillating Screw Propeller," Fourth Symposium on Naval Hydrodynamics, Office of Naval Research, Dept. of Navy, ACR-92, 1962.
11. Shiori, J. and S. Tsakonas, "Three-Dimensional Approach to the Gust Problem for a Screw Propeller," Stevens Institute of Technology, D. L. Report 940, March 1963; J. Ship Research, Vol. 7, No. 4, April 1964.
12. Tsakonas, S. and W. R. Jacobs, "Unsteady Lifting Surface Theory for a Marine Propeller of Low Pitch Angle with Chordwise Loading Distribution," Stevens Institute of Technology, DL Report 994, January 1964; J. Ship Research, Vol. 9, No. 2, September 1965.

REFERENCES (Cont'd)

13. Tsakonas, S., C. Y. Chen, and W. R. Jacobs, "Exact Treatment of the Helicoidal Wake in the Propeller Lifting Surface Theory," Stevens Institute of Technology, D. L. Report 1117, August 1966.

14. Silverstein, A., S. Katzoff, and W. K. Bullivant, "Downwash and Wake Behind Plain and Flapped Airfoils," NACA TR-651, 1939.

15. Tjoenneland, J. P., "An Investigation into the Repeability of Wake Survey Data and the Effect of Small Yaw Angles on the Wake Velocities," MIT, Dept. of Naval Architecture and Marine Engineering, Report No. 67-5, January 1967.

16. Dylewski, T. J., "Criteria for Selecting Curves for Fitting to Data," AIAA Journal, Vol. 8, No. 8, August 1970.

17. Naumann, H., "Unsteady Airfoil Theory Applied to Cambered Blades and to Blade Rows of High Solidity", Ph.D. Thesis, University of Pennsylvania, 1971.

TABLE 1

Radial Variations of $\partial C_L/\partial\alpha$ as Calculated from Experimental Cascade Data

Two-Bladed Propeller		Five-Bladed Propeller		Ten-Bladed Propeller	
r/R_{tip}	$\partial C_L/\partial\alpha$	r/R_{tip}	$\partial C_L/\partial\alpha$	r/R_{tip}	$\partial C_L/\partial\alpha$
0.3	2π	0.3	3.10	0.3	1.69
0.4	2π	0.4	4.20	0.4	2.18
0.5	2π	0.5	5.19	0.5	2.95
0.6	2π	0.6	5.96	0.6	3.71
0.7	2π	0.7	2π	0.7	4.10
0.8	2π	0.8	2π	0.8	4.77
0.9	2π	0.9	2π	0.9	5.76
1.0	2π	1.0	2π	1.0	6.20

TABLE 2

Sensitivity of Propellers with Various Blade Numbers to the Harmonic Components of the Inflow

	B	HARMONIC COMPONENTS																				
T_z F_z	3	X			X			X			X			X			X			X		
	4	X				X				X				X				X				X
	5	X					X					X					X					X
	6	X						X						X						X		

T_x F_x T_y F_y	3		X	X		X	X		X	X		X	X		X	X		X	X		X	X
	4		X		X		X		X		X		X		X		X		X		X	
	5		X			X		X			X		X			X		X			X	
	6		X				X		X				X		X				X		X	
		0	1	2	3	4	5	6	7	8	9	10	11	12	13	14	15	16	17	18	19	20

TABLE 3

Harmonic Content of the Propeller Inflow for Various Values of Free-Stream Velocity and Non-Dimensional Strut-to-Propeller Spacing

$V_\infty = 15$ fps

$X/D_p = 0.5$

R/R_{tip}	A_o	A_2	B_2	A_5	B_5	A_{10}	B_{10}
0.2	0.954	0.0251	-0.0011	0.0117	0.0015	-0.0088	-0.0023
0.3	0.955	0.0276	-0.0035	0.0173	0.0007	-0.0094	-0.0016
0.4	0.962	0.0220	-0.0011	0.0112	-0.0011	-0.0069	0.0002
0.5	0.963	0.0150	0.0010	0.0037	-0.0026	-0.0043	0.0019
0.6	0.963	0.0100	0.0013	0.0012	-0.0019	-0.0029	0.0014
0.7	0.962	0.0074	0.0005	0.0010	0.0004	-0.0025	-0.0007
0.8	0.960	0.0062	0.0010	0.0018	-0.0008	-0.0019	0.0007
0.9	0.959	0.0062	0.0014	0.0032	-0.0027	-0.0006	0.0020
1.0	0.959	0.0054	0.0012	0.0043	-0.0020	-0.0004	0.0017

$V_\infty = 15$ fps

$X/D_p = 0.625$

R/R_{tip}	A_o	A_2	B_2	A_5	B_5	A_{10}	B_{10}
0.2	0.963	0.0326	-0.0007	-0.0051	0.0022	0.0059	-0.0006
0.3	0.968	0.0261	-0.0007	-0.0038	0	0.0089	-0.0010
0.4	0.969	0.0207	0.0010	-0.0028	-0.0019	0.0103	0.0024
0.5	0.970	0.0162	0.0008	-0.0026	-0.0015	0.0105	0.0020
0.6	0.970	0.0123	0.0002	-0.0024	-0.0006	0.0109	0.0004
0.7	0.969	0.0094	-0.0002	-0.0013	-0.0021	0.0112	-0.0008
0.8	0.969	0.0073	0.0003	-0.0003	-0.0019	0.0108	0.0023
0.9	0.969	0.0051	0.0007	-0.0002	-0.0005	0.0104	0.0038
1.0	0.970	0.0035	0.0007	-0.0010	0.0005	0.0101	0.0031

TABLE 3 (Cont'd)

$V_\infty = 15$ fps

$X/D_p = 0.75$

R/R_{tip}	A_o	A_2	B_2	A_5	B_5	A_{10}	B_{10}
0.2	0.966	0.0125	-0.0039	-0.0016	0.0028	0.0046	-0.0013
0.3	0.969	0.0102	0	0.0021	0.0053	0.0056	0.0019
0.4	0.970	0.0077	0.0014	0.0031	0.0027	0.0023	0.0016
0.5	0.971	0.0060	0.0010	0.0021	-0.0010	0.0015	0.0023
0.6	0.972	0.0055	0	0.0006	0.0002	0.0043	0.0021
0.7	0.972	0.0069	-0.0009	-0.0009	0.0023	0.0068	-0.0005
0.8	0.971	0.0062	-0.0012	0.0021	-0.0012	0.0057	-0.0021
0.9	0.970	0.0071	-0.0051	0.0089	-0.0012	0.0030	0
1.0	0.967	0.0113	-0.0095	0.0076	-0.0040	0.0017	0.0023

$V_\infty = 15$ fps

$X/D_p = 1.0$

R/R_{tip}	A_o	A_2	B_2	A_5	B_5	A_{10}	B_{10}
0.2	0.968	0.0143	-0.0140	0.0005	-0.0015	0.0033	0.0003
0.3	0.972	0.0176	-0.0007	-0.0070	-0.0047	0.0021	0
0.4	0.974	0.0156	0.0044	-0.0055	-0.0045	0.0036	0.0014
0.5	0.974	0.0122	0.0031	-0.0044	-0.0023	0.0057	0.0016
0.6	0.975	0.0083	0.0008	-0.0030	-0.0006	0.0066	-0.0012
0.7	0.975	0.0052	0.0001	-0.0003	-0.0026	0.0067	-0.0035
0.8	0.975	0.0053	0.0009	0.0012	-0.0013	0.0077	-0.0007
0.9	0.975	0.0044	0.0016	0.0003	-0.0011	0.0079	0.0019
1.0	0.975	0.0046	0.0021	-0.0015	-0.0017	0.0079	0.0018

$V_\infty = 15$ fps

$X/D_p = 1.25$

R/R_{tip}	A_o	A_2	B_2	A_5	B_5	A_{10}	B_{10}
0.2	0.963	0.0294	-0.0006	0.0130	0.0023	0.0047	-0.0091
0.3	0.973	0.0193	-0.0014	0.0102	0.0051	0.0056	-0.0110
0.4	0.974	0.0141	0.0006	0.0071	0.0057	0.0077	-0.0113
0.5	0.975	0.0119	0.0014	0.0053	0.0033	0.0117	-0.0098
0.6	0.975	0.0131	0.0017	0.0042	0.0007	0.0136	-0.0087
0.7	0.975	0.0101	0.0019	0.0043	0.0017	0.0143	-0.0088
0.8	0.976	0.0077	0.0021	0.0055	0.0048	0.0140	-0.0090
0.9	0.977	0.0054	0.0028	0.0048	0.0048	0.0136	-0.0085
1.0	0.980	0.0032	0.0031	0.0038	0.0025	0.0128	-0.0079

TABLE 3 (Cont'd)

V_∞ = 15 fps

X/D_p = 1.50

R/R_{tip}	A_o	A_2	B_2	A_5	B_5	A_{10}	B_{10}
0.2	0.952	0.0278	0.0004	0.0098	0.0001	0.0015	-0.0015
0.3	0.962	0.0177	0.0002	0.0072	0.0030	0.0022	-0.0030
0.4	0.964	0.0133	0.0009	0.0049	0.0037	0.0045	-0.0033
0.5	0.963	0.0126	0.0013	0.0031	0.0014	0.0073	-0.0016
0.6	0.962	0.0120	0.0012	0.0022	-0.0019	0.0090	-0.0004
0.7	0.963	0.0086	0.0014	0.0016	-0.0011	0.0091	0.0004
0.8	0.964	0.0055	0.0014	0.0022	0.0014	0.0085	0.0010
0.9	0.966	0.0039	0.0013	0.0026	0.0021	0.0082	0.0010
1.0	0.967	0.0033	0.0015	0.0016	0.0011	0.0085	0.0010

V_∞ = 15 fps

X/D_p = 2.0

R/R_{tip}	A_o	A_2	B_2	A_5	B_5	A_{10}	B_{10}
0.2	0.973	0.0049	-0.0122	0.0012	-0.0016	0.0027	0.0003
0.3	0.977	0.0140	-0.0033	0.0039	0.0014	0.0028	-0.0002
0.4	0.979	0.0130	0.0032	0.0020	0.0041	0.0021	0.0002
0.5	0.980	0.0094	0.0036	0.0005	0.0028	0.0029	-0.0002
0.6	0.981	0.0059	0.0010	-0.0005	-0.0001	0.0036	-0.0010
0.7	0.982	0.0040	-0.0002	-0.0020	0.0017	0.0035	-0.0002
0.8	0.982	0.0046	-0.0006	-0.0015	-0.0010	0.0045	0.0012
0.9	0.982	0.0049	0	-0.0006	0.0003	0.0046	0.0034
1.0	0.982	0.0043	0.0001	0.0012	0.0021	0.0046	0.0024

V_∞ = 15 fps

X/D_p = 3.0

R/R_{tip}	A_o	A_2	B_2	A_5	B_5	A_{10}	B_{10}
0.2	0.978	0.0054	-0.0079	0.0004	-0.0010	0.0026	0.0013
0.3	0.980	0.0106	-0.0046	0.0034	0.0021	0.0028	0.0008
0.4	0.983	0.0107	0.0016	0.0036	0.0052	0.0031	0.0007
0.5	0.985	0.0101	0.0015	0.0034	0.0045	0.0030	-0.0003
0.6	0.986	0.0075	-0.0007	0.0022	0.0021	0.0029	-0.0021
0.7	0.987	0.0039	-0.0024	0.0004	0.0033	0.0036	-0.0013
0.8	0.988	0.0056	-0.0015	-0.0010	0.0017	0.0048	0
0.9	0.988	0.0037	-0.0002	-0.0012	0	0.0037	0.0019
1.0	0.988	0.0030	0.0005	0.0010	-0.0006	0.0038	0.0033

TABLE 3 (Cont'd)

V_∞ = 15 fps

X/D_p = 4.0

R/R_{tip}	A_o	A_2	B_2	A_5	B_5	A_{10}	B_{10}
0.2	0.971	0.0067	-0.0033	-0.0018	-0.0025	0.0025	-0.0002
0.3	0.981	0.0087	-0.0015	-0.0018	-0.0029	0.0023	0.0001
0.4	0.985	0.0096	0.0016	-0.0010	-0.0017	0.0023	0
0.5	0.987	0.0082	0.0014	-0.0012	0.0008	0.0028	-0.0004
0.6	0.987	0.0065	-0.0001	-0.0017	0.0031	0.0038	-0.0007
0.7	0.987	0.0058	-0.0007	-0.0015	0.0026	0.0045	-0.0008
0.8	0.987	0.0048	0.0001	-0.0017	0.0007	0.0044	0.0003
0.9	0.987	0.0040	0.0009	-0.0012	-0.0010	0.0043	0.0014
1.0	0.987	0.0033	0.0013	-0.0003	-0.0024	0.0042	0.0015

V_∞ = 18 fps

X/D_p = 0.5

R/R_{tip}	A_o	A_2	B_2	A_5	B_5	A_{10}	B_{10}
0.2	0.962	0.0246	-0.0129	0.0029	-0.0088	0.0020	-0.0020
0.3	0.961	0.0283	-0.0028	0.0151	0.0030	-0.0004	-0.0012
0.4	0.960	0.0285	0.0017	0.0135	0.0012	0.0046	0.0010
0.5	0.963	0.0201	0.0020	0.0073	-0.0002	0.0076	0.0024
0.6	0.965	0.0122	0.0007	0.0028	-0.0004	0.0069	0.0001
0.7	0.964	0.0088	-0.0006	-0.0002	0.0002	0.0079	-0.0025
0.8	0.961	0.0094	0.0002	0.0002	-0.0007	0.0107	-0.0003
0.9	0.960	0.0088	0.0007	0.0024	0.0013	0.0116	0.0007
1.0	0.960	0.0069	0.0013	0.0031	0.0030	0.0092	0.0012

V_∞ = 18 fps

X/D_p = 0.625

R/R_{tip}	A_o	A_2	B_2	A_5	B_5	A_{10}	B_{10}
0.2	0.960	0.0325	-0.0019	0.0080	-0.0001	0.0027	-0.0001
0.3	0.965	0.0271	-0.0015	0.0043	0.0043	0.0065	0.0009
0.4	0.967	0.0226	0.0002	0.0034	0.0047	0.0085	0.0026
0.5	0.967	0.0173	0.0003	0.0029	0.0020	0.0093	0.0017
0.6	0.967	0.0130	-0.0007	0.0024	0.0002	0.0089	-0.0007
0.7	0.967	0.0107	-0.0008	0.0017	0.0015	0.0088	-0.0014
0.8	0.966	0.0095	-0.0005	0.0006	0.0023	0.0095	0.0007
0.9	0.966	0.0073	-0.0003	0.0005	0.0027	0.0092	0.0011
1.0	0.966	0.0060	-0.0003	0.0009	0.0020	0.0084	0.0010

TABLE 3 (Cont'd)

V_∞ = 18 fps

X/D_p = 0.75

R/R_{tip}	A_o	A_2	B_2	A_5	B_5	A_{10}	B_{10}
0.2	0.964	0.0168	-0.0137	0.0004	-0.0038	0.0016	-0.0017
0.3	0.967	0.0210	-0.0041	0.0128	0.0027	0.0008	-0.0013
0.4	0.970	0.0171	0.0008	0.0102	0.0048	0.0022	-0.0015
0.5	0.971	0.0128	0.0022	0.0078	0.0025	0.0036	-0.0004
0.6	0.972	0.0095	0.0007	0.0053	0	0.0050	-0.0006
0.7	0.972	0.0077	-0.0009	0.0022	0.0005	0.0076	-0.0030
0.8	0.972	0.0060	-0.0008	0.0010	0.0018	0.0084	-0.0021
0.9	0.972	0.0045	0	0.0009	0.0023	0.0082	-0.0016
1.0	0.972	0.0037	0.0007	0.0022	0.0013	0.0076	-0.0003

V_∞ = 18 fps

X/D_p = 0.875

R/R_{tip}	A_o	A_2	B_2	A_5	B_5	A_{10}	B_{10}
0.2	0.974	0.0121	0.0002	-0.0009	0.0014	0.0007	-0.0009
0.3	0.976	0.0148	0.0006	-0.0099	-0.0044	0.0012	-0.0020
0.4	0.976	0.0145	0.0020	-0.0117	-0.0072	0.0005	-0.0036
0.5	0.977	0.0148	0.0015	-0.0063	-0.0032	0.0024	-0.0048
0.6	0.978	0.0110	-0.0009	-0.0021	0.0025	0.0062	-0.0040
0.7	0.978	0.0053	-0.0003	-0.0005	-0.0032	0.0051	-0.0024
0.8	0.979	0.0058	0.0006	-0.0004	0.0016	0.0077	0.0005
0.9	0.979	0.0059	0.0014	-0.0015	0.0008	0.0083	0.0035
1.0	0.980	0.0046	0.0014	-0.0024	-0.0008	0.0075	0.0029

V_∞ = 18 fps

X/D_p = 1.0

R/R_{tip}	A_o	A_2	B_2	A_5	B_5	A_{10}	B_{10}
0.2	0.972	0.0126	-0.0138	-0.0005	0.0020	0.0010	0.0026
0.3	0.973	0.0184	-0.0020	-0.0079	-0.0035	0.0008	0.0027
0.4	0.974	0.0154	0.0028	0.0063	-0.0059	0.0027	0.0035
0.5	0.975	0.0117	0.0026	-0.00[illegible]4	-0.0022	0.0047	0.0033
0.6	0.975	0.0105	0.0010	-0.0025	-0.0001	0.0058	0.0015
0.7	0.976	0.0058	-0.0004	-0.0003	-0.0026	0.0060	-0.0012
0.8	0.976	0.0064	0.0002	0.0017	-0.0015	0.0081	-0.0005
0.9	0.976	0.0049	0.0015	0.0007	-0.0005	0.0080	0.0038
1.0	0.976	0.0030	0.0021	-0.0012	-0.0007	0.0074	0.0048

TABLE 3 (Cont'd)

V_∞ = 18 fps

X/D_p = 1.25

R/R_{tip}	A_o	A_2	B_2	A_5	B_5	A_{10}	B_{10}
0.2	0.967	0.0246	-0.0015	-0.0006	0.0018	0.0024	0.0001
0.3	0.974	0.0204	0.0017	0.0013	0.0007	0.0036	-0.0001
0.4	0.975	0.0165	0.0026	0.0018	-0.0008	0.0050	0.0021
0.5	0.975	0.0128	0.0018	0.0003	-0.0005	0.0066	0.0018
0.6	0.976	0.0098	0.0012	-0.0008	0.0002	0.0079	0.0012
0.7	0.976	0.0086	0.0012	0	-0.0002	0.0090	0.0013
0.8	0.976	0.0075	0.0013	0.0013	-0.0015	0.0091	0.0022
0.9	0.976	0.0064	0.0012	0.0017	-0.0023	0.0092	0.0017
1.0	0.976	0.0064	0.0011	0.0017	-0.0014	0.0094	0.0009

V_∞ = 18 fps

X/D_p = 1.50

R/R_{tip}	A_o	A_2	B_2	A_5	B_5	A_{10}	B_{10}
0.2	0.954	0.0214	-0.0007	-0.0041	-0.0009	0.0034	-0.0021
0.3	0.960	0.0189	0.0003	0.0001	-0.0003	0.0038	-0.0020
0.4	0.961	0.0150	0.0001	0.0017	-0.0010	0.0045	-0.0003
0.5	0.961	0.0111	0.0010	0.0002	-0.0013	0.0057	-0.0006
0.6	0.962	0.0083	-0.0022	-0.0013	-0.0008	0.0075	-0.0012
0.7	0.963	0.0070	-0.0026	-0.0005	-0.0007	0.0083	-0.0012
0.8	0.963	0.0074	-0.0022	0.0004	-0.0012	0.0083	0.0008
0.9	0.964	0.0072	-0.0023	0.0007	-0.0017	0.0086	0.0011
1.0	0.964	0.0067	-0.0025	0.0002	-0.0010	0.0085	-0.0003

V_∞ = 18 fps

X/D_p = 2.00

R/R_{tip}	A_o	A_2	B_2	A_5	B_5	A_{10}	B_{10}
0.2	0.972	0.0033	-0.0006	-0.0022	0.0007	0.0036	-0.0006
0.3	0.977	0.0145	-0.0006	0.0020	0.0036	0.0032	-0.0003
0.4	0.980	0.0135	0.0025	0.0048	0.0065	0.0033	-0.0005
0.5	0.982	0.0117	0.0006	0.0037	0.0035	0.0031	-0.0016
0.6	0.983	0.0091	-0.0012	0.0018	0.0013	0.0029	-0.0024
0.7	0.984	0.0055	-0.0017	0.0002	0.0032	0.0034	-0.0017
0.8	0.985	0.0071	-0.0012	-0.0017	0.0003	0.0055	-0.0007
0.9	0.985	0.0056	0.0003	-0.0008	-0.0006	0.0052	0.0022
1.0	0.985	0.0044	0.0012	0.0014	0.0008	0.0045	0.0028

TABLE 3 (Cont'd)

V_∞ = 18 fps

X/D_p = 3.00

R/R_{tip}	A_o	A_2	B_2	A_5	B_5	A_{10}	B_{10}
0.2	0.979	0.0060	-0.0042	0.0013	-0.0026	0.0036	0.0006
0.3	0.983	0.0106	-0.0011	0.0022	0.0002	0.0030	0.0003
0.4	0.985	0.0109	0.0017	0.0031	0.0041	0.0026	0
0.5	0.986	0.0118	0.0007	0.0027	0.0035	0.0020	-0.0013
0.6	0.987	0.0101	-0.0012	0.0013	0.0016	0.0023	-0.0019
0.7	0.987	0.0056	-0.0018	-0.0002	0.0031	0.0038	-0.0017
0.8	0.988	0.0080	-0.0013	-0.0019	0.0023	0.0051	-0.0014
0.9	0.988	0.0061	0.0005	-0.0011	0.0004	0.0047	0.0010
1.0	0.988	0.0041	0.0015	0.0009	0.0002	0.0041	0.0023

V_∞ = 18 fps

X/D_p = 4.00

R/R_{tip}	A_o	A_2	B_2	A_5	B_5	A_{10}	B_{10}
0.2	0.978	0.0098	-0.0032	-0.0005	-0.0010	0.0033	0.0001
0.3	0.982	0.0124	-0.0012	-0.0014	-0.0015	0.0035	0.0003
0.4	0.985	0.0131	0.0028	-0.0015	-0.0013	0.0027	0.0005
0.5	0.987	0.0121	0.0015	-0.0016	-0.0002	0.0032	0.0003
0.6	0.989	0.0091	-0.0008	-0.0016	0.0013	0.0041	0.0002
0.7	0.990	0.0077	-0.0021	-0.0015	0.0021	0.0045	0.0003
0.8	0.990	0.0075	-0.0015	-0.0021	0.0014	0.0044	0.0011
0.9	0.990	0.0063	-0.0009	-0.0014	0.0005	0.0044	0.0025
1.0	0.990	0.0057	-0.0004	-0.0013	0.0006	0.0043	0.0026

V_∞ = 21 fps

X/D_p = 0.625

R/R_{tip}	A_o	A_2	B_2	A_5	B_5	A_{10}	B_{10}
0.2	0.962	0.0178	0.0014	0.0049	0.0011	0.0059	-0.0004
0.3	0.965	0.0145	-0.0007	0.0032	0.0007	0.0079	0.0018
0.4	0.966	0.0139	0.0002	0.0031	0.0010	0.0082	0.0034
0.5	0.967	0.0136	0	0.0032	0.0009	0.0088	0.0018
0.6	0.967	0.0126	-0.0006	0.0024	0.0002	0.0088	-0.0010
0.7	0.967	0.0120	-0.0007	0.0015	0.0018	0.0090	-0.0012
0.8	0.967	0.0157	-0.0002	0.0006	0.0048	0.0101	0.0003
0.9	0.967	0.0185	0.0002	0.0010	0.0066	0.0085	0.0003
1.0	0.967	0.0198	-0.0014	0.0031	0.0039	0.0062	0.0002

TABLE 3 (Cont'd)

V_∞ = 21 fps

X/D_p = 0.75

R/R_{tip}	A_o	A_2	B_2	A_5	B_5	A_{10}	B_{10}
0.2	0.970	0.0299	-0.0004	-0.0080	-0.0010	0.0030	-0.0008
0.3	0.977	0.0238	-0.0017	-0.0115	-0.0034	0.0017	0.0005
0.4	0.978	0.0179	0.0003	-0.0100	-0.0044	0.0026	-0.0007
0.5	0.979	0.0126	0.0017	-0.0079	-0.0020	0.0037	-0.0004
0.6	0.979	0.0091	0.0006	-0.0054	0.0003	0.0053	-0.0021
0.7	0.979	0.0086	-0.0010	-0.0021	0	0.0072	-0.0058
0.8	0.979	0.0064	-0.0004	-0.0008	-0.0013	0.0085	-0.0049
0.9	0.979	0.0041	0.0005	-0.0017	-0.0014	0.0089	-0.0010
1.0	0.979	0.0039	0.0010	-0.0023	-0.0011	0.0087	0.0001

V_∞ = 21 fps

X/D_p = 0.875

R/R_{tip}	A_o	A_2	B_2	A_5	B_5	A_{10}	B_{10}
0.2	0.977	0.0194	-0.0015	-0.0086	-0.0012	0.0008	0.0002
0.3	0.979	0.0165	0.0006	-0.0114	-0.0063	0.0003	-0.0016
0.4	0.980	0.0158	0.0010	-0.0135	-0.0075	0	-0.0028
0.5	0.980	0.0155	-0.0006	-0.0068	-0.0008	0.0041	-0.0038
0.6	0.980	0.0126	-0.0019	-0.0032	0.0021	0.0063	-0.0043
0.7	0.980	0.0054	-0.0017	-0.0025	-0.0021	0.0029	-0.0038
0.8	0.980	0.0082	-0.0008	-0.0034	-0.0009	0.0081	-0.0017
0.9	0.980	0.0063	0.0002	-0.0034	0.0001	0.0080	0.0015
1.0	0.980	0.0045	0.0006	-0.0025	-0.0006	0.0072	0.0025

V_∞ = 21 fps

X/D_p = 1.00

R/R_{tip}	A_o	A_2	B_2	A_5	B_5	A_{10}	B_{10}
0.2	0.970	0.0269	0.0001	-0.0025	-0.0004	0.0025	0
0.3	0.975	0.0232	-0.0024	-0.0041	-0.0017	0.0038	0.0001
0.4	0.977	0.0174	-0.0001	-0.0058	-0.0035	0.0043	0.0006
0.5	0.978	0.0148	0.0017	-0.0071	-0.0010	0.0049	0.0007
0.6	0.978	0.0124	0.0009	-0.0060	0.0014	0.0058	-0.0010
0.7	0.978	0.0082	-0.0003	-0.0031	-0.0001	0.0062	-0.0036
0.8	0.978	0.0072	0.0001	-0.0012	-0.0015	0.0082	-0.0029
0.9	0.978	0.0063	0.0010	-0.0008	-0.0012	0.0091	0
1.0	0.978	0.0058	0.0013	-0.0021	-0.0002	0.0080	0.0011

TABLE 3 (Cont'd)

V_∞ = 21 fps

X/D_p = 1.25

R/R_{tip}	A_o	A_2	B_2	A_5	B_5	A_{10}	B_{10}
0.2	0.970	0.0230	0.0037	-0.0034	-0.0008	0.0029	0.0005
0.3	0.976	0.0208	0.0037	-0.0029	-0.0007	0.0035	0.0014
0.4	0.979	0.0163	0.0026	-0.0018	-0.0012	0.0050	0.0022
0.5	0.980	0.0120	0.0013	-0.0014	-0.0007	0.0066	0.0015
0.6	0.980	0.0090	0.0001	-0.0027	0.0001	0.0077	-0.0003
0.7	0.980	0.0074	0.0001	-0.0018	-0.0002	0.0083	0.0001
0.8	0.980	0.0067	0.0004	-0.0004	-0.0009	0.0092	0.0007
0.9	0.980	0.0054	0.0004	-0.0003	-0.0011	0.0093	0.0005
1.0	0.980	0.0046	0.0002	0.0002	-0.0008	0.0091	-0.0007

V_∞ = 21 fps

X/D_p = 1.50

R/R_{tip}	A_o	A_2	B_2	A_5	B_5	A_{10}	B_{10}
0.2	0.976	0.0161	-0.0014	0.0006	0.0035	0.0045	0
0.3	0.981	0.0144	-0.0005	-0.0002	0.0015	0.0048	0.0008
0.4	0.983	0.0120	0.0014	0.0015	0.0009	0.0052	0.0018
0.5	0.984	0.0105	0.0018	0.0032	0.0001	0.0058	0.0015
0.6	0.985	0.0096	0.0013	0.0032	-0.0002	0.0064	0.0008
0.7	0.985	0.0104	0.0013	0.0017	0.0007	0.0064	0.0014
0.8	0.985	0.0122	0.0015	0.0003	0.0016	0.0055	0.0020
0.9	0.983	0.0138	0.0013	0.0004	0.0019	0.0047	0.0019
1.0	0.980	0.0143	-0.0013	0.0016	-0.0001	0.0042	0.0013

V_∞ = 21 fps

X/D_p = 2.00

R/R_{tip}	A_o	A_2	B_2	A_5	B_5	A_{10}	B_{10}
0.2	0.974	0.0075	-0.0055	0.0028	0.0017	0.0166	0.0106
0.3	0.979	0.0115	-0.0018	0.0058	0.0058	0.0164	0.0109
0.4	0.981	0.0110	0.0009	0.0069	0.0091	0.0170	0.0102
0.5	0.983	0.0113	0.0017	0.0065	0.0059	0.0172	0.0085
0.6	0.984	0.0094	0.0001	0.0047	0.0035	0.0169	0.0074
0.7	0.985	0.0046	-0.0031	0.0026	0.0052	0.0177	0.0081
0.8	0.985	0.0065	-0.0028	0.0008	0.0034	0.0197	0.0076
0.9	0.985	0.0051	-0.0010	0.0015	0.0021	0.0210	0.0109
1.0	0.985	0.0037	0.0001	0.0034	0.0023	0.0201	0.0133

TABLE 3 (Cont'd)

V_∞ = 21 fps

X/D_p = 3.0

R/R_{tip}	A_o	A_2	B_2	A_5	B_5	A_{10}	B_{10}
0.2	0.976	0.0028	0.0016	0.0005	0.0017	0.0019	-0.0005
0.3	0.982	0.0081	0.0026	0.0020	0.0038	0.0020	-0.0004
0.4	0.987	0.0110	0.0026	0.0039	0.0039	0.0023	0.0001
0.5	0.989	0.0107	0.0016	0.0050	0.0028	0.0026	0
0.6	0.990	0.0087	0	0.0040	0.0022	0.0033	-0.0008
0.7	0.991	0.0063	-0.0012	0.0016	0.0017	0.0045	-0.0017
0.8	0.991	0.0059	-0.0009	0.0010	0.0009	0.0056	-0.0011
0.9	0.992	0.0055	-0.0003	0.0012	0.0003	0.0060	0.0005
1.0	0.992	0.0049	0.0001	0.0021	0.0002	0.0048	0.0014

TABLE 4

Results of Calibration with Steady Axial Force Applied to the Shaft

Steady Load (lb)	Dynamic Load (peak lb)	Balance Output (peak volt)
0	10	1.00
33	10	0.920
65	10	0.930
104	10	0.885
126	10	0.865

TABLE 5

Steady Thrust of Free-Stream Propellers

2 Blades

J	C_T	Thrust (lb)
1.05	0.19	20.8
1.17	0.105	11.5
1.29	0.03	3.28

5 Blades

J	C_T	Thrust (lb)
1.05	0.36	39.4
1.17	0.185	20.2
1.29	0.055	6.01

10 Blades

J	C_T	Thrust (lb)
1.05	0.48	52.5
1.17	0.22	24.1
1.29	0.04	4.38

July 10, 1972
DET:mac

	TWO-BLADED PROPELLER			FIVE-BLADED PROPELLER				TEN-BLADED PROPELLER			
Free Stream Velocity	Advance Ratio	Experi-ment	Two-Dim. Theory	Advance Ratio	Experi-ment	Two-Dim. Theory	Lifting Surface Theory	Advance Ratio	Experi-ment	Two-Dim. Theory	Liftin Surfac Theor
				1.29	X	X					
15 fps				1.17	X	X					
				1.05	X	X					
	1.29	X	X	1.29	X	X	X	1.29	X	X	X
18 fps	1.17	X	X	1.17	X	X	X	1.17	X	X	X
	1.05	X	X	1.05	X	X	X	1.05	X	X	X
				1.29	X	X					
21 fps				1.17	X	X					
				1.05	X	X					

TABLE 6

Conditions for Which Experiments and Theoretical Predictions Were Made

July 10, 1972
DET:mac

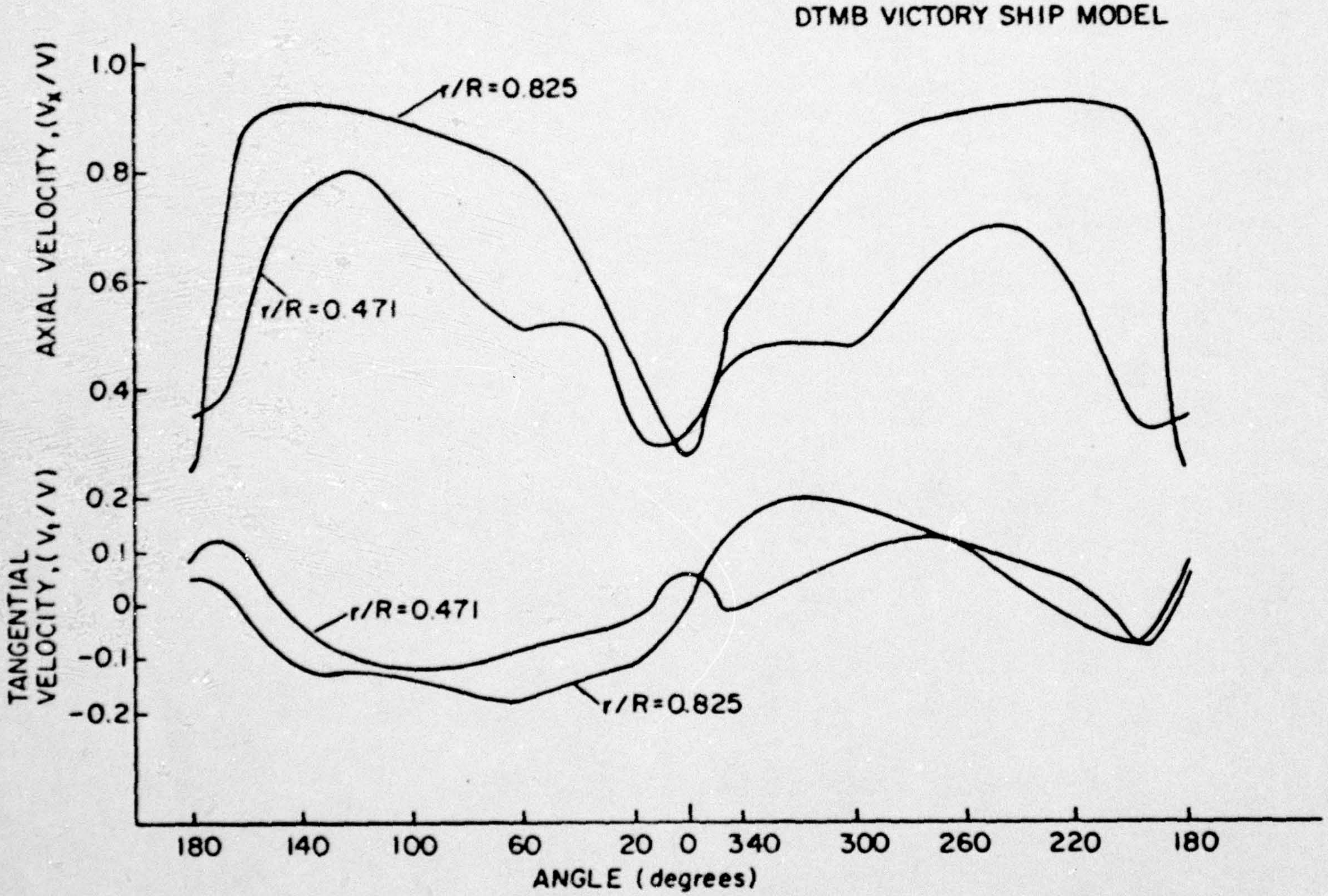

Figure 1 - Distribution of Axial and Tangential Velocity Components in the Propeller Plane of a Single Screw Ship

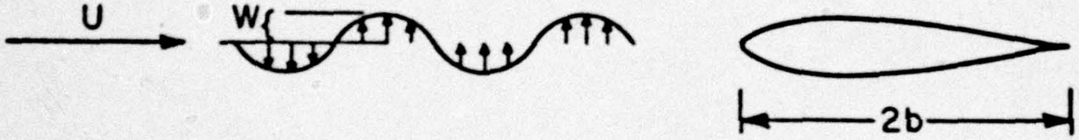

Figure 2 - Airfoil Operating in the Freestream with a Sinusoidal Gust Velocity Normal to the Airfoil's Surface

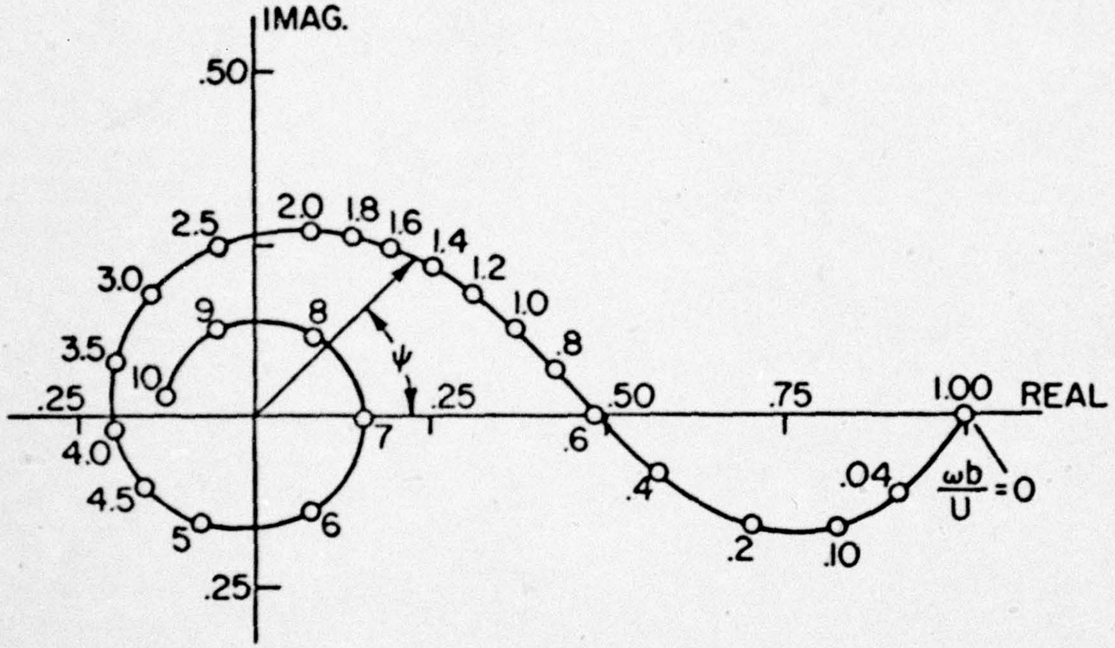

Figure 3 - Non-dimensional Lift, as Calculated by Sears, Represented in the Complex Plane

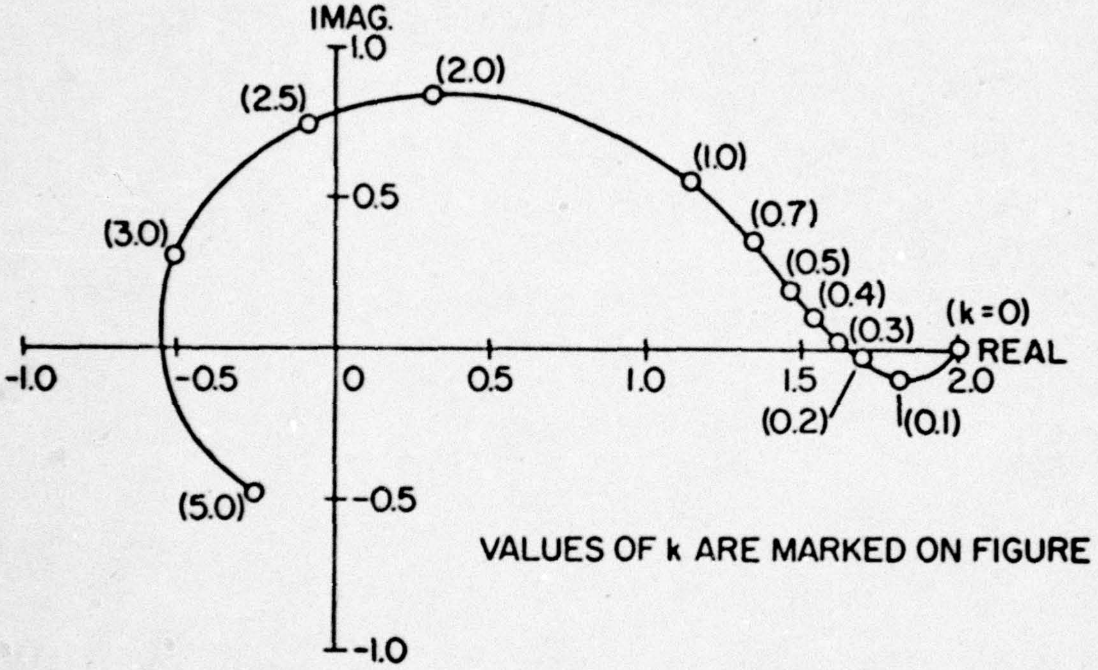

VALUES OF k ARE MARKED ON FIGURE

Figure 4 - Non-dimensional Lift, as Calculated by Horlock, Represented in the Complex Plane

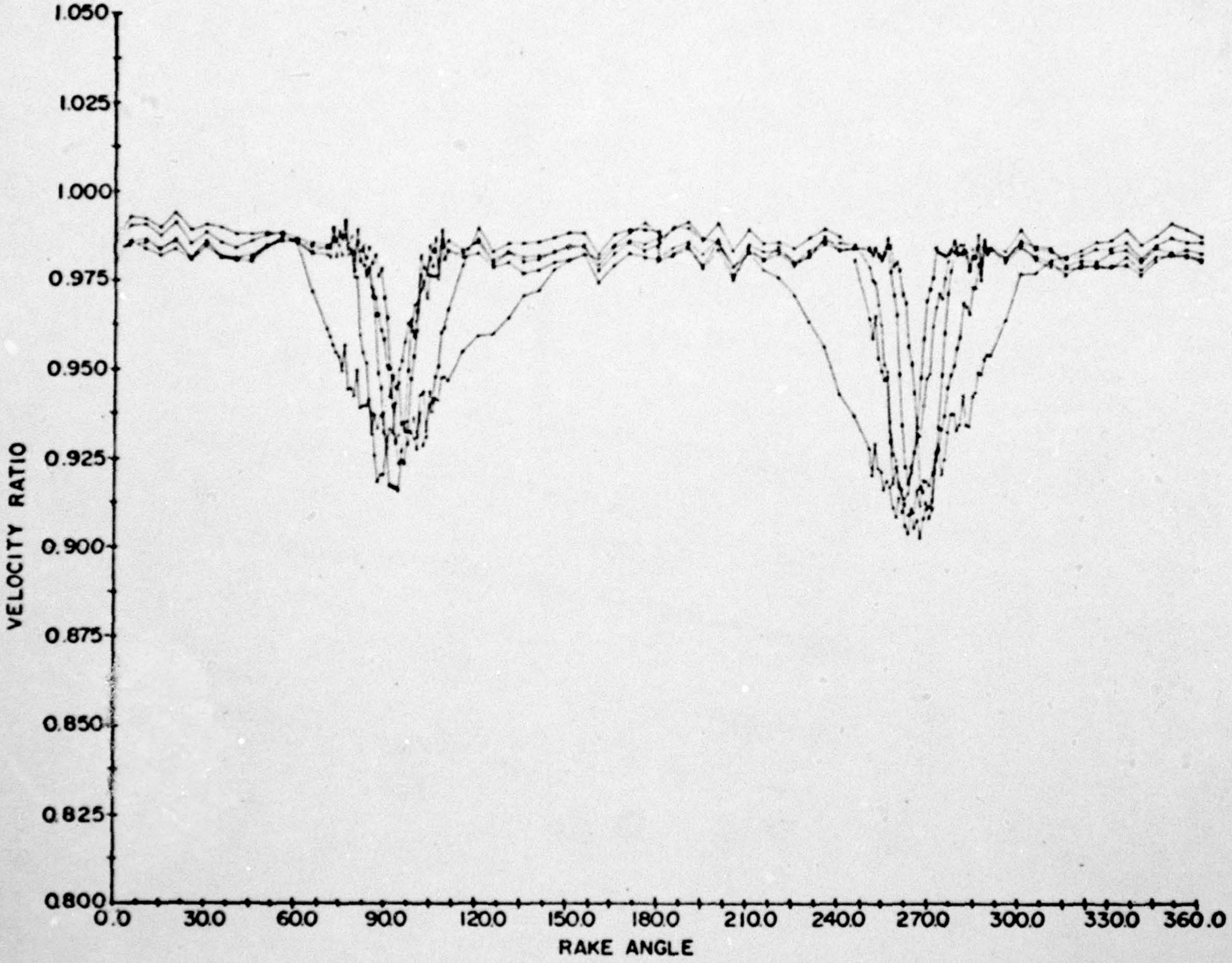

Figure 5 - Typical Circumferential Distribution of Axial Velocity Behind a Strut

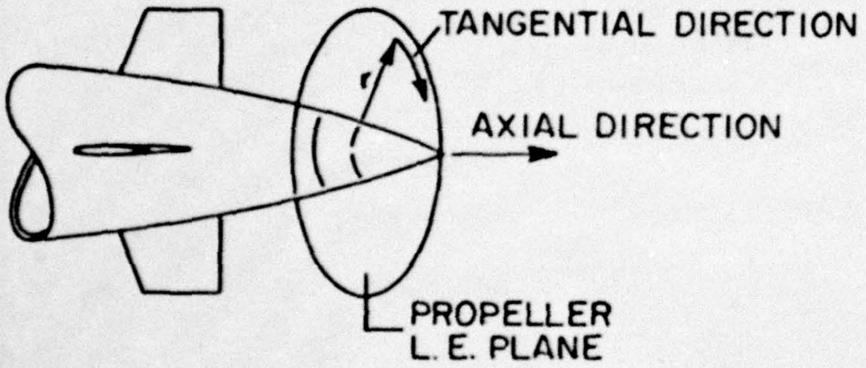

6a. COORDINATE SYSTEM

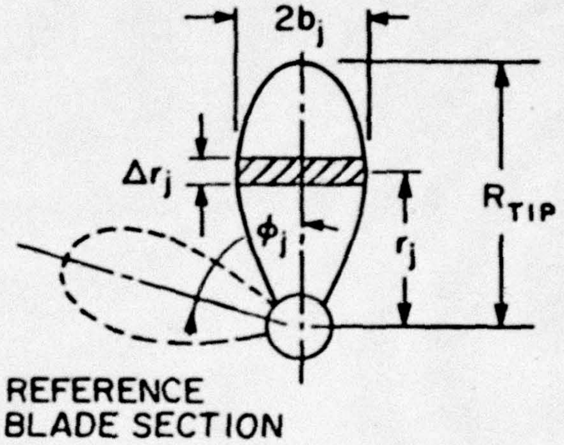

6 b. TYPICAL PROPELLER BLADE

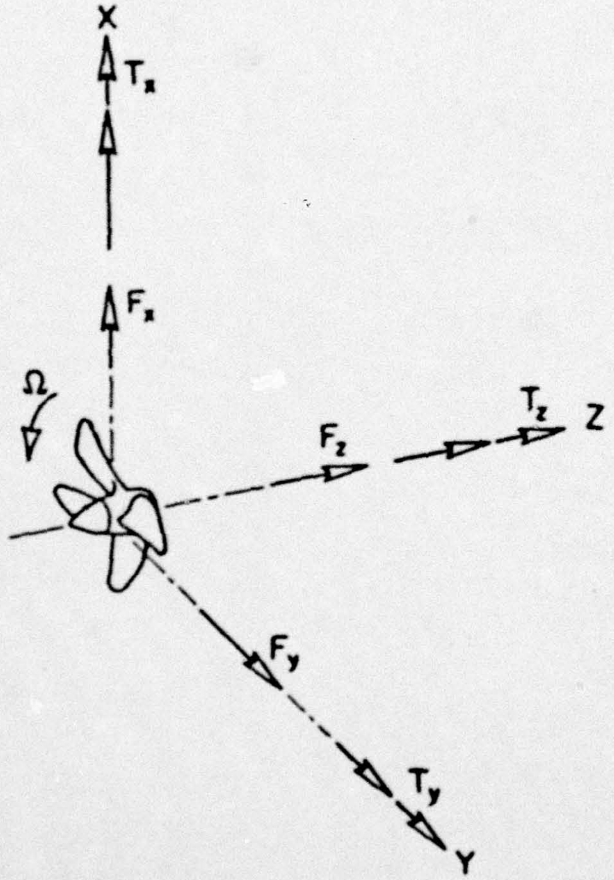

Figure 7 - Coordinate System Assumed for Calculation of Unsteady Forces and Moments

July 10. 1972
DET:mac

Figure 6 - Wake Rake Mounted Behind Strut

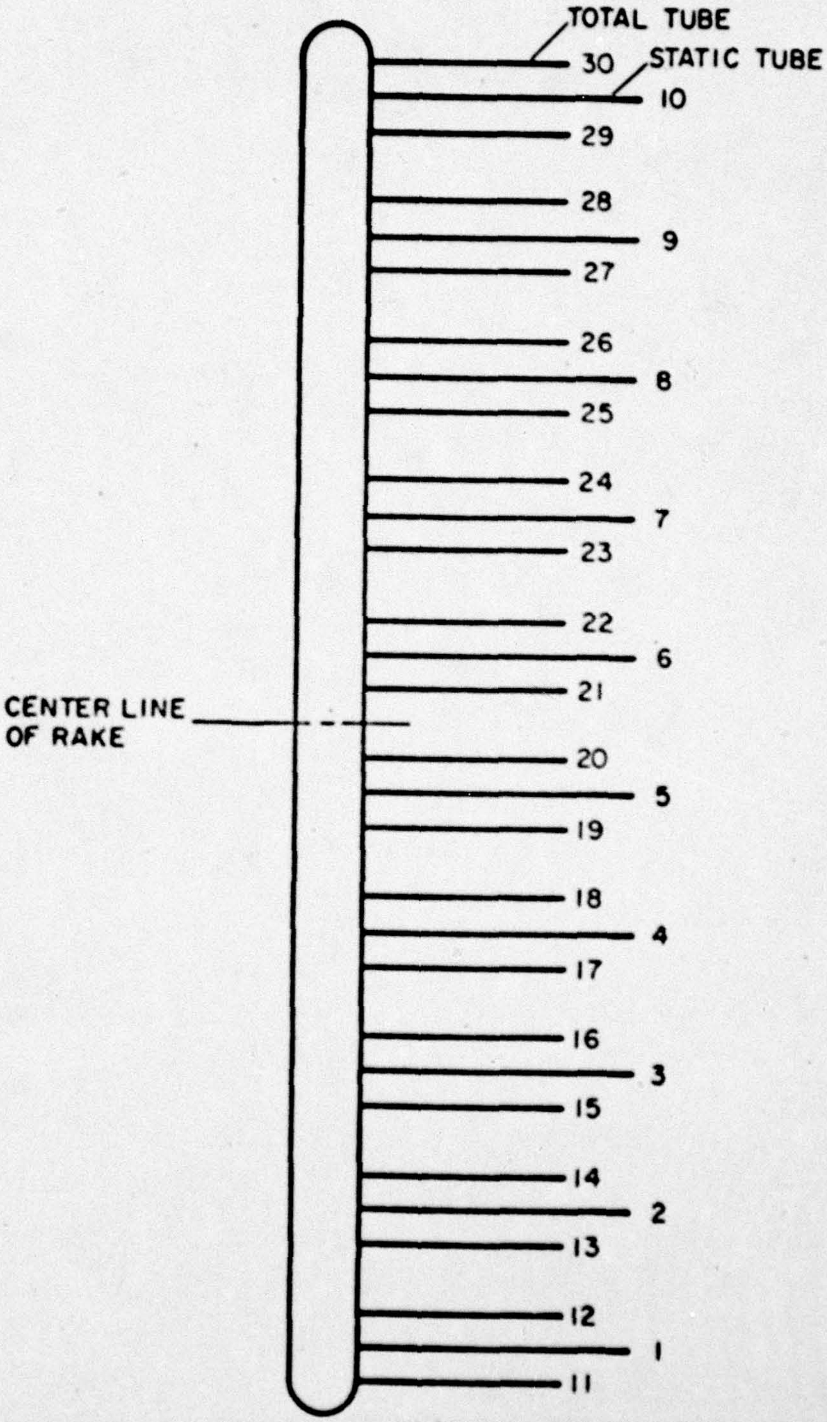

Figure 9 - Schematic of Wake Rake

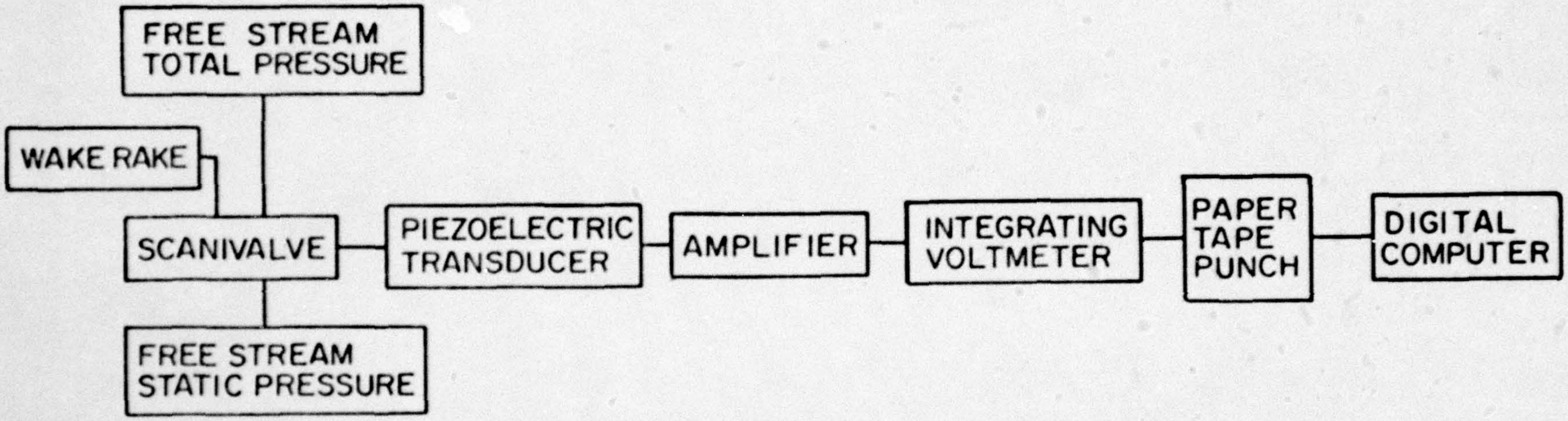

Figure 10 - Data Acquisition and Reduction System for Wake Surveys

July 10, 1972
DET:mac

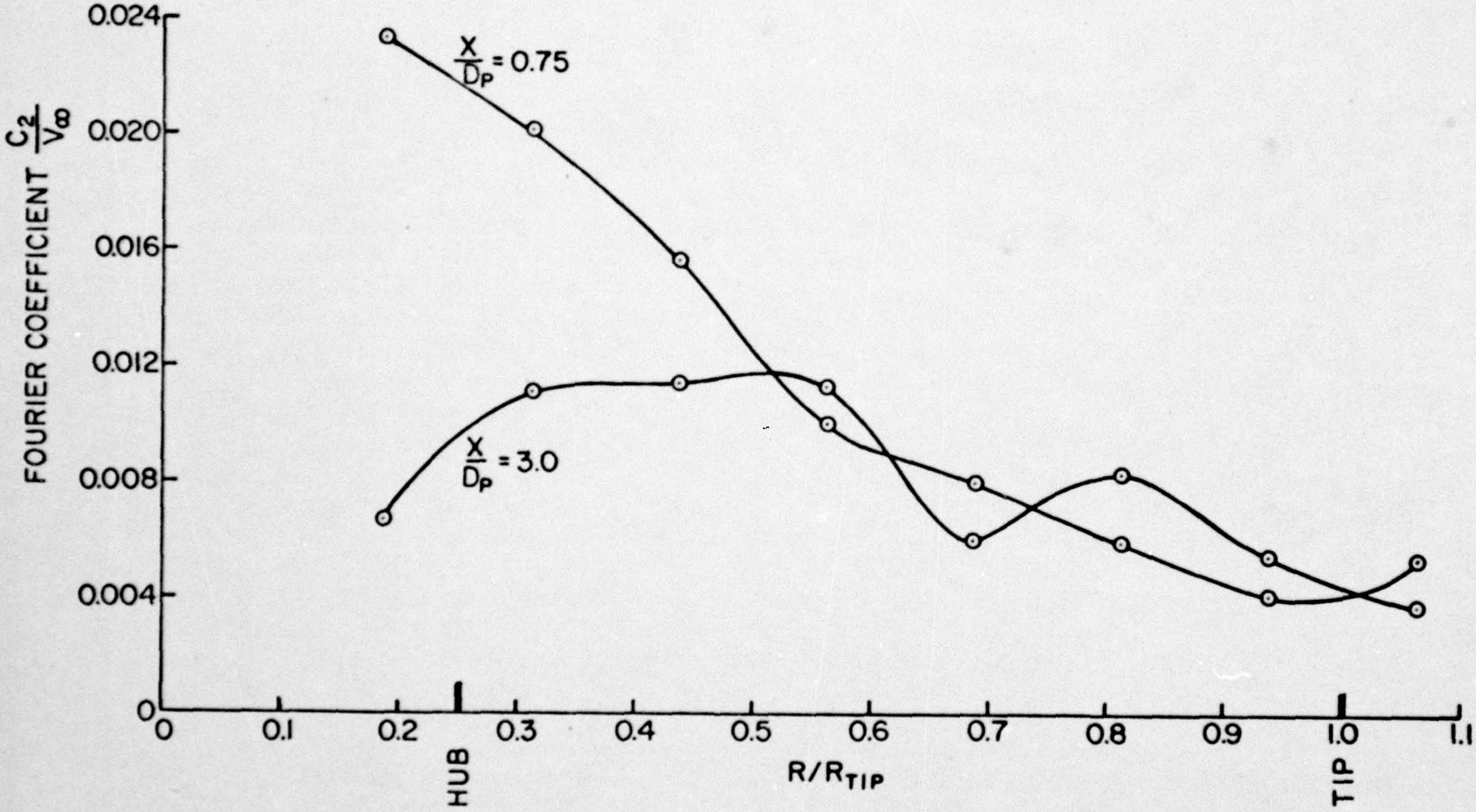

Figure 11 - Complex Fourier Coefficient C_2/V_∞ versus Non-dimensional Radius for Two Strut-to-Propeller Spacings

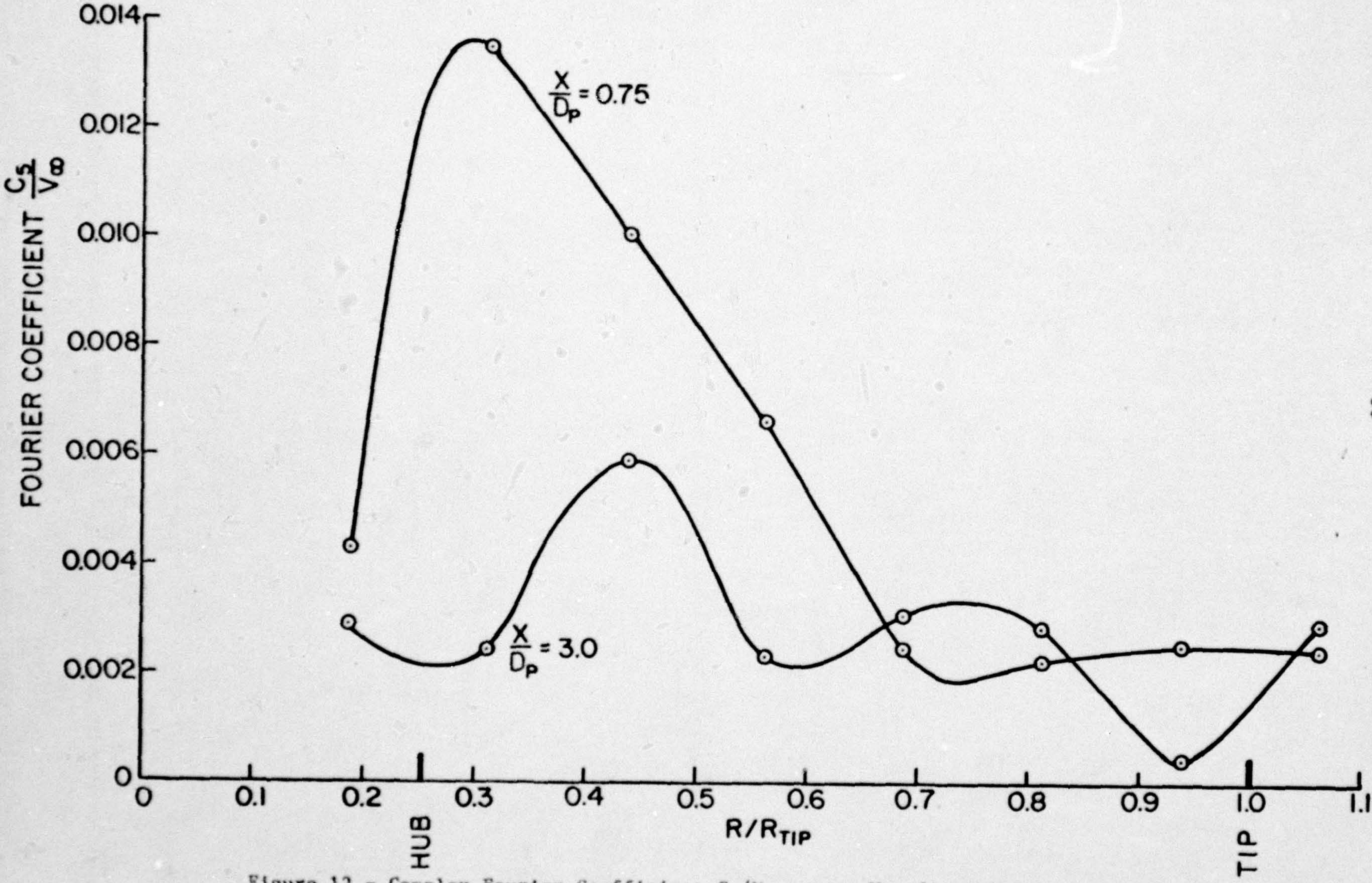

Figure 12 - Complex Fourier Coefficient C_5/V_∞ versus Non-dimensional Radius for Two Strut-to-Propeller Spacings

July 10, 1972
DET:mac

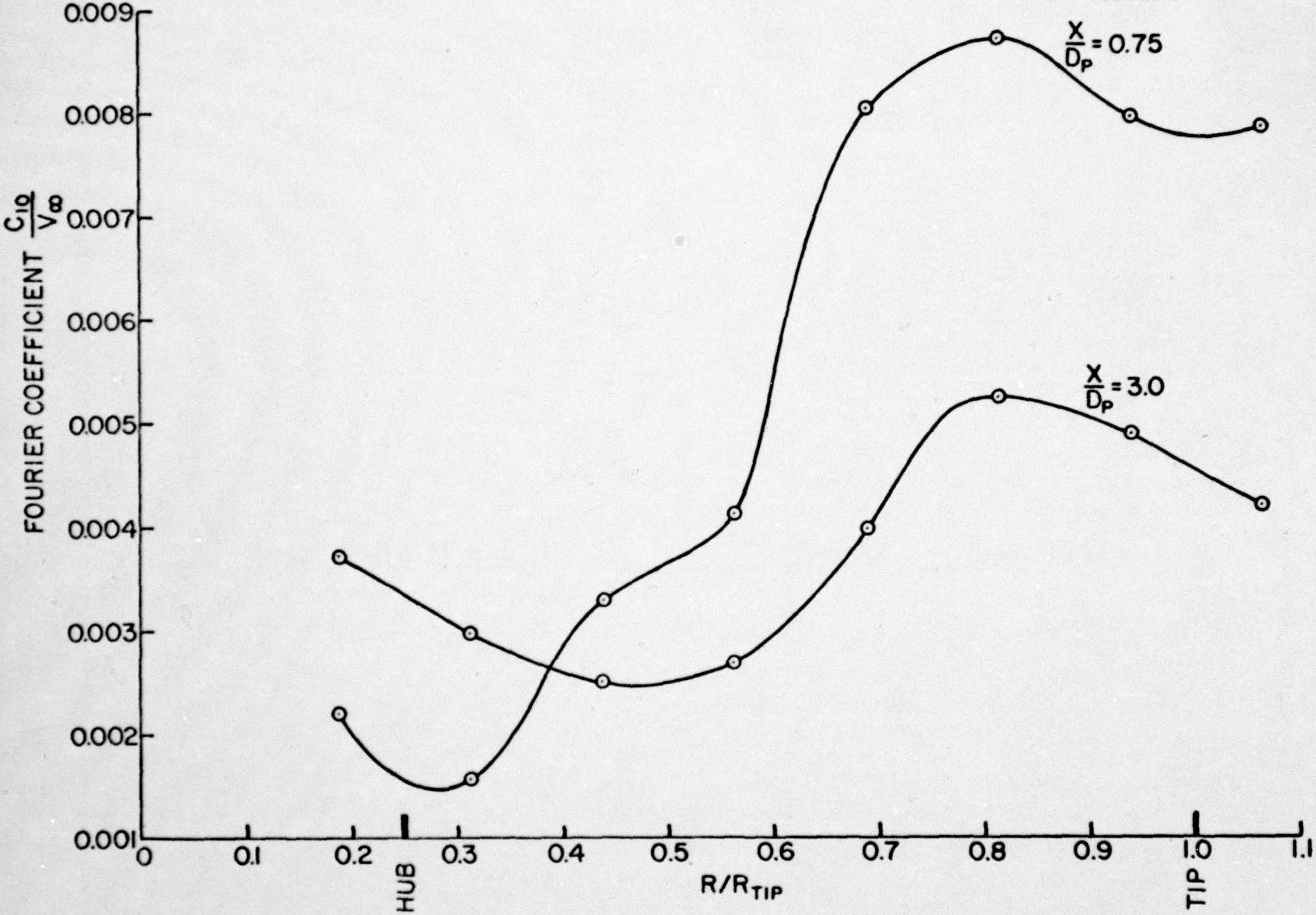

Figure 13 - Complex Fourier Coefficient C_{10}/V_∞ versus Non-Dimensional Radius for Two Strut-to-Propeller Spacings

July 10, 1972
DET:mac

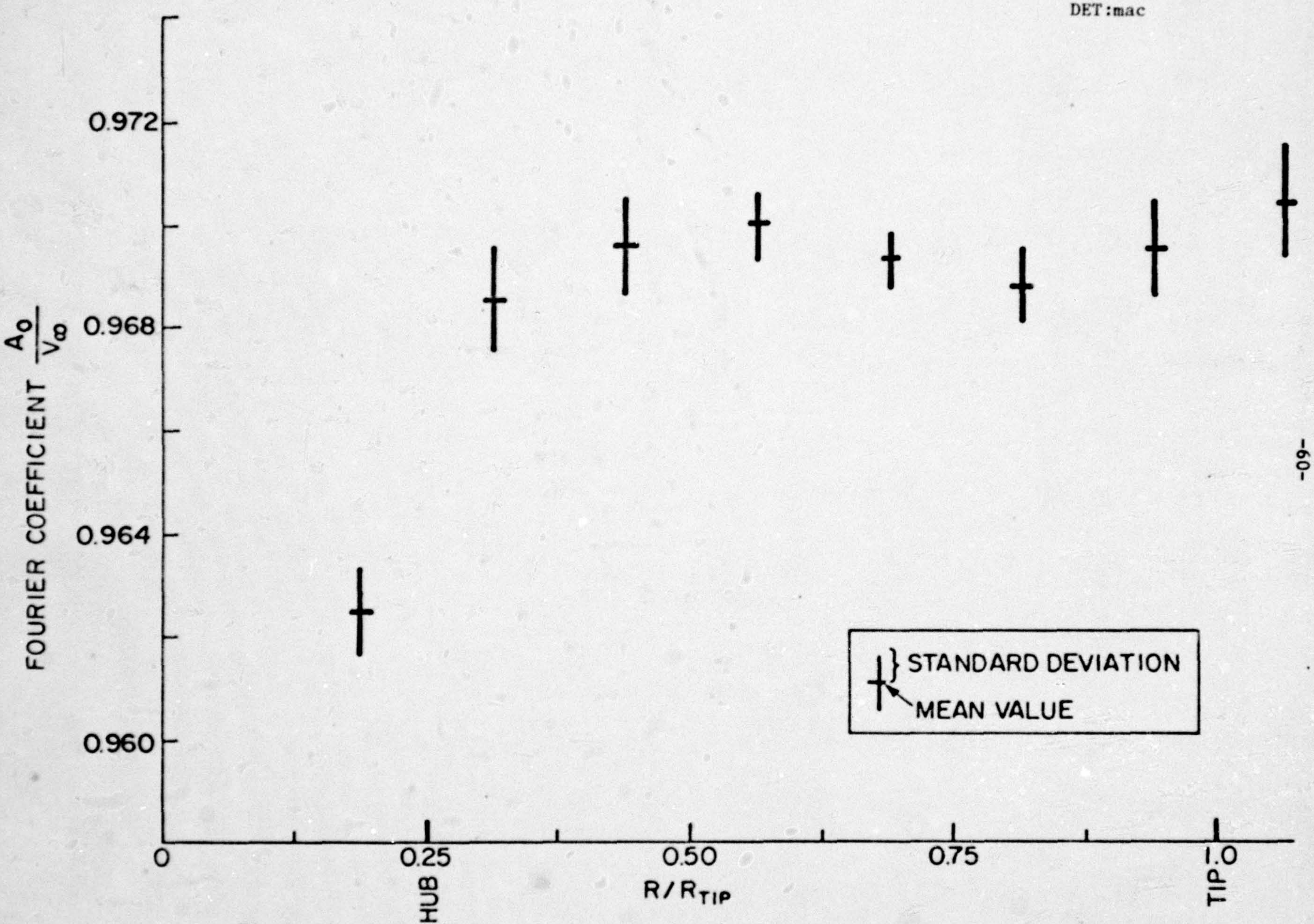

Figure 14 - Mean and Standard Deviation of Fourier Coefficient A_o/V_∞ versus Non-dimensional Radius

July 10, 1972
DET:mac

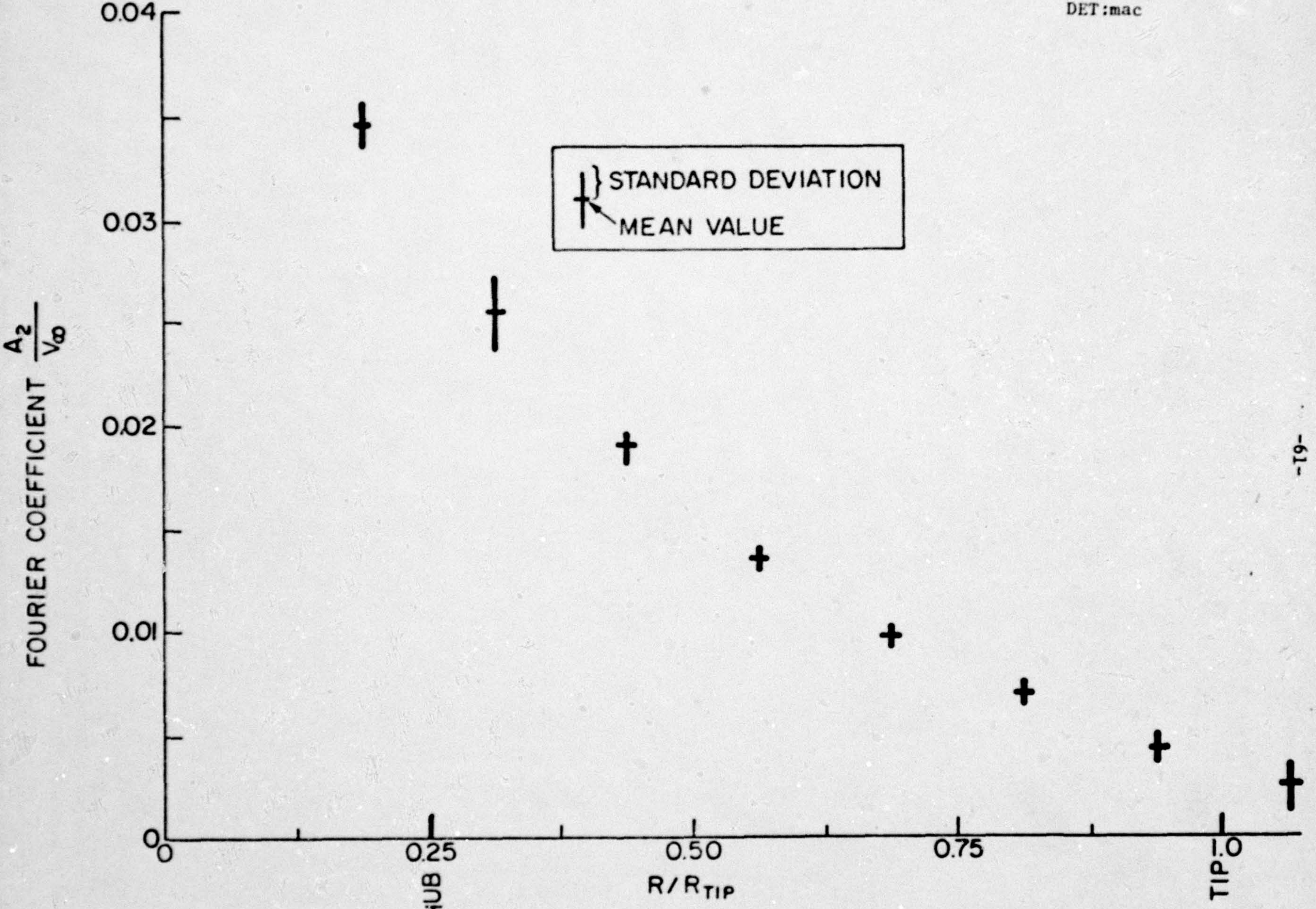

Figure 15 - Mean and Standard Deviation of Fourier Coefficient A_2/V_∞ versus Non-dimensional Radius

July 10, 1972
DET:mac

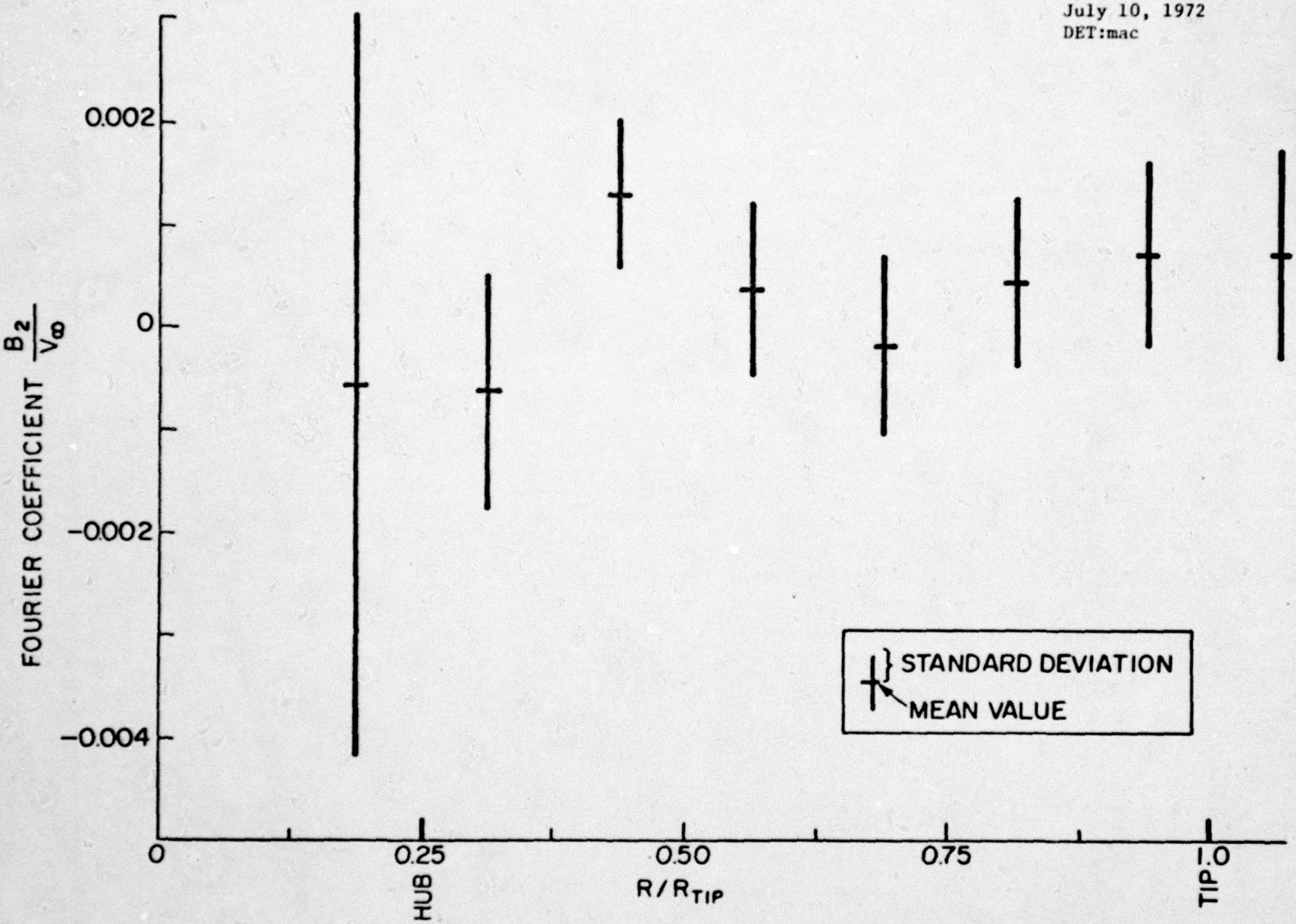

Figure 16 - Mean and Standard Deviation of Fourier Coefficient B_2/V_∞ versus Non-dimensional Radius

July 10, 1972
DET:mac

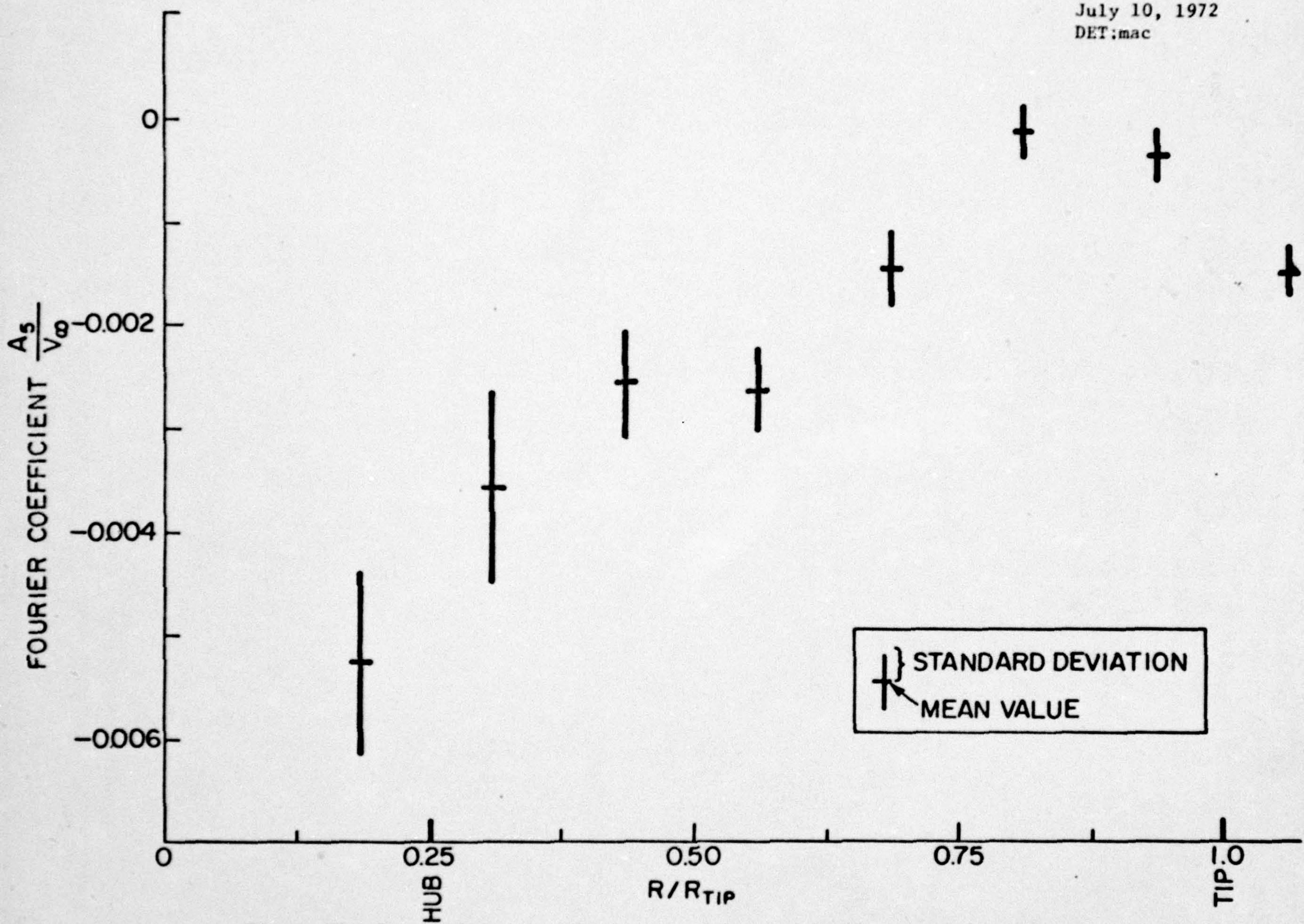

Figure 17 - Mean and Standard Deviation of Fourier Coefficient A_5/V_∞ versus Non-dimensional Radius

July 10, 1972
DET:mac

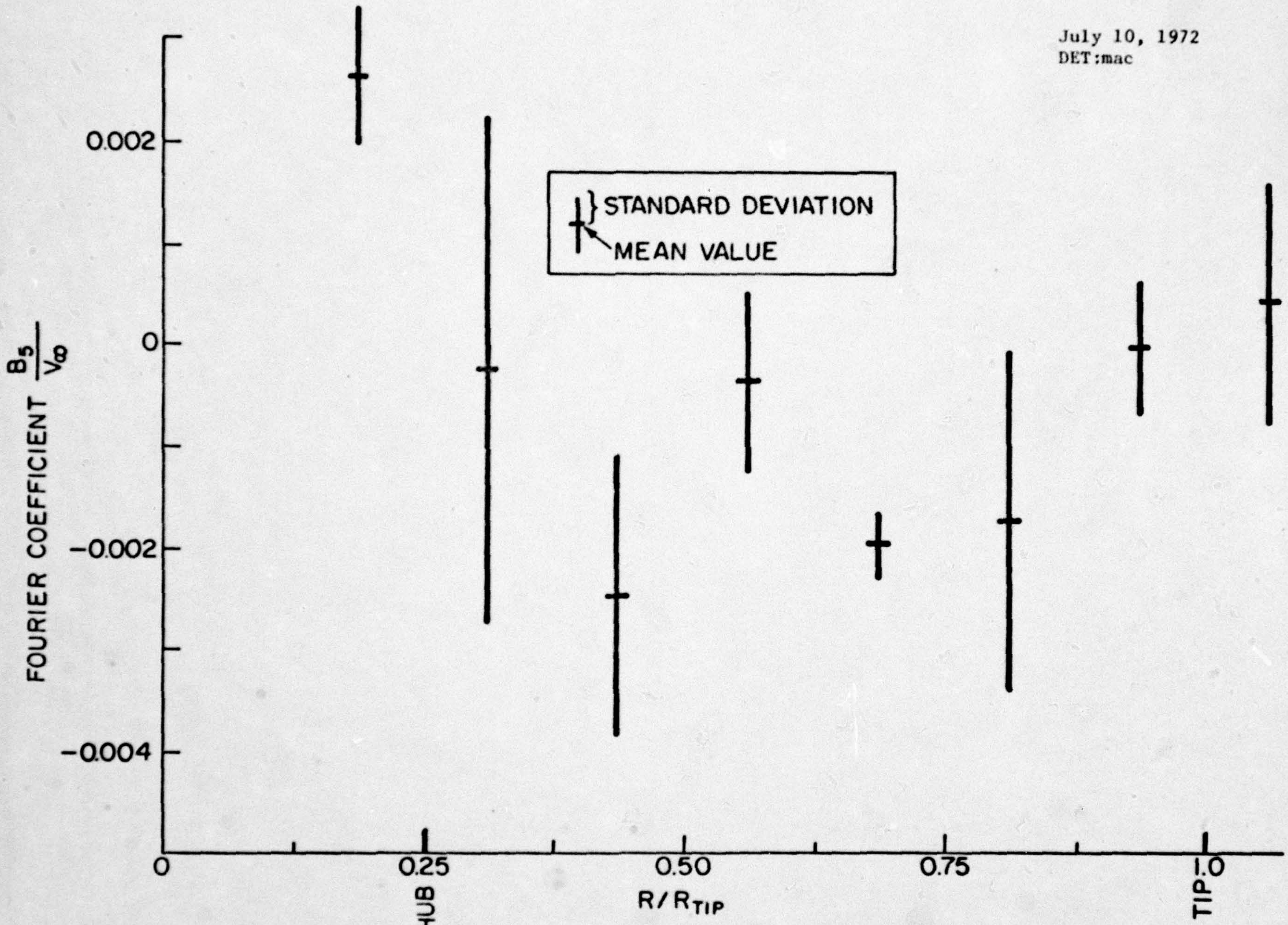

Figure 18 - Mean and Standard Deviation of Fourier Coefficient B_5/V_∞ versus Non-dimensional Radius

July 10, 1972
DET:mac

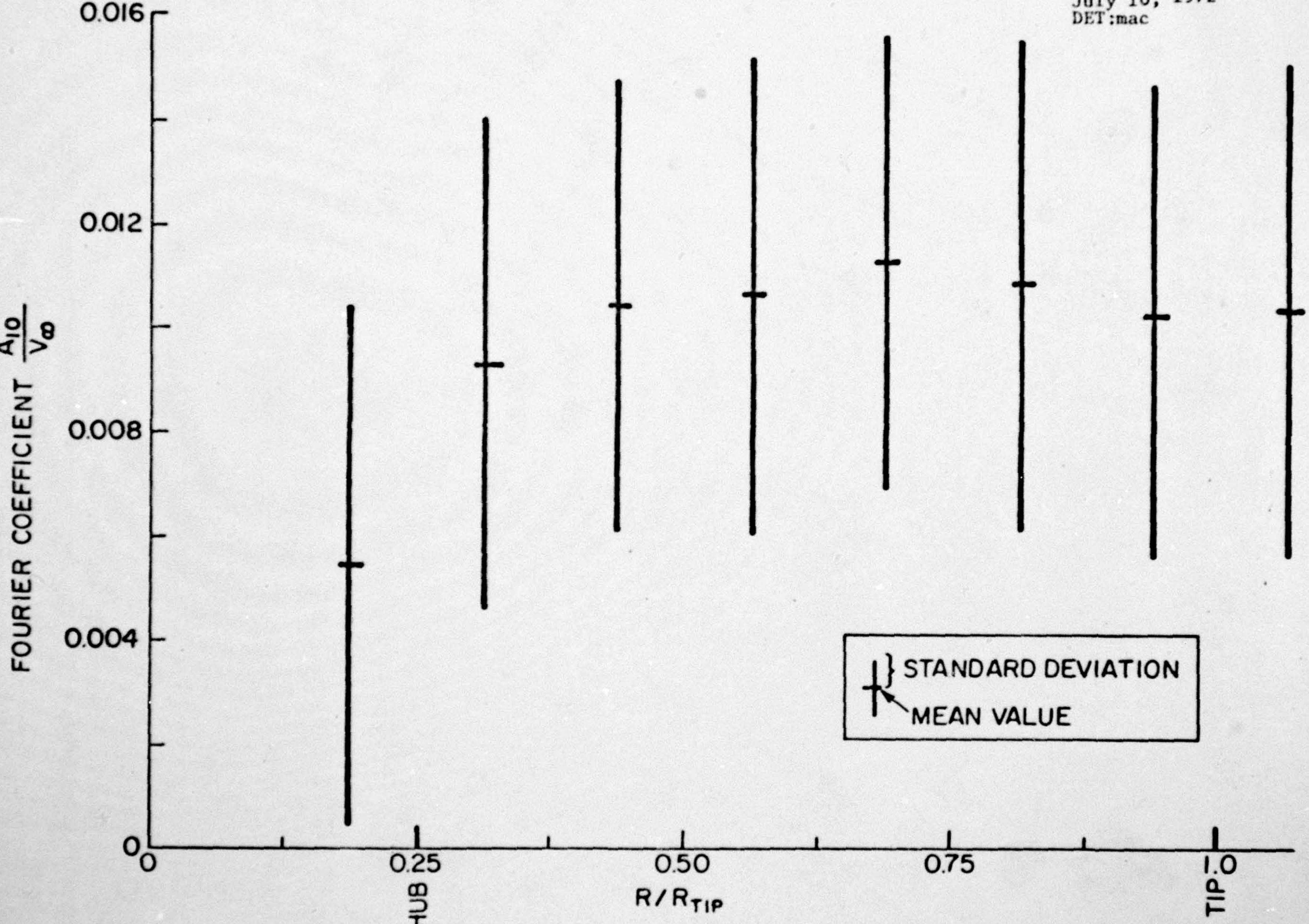

Figure 19 - Mean and Standard Deviation of Fourier Coefficient A_{10}/V_∞ versus Non-dimensional Radius

July 10, 1972
DET:mac

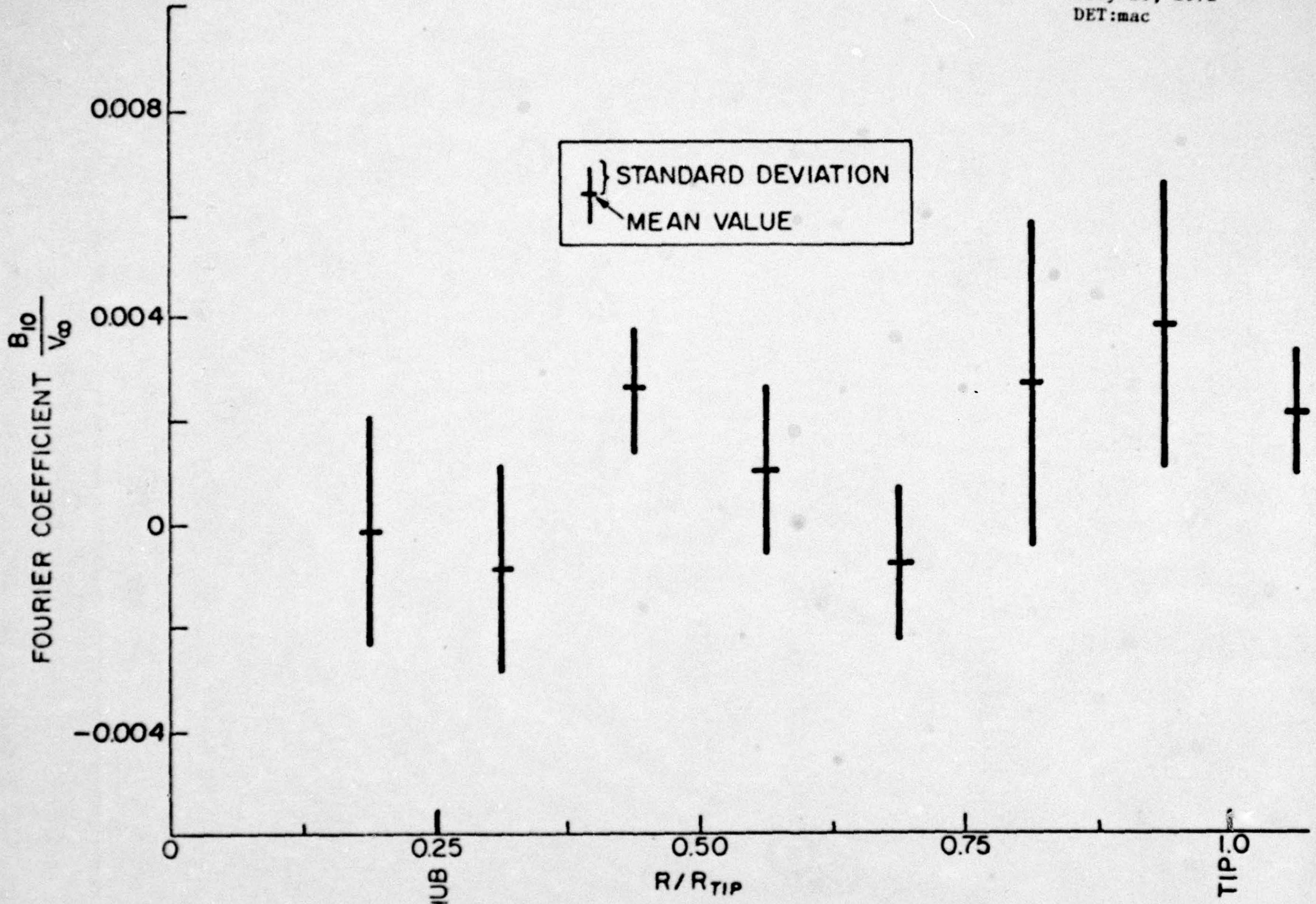

Figure 20 - Mean and Standard Deviation of Fourier Coefficient B_{10}/V_∞ versus Non-dimensional Radius

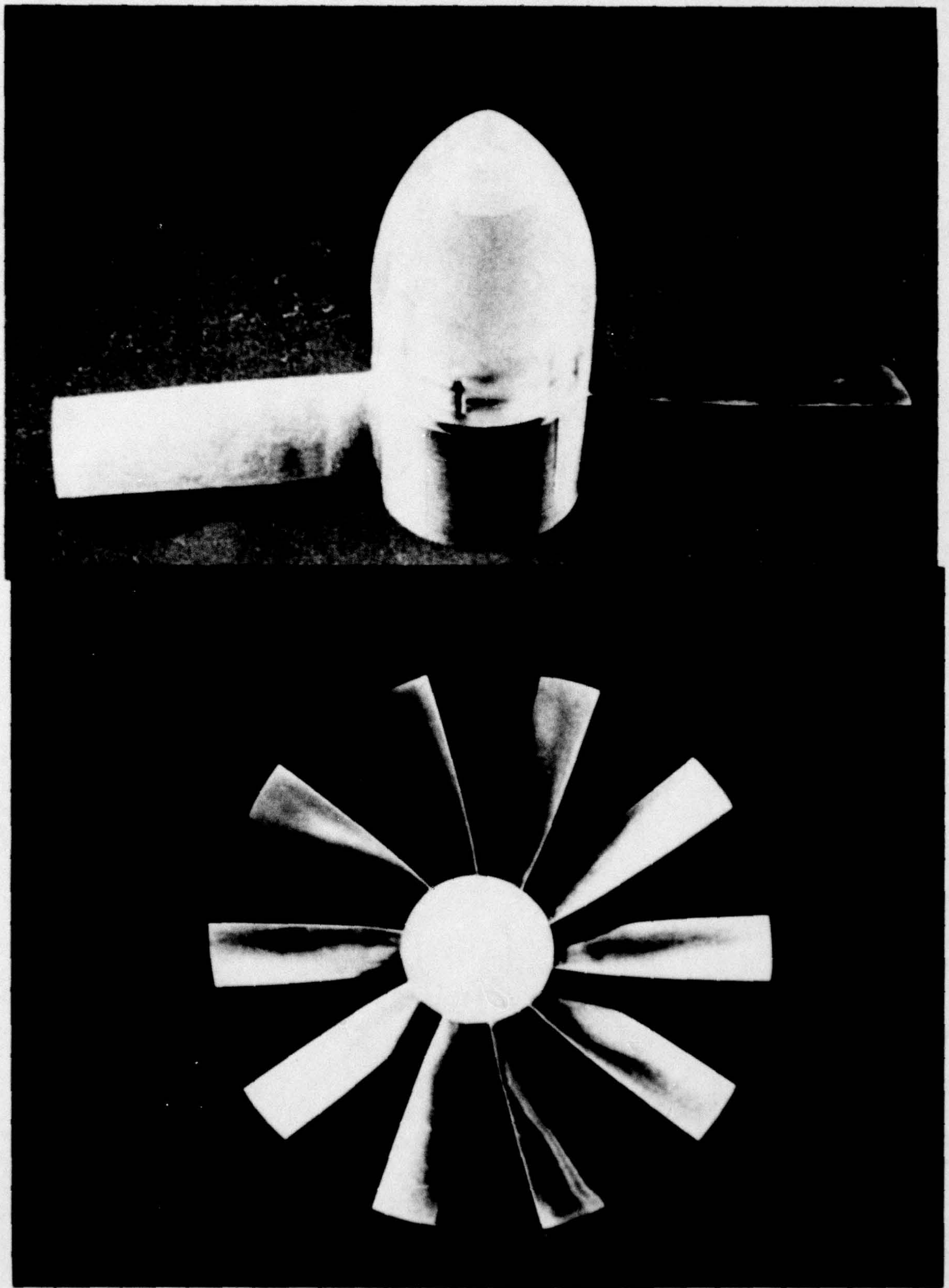

[illegible]

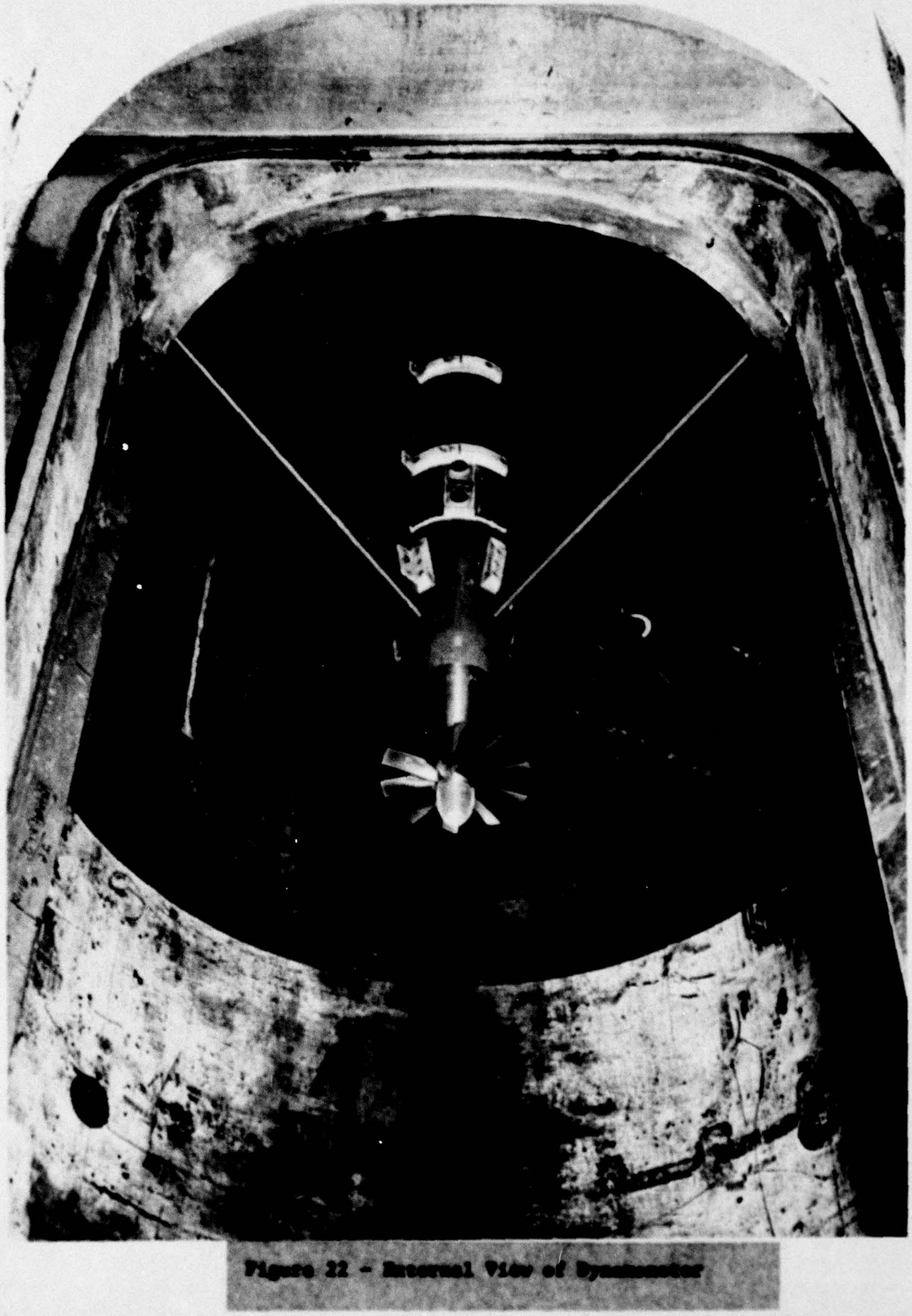

Figure 22 - Internal View of Dynamometer

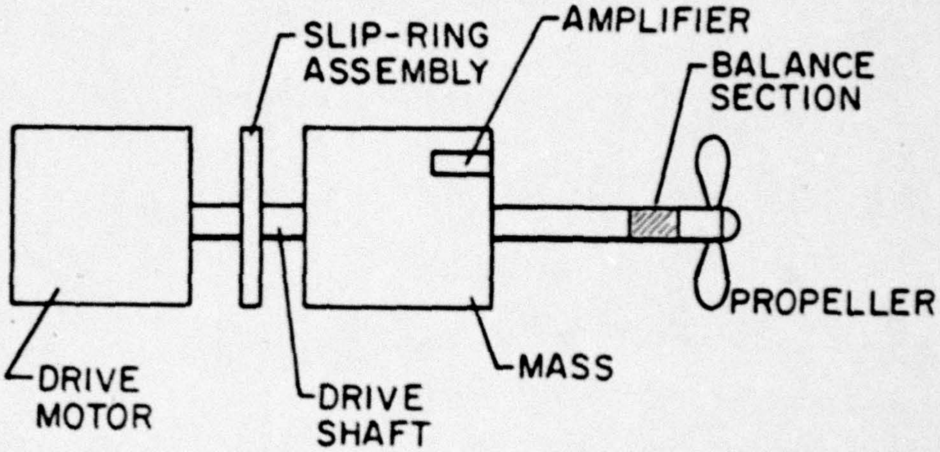

Figure 23 - Internal View of Dynamometer

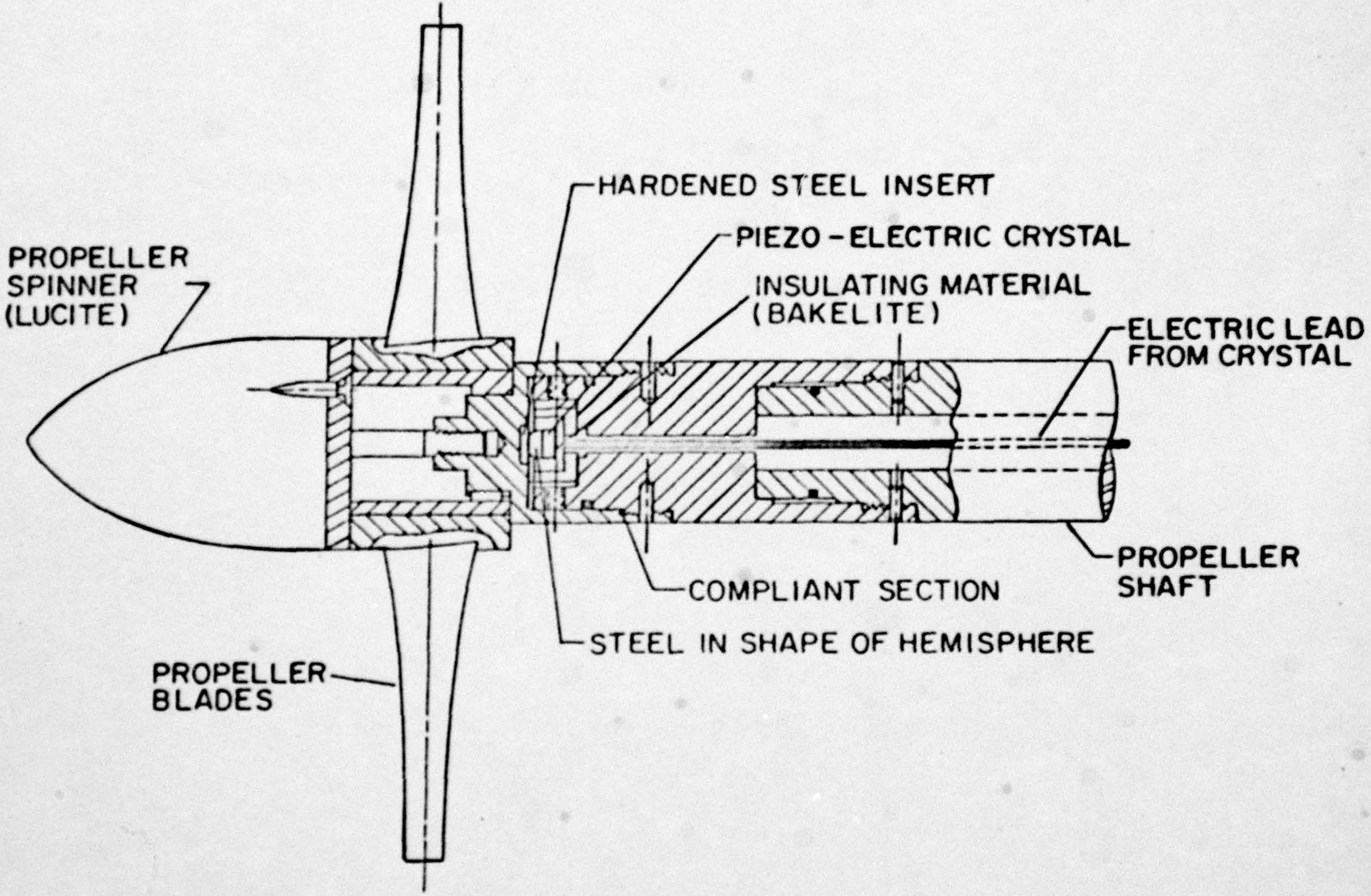

Figure 24 - Detailed Drawing of Time-Dependent Thrust Balance

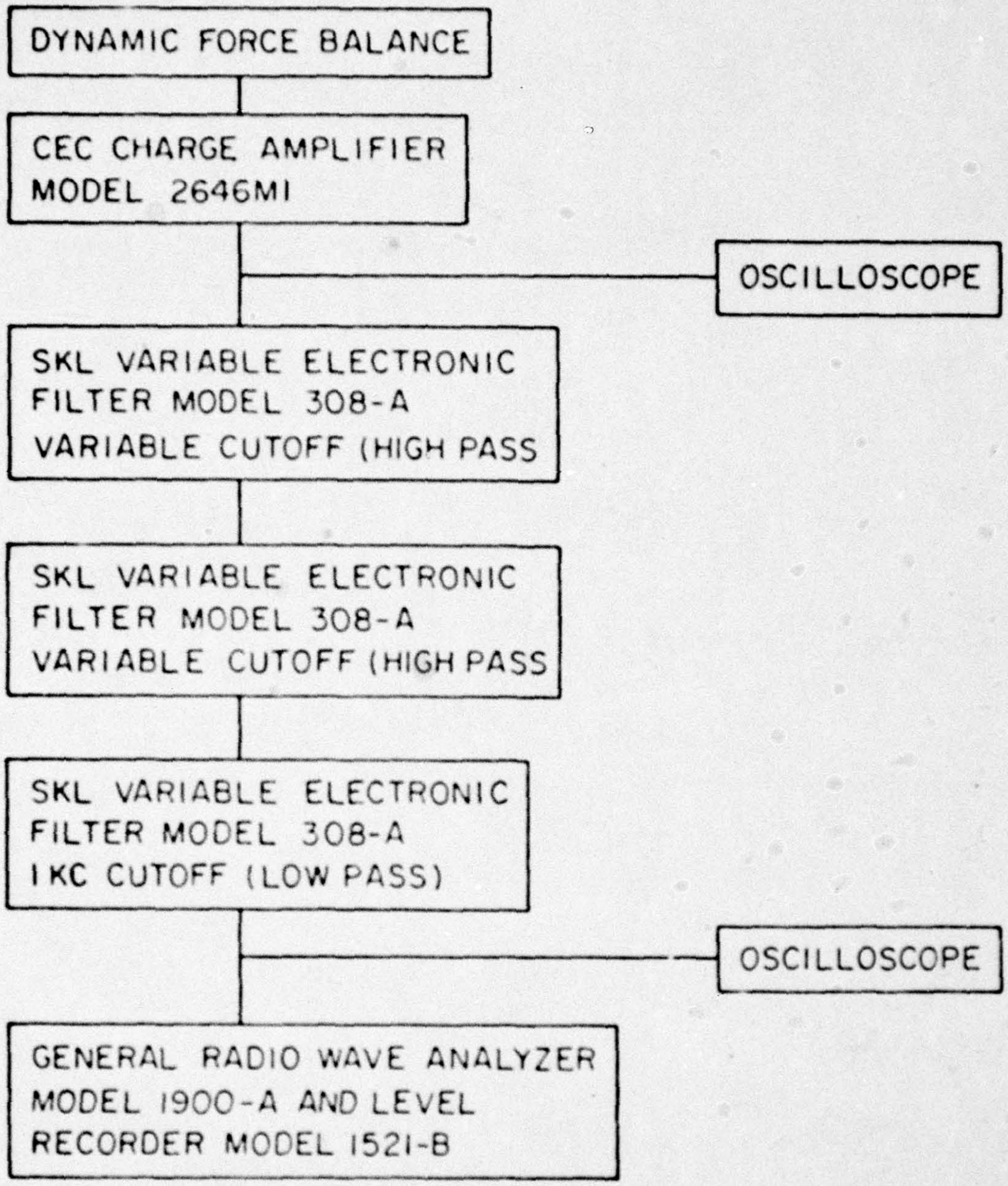

Figure 25 - Data Acquisition and Reduction System for Time-Dependent Thrust Measurement

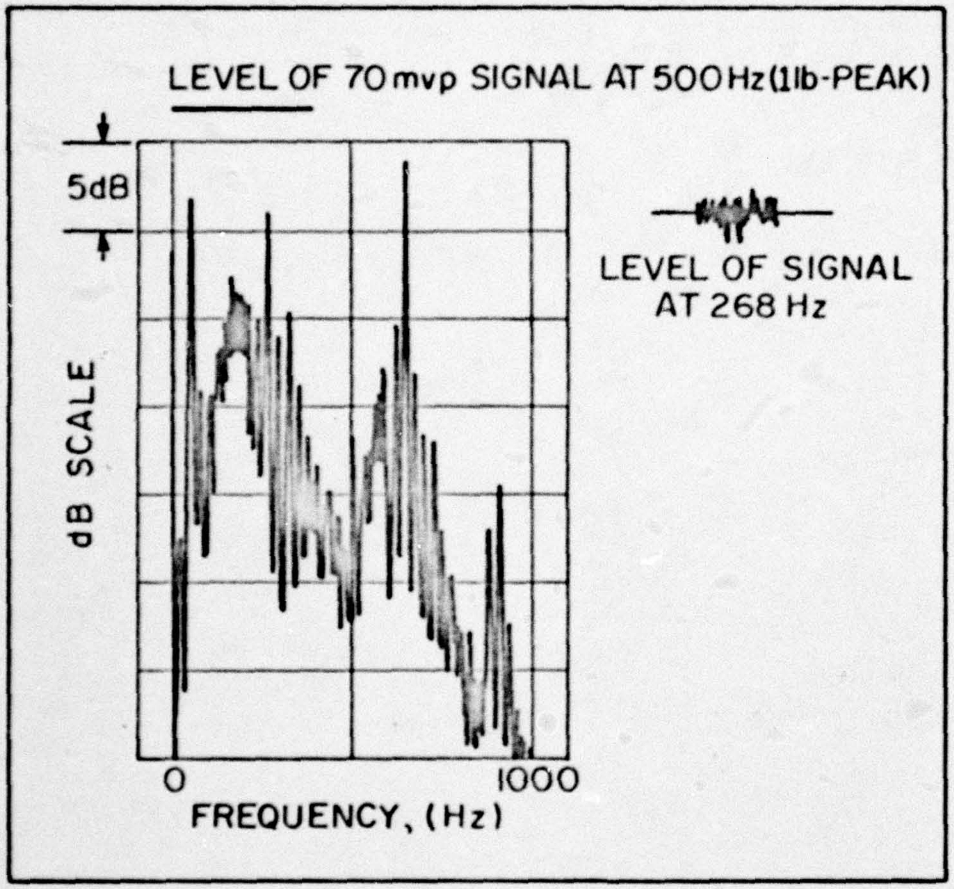

TEST CONDITIONS
10 BLADED PROPELLER
V_{∞} = 21 ft/sec
J = 1.17
STRUT 6 inches FORWARD OF PROPELLER

Figure 26 - Frequency Spectrum of Time-Dependent Thrust Signal, Blade-Rate Frequency Signal Level and Level of Calibration Signal

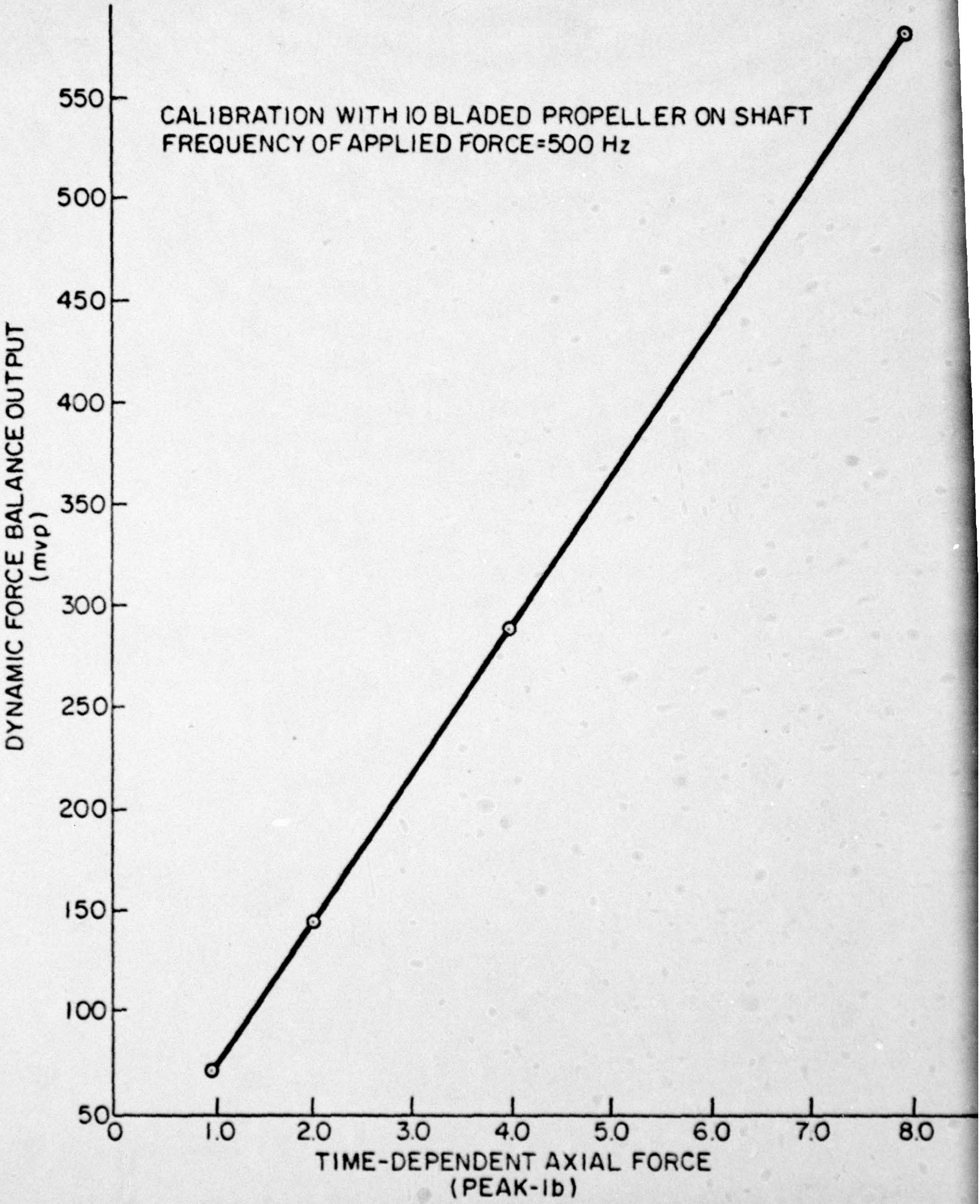

Figure 27 - Typical Calibration Curve

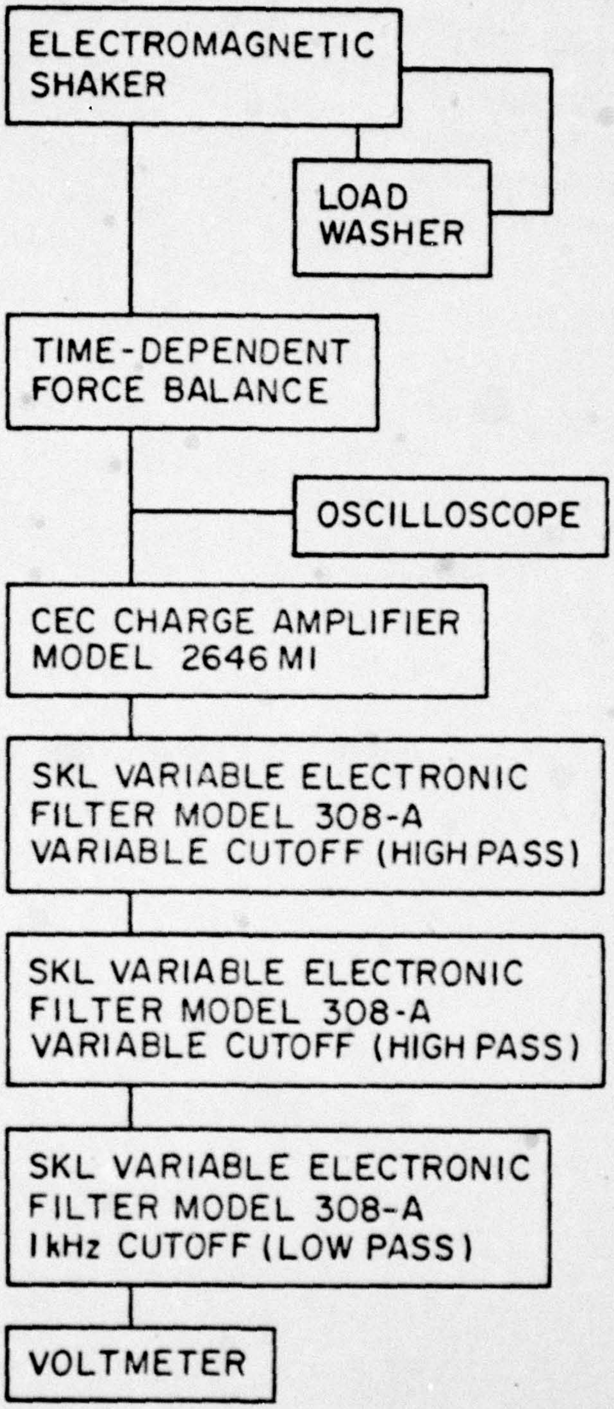

Figure 28 - Apparatus for Calibration

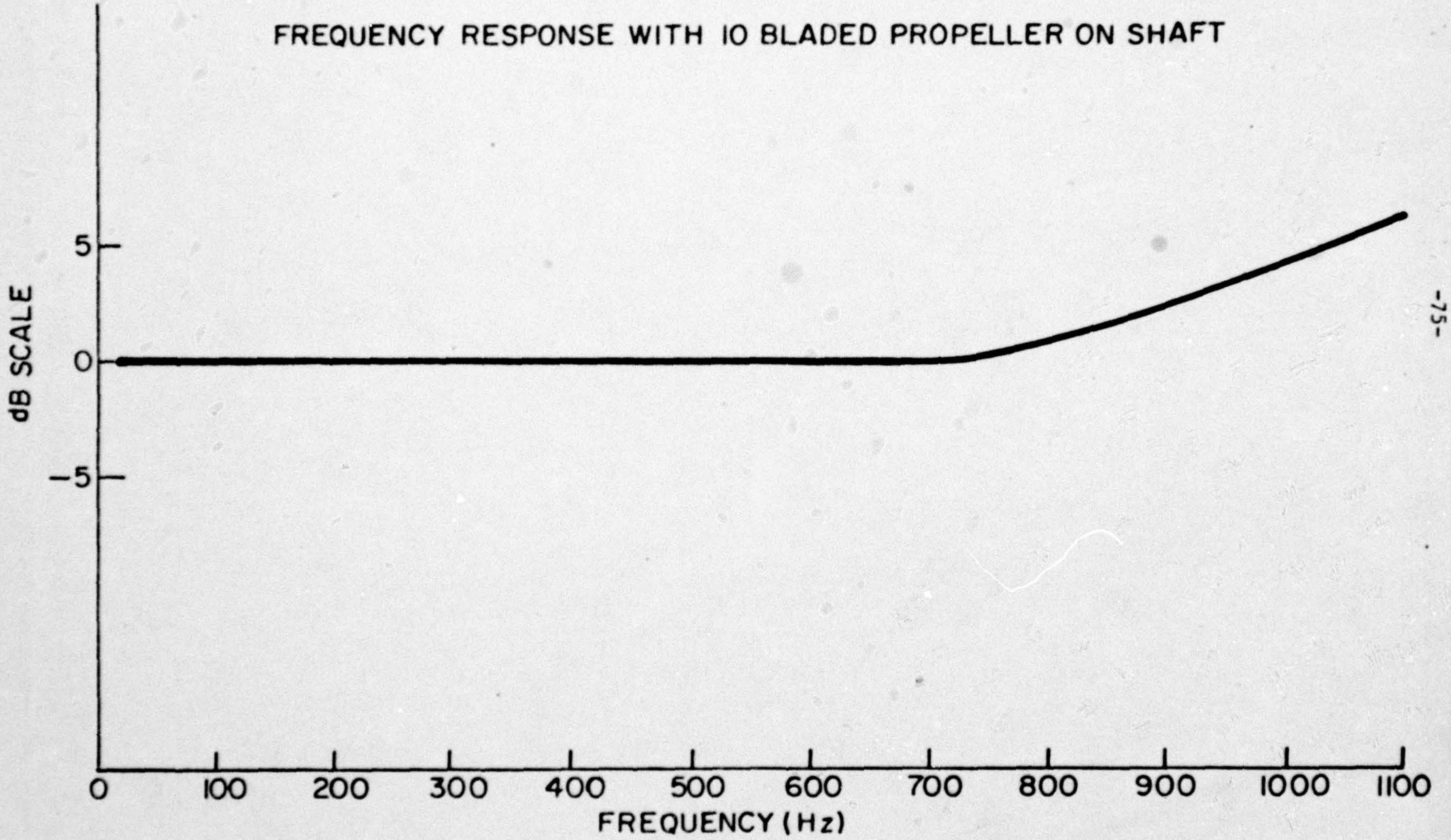

Figure 29 - Frequency Response of Time-Dependent Thrust Balance

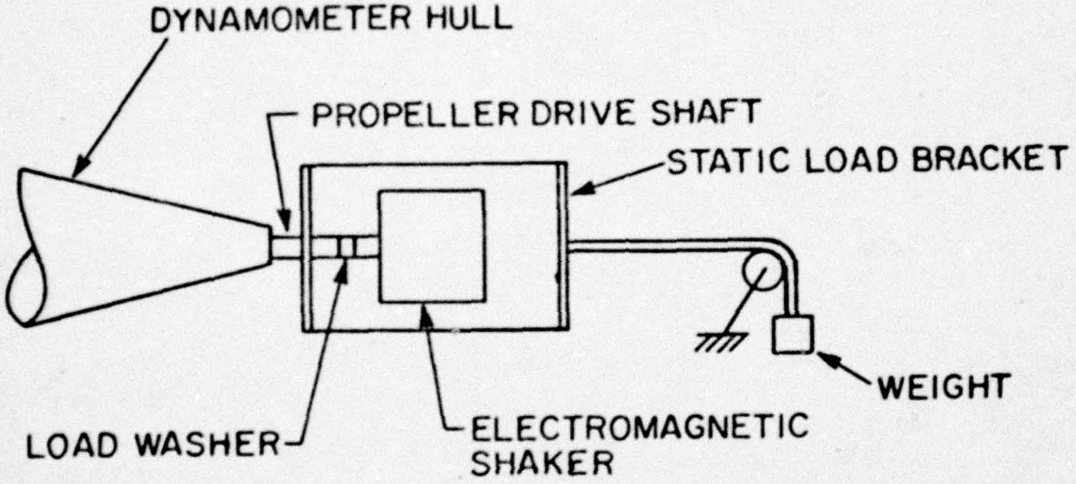

Figure 30 - Apparatus for Calibration of Time-Dependent Thrust Balance with Applied Steady Axial Force

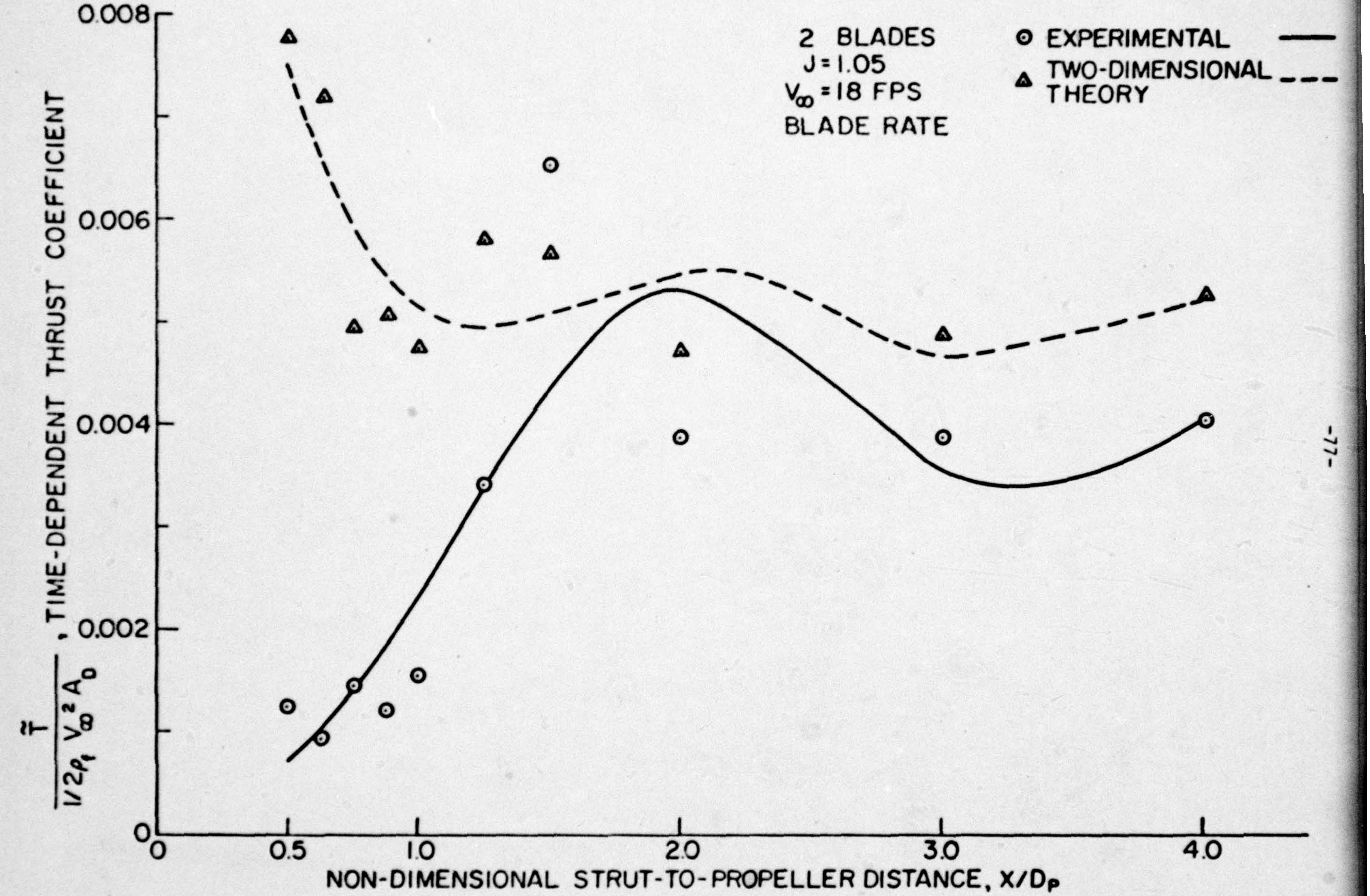

Figure 31 - Single-Amplitude Time-Dependent Thrust Coefficient versus Strut-to-Propeller Distance for Two-Bladed Propeller, J = 1.05, V_∞ = 18 fps

July 10, 1972
DET:mac

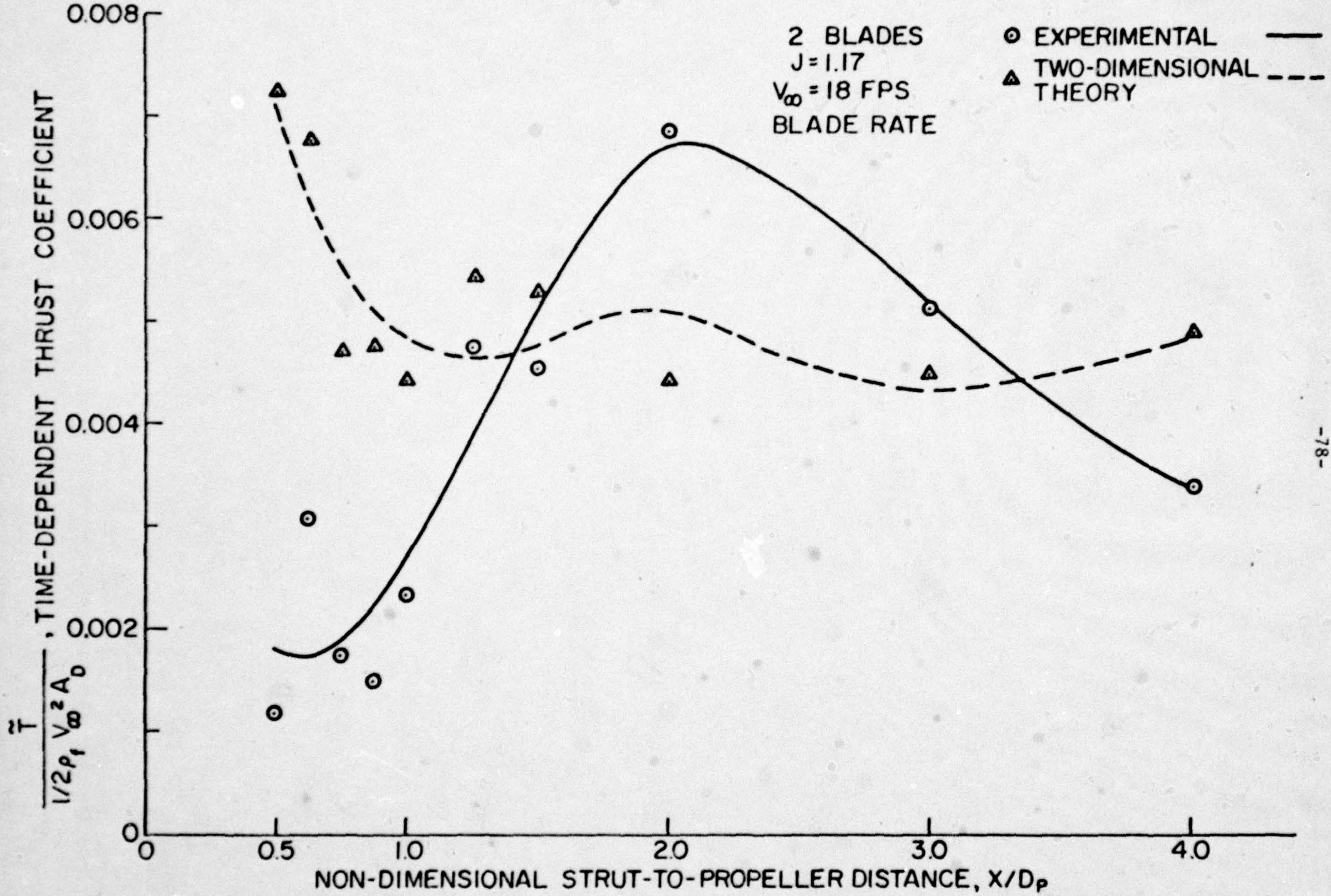

Figure 32 - Single-Amplitude Time-Dependent Thrust Coefficient versus Strut-to-Propeller Distance for Two-Bladed Propeller, J = 1.17, V_∞ = 18 fps

July 10, 1972
DET:mac

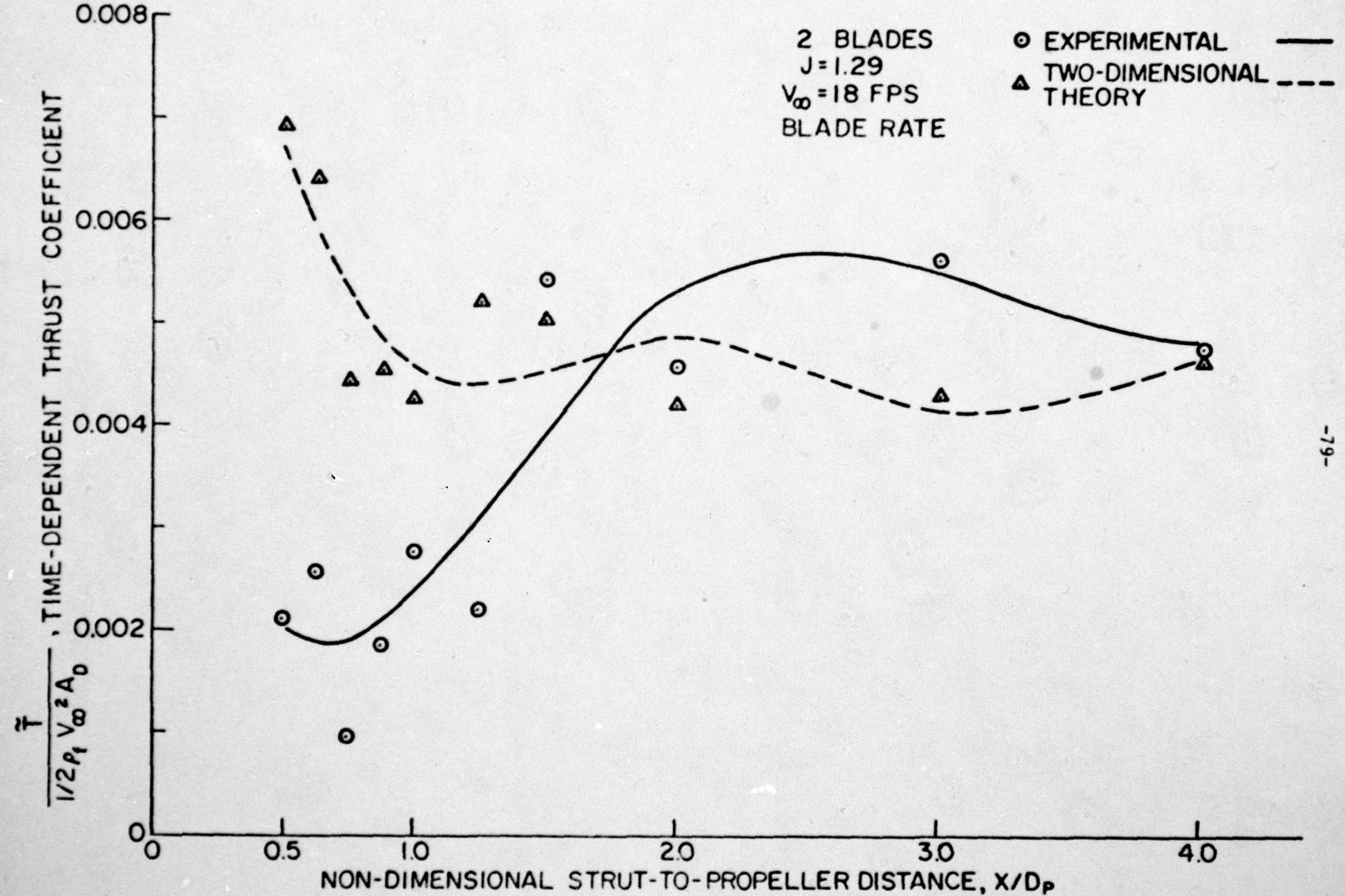

Figure 33 - Single-Amplitude Time-Dependent Thrust Coefficient versus Strut-to-Propeller Distance for Two-Bladed Propeller, $J = 1.29$, $V_\infty = 18$ fps

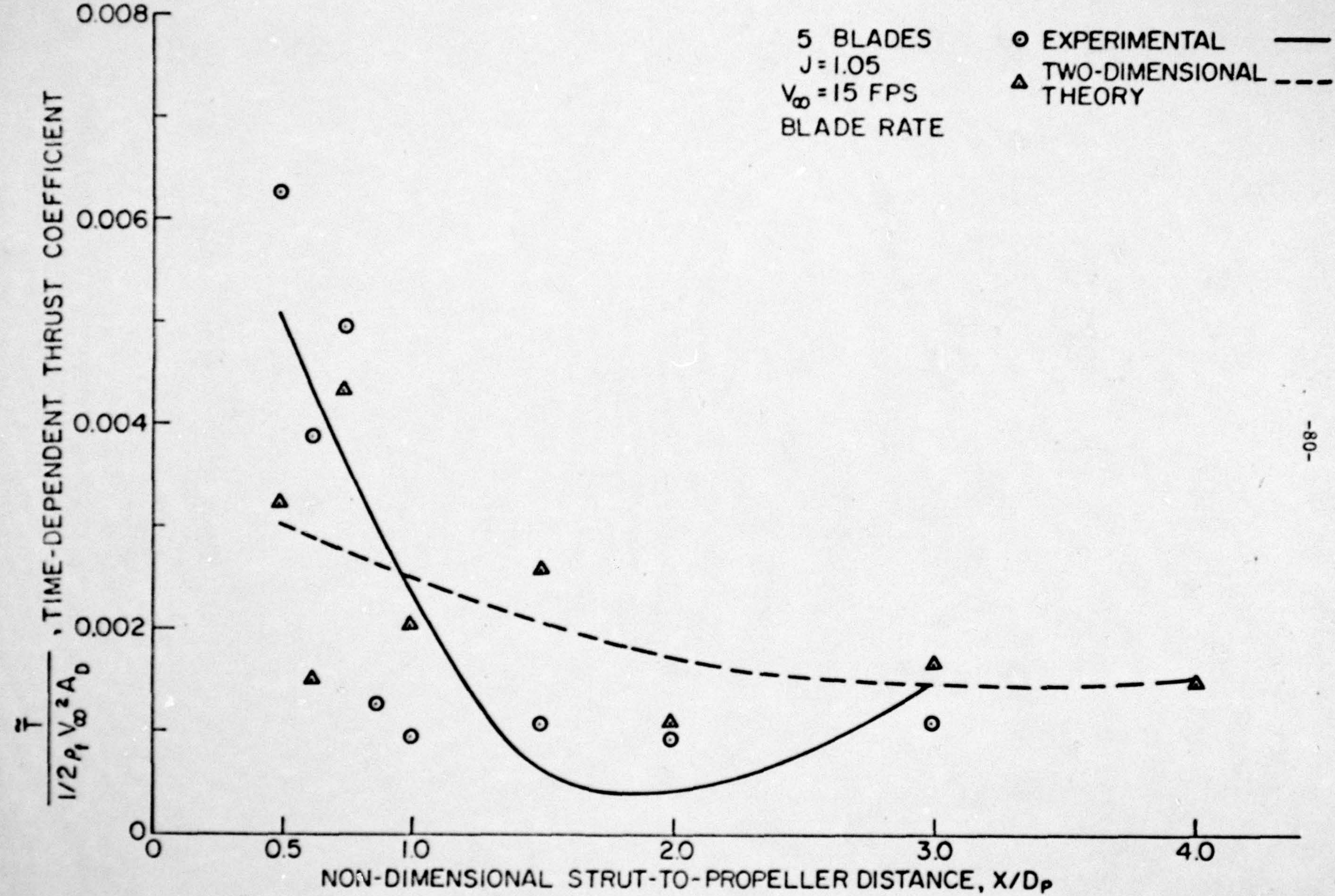

Figure 34 - Single-Amplitude Time-Dependent Thrust Coefficient versus Strut-to-Propeller Distance for Five-Bladed Propeller, J = 1.05, V_∞ = 15 fps

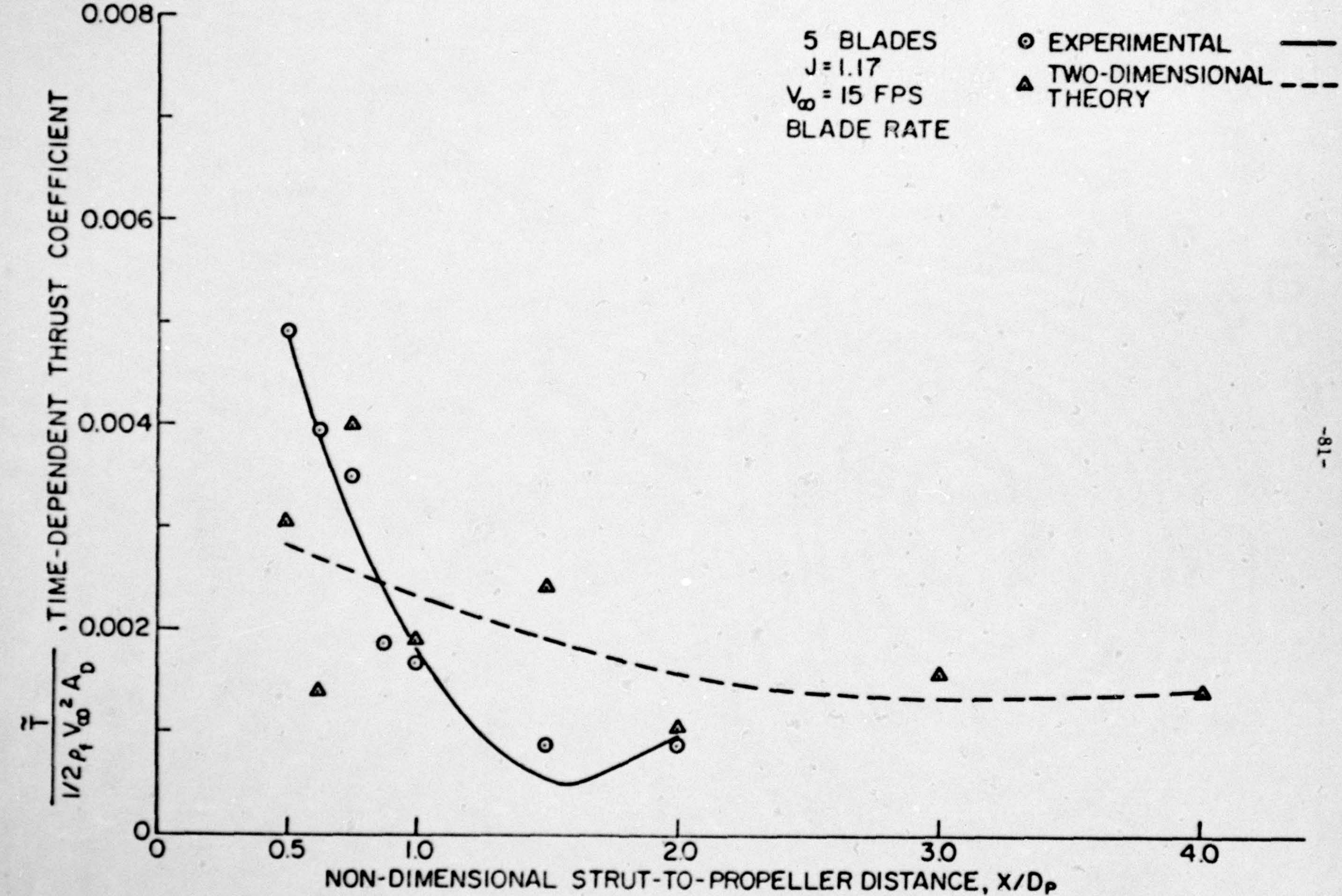

Figure 35 - Single-Amplitude Time-Dependent Thrust Coefficient versus Strut-to-Propeller Distance for Five-Bladed Propeller, J = 1.17, V_∞ = 15 fps

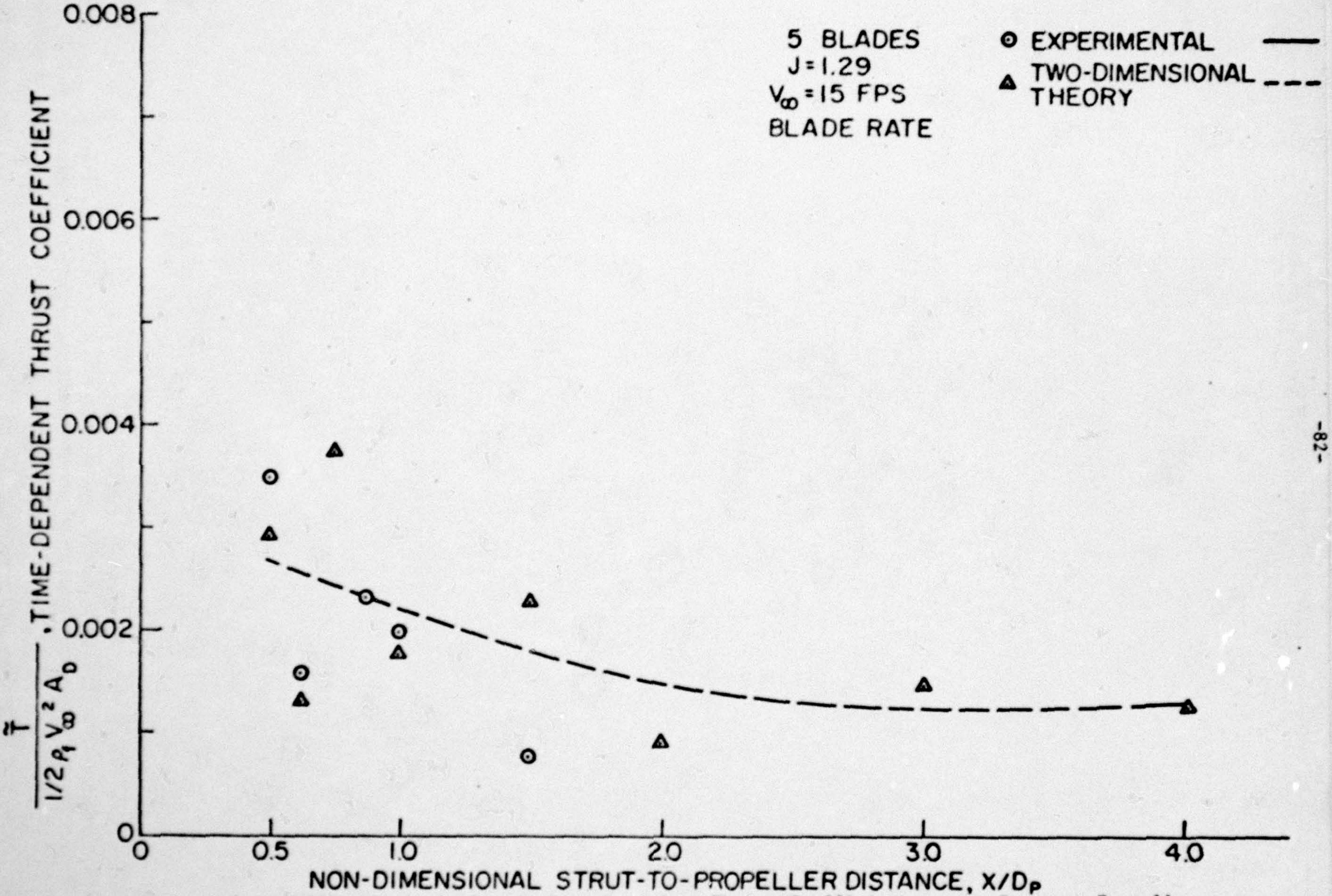

Figure 36 - Single-Amplitude Time-Dependent Thrust Coefficient versus Strut-to-Propeller Distance for Five-Bladed Propeller, J = 1.29, V_∞ = 15 fps

July 10, 1972
DET:mac

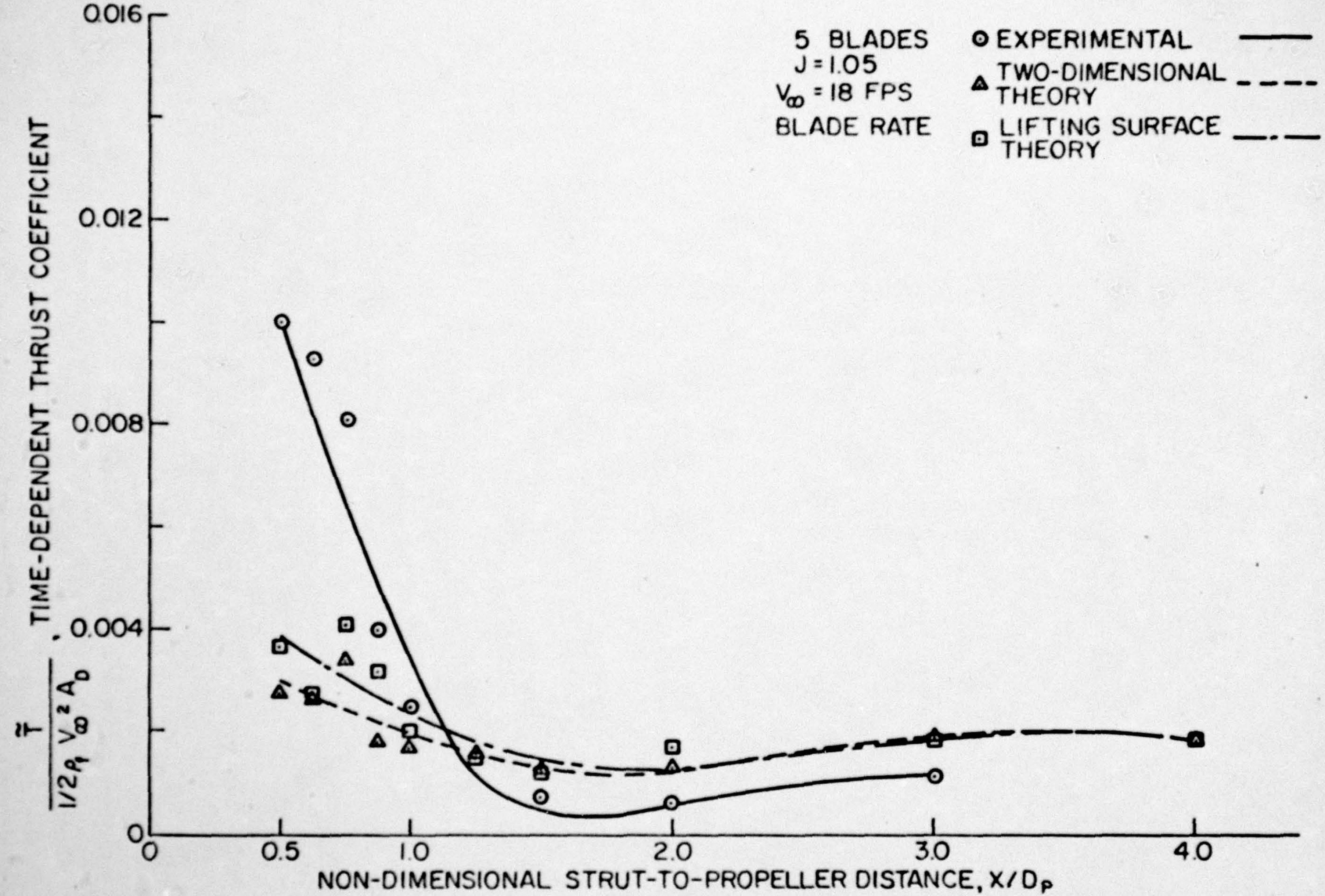

Figure 37 - Single-Amplitude Time-Dependent Thrust Coefficient versus Strut-to-Propeller Distance for Five-Bladed Propeller, J = 1.05, V_∞ = 18 fps

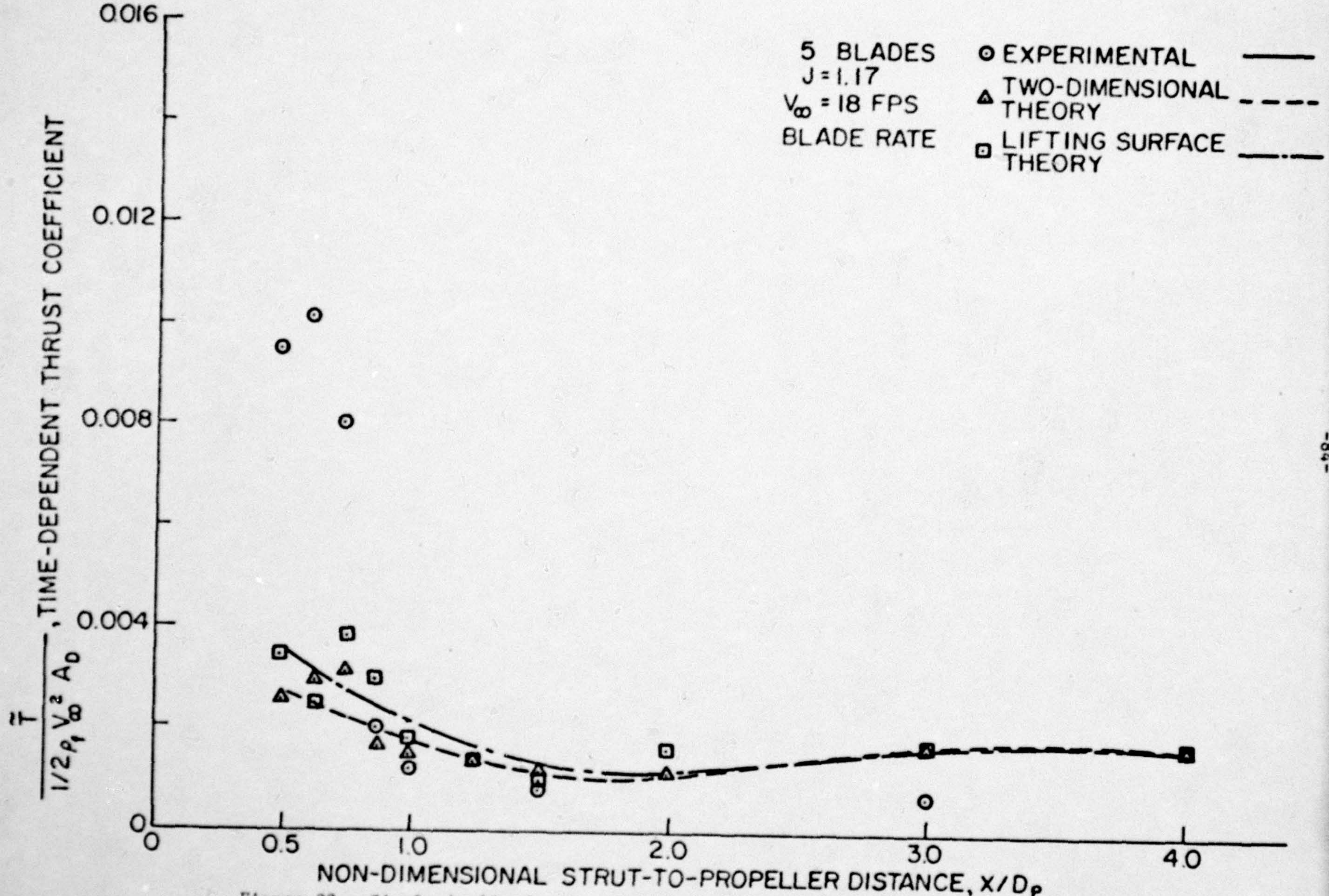

Figure 38 - Single-Amplitude Time-Dependent Thrust Coefficient versus Strut-to-Propeller Distance for Five-Bladed Propeller, J = 1.17, V_∞ = 18 fps

July 10, 1972
DET:mac

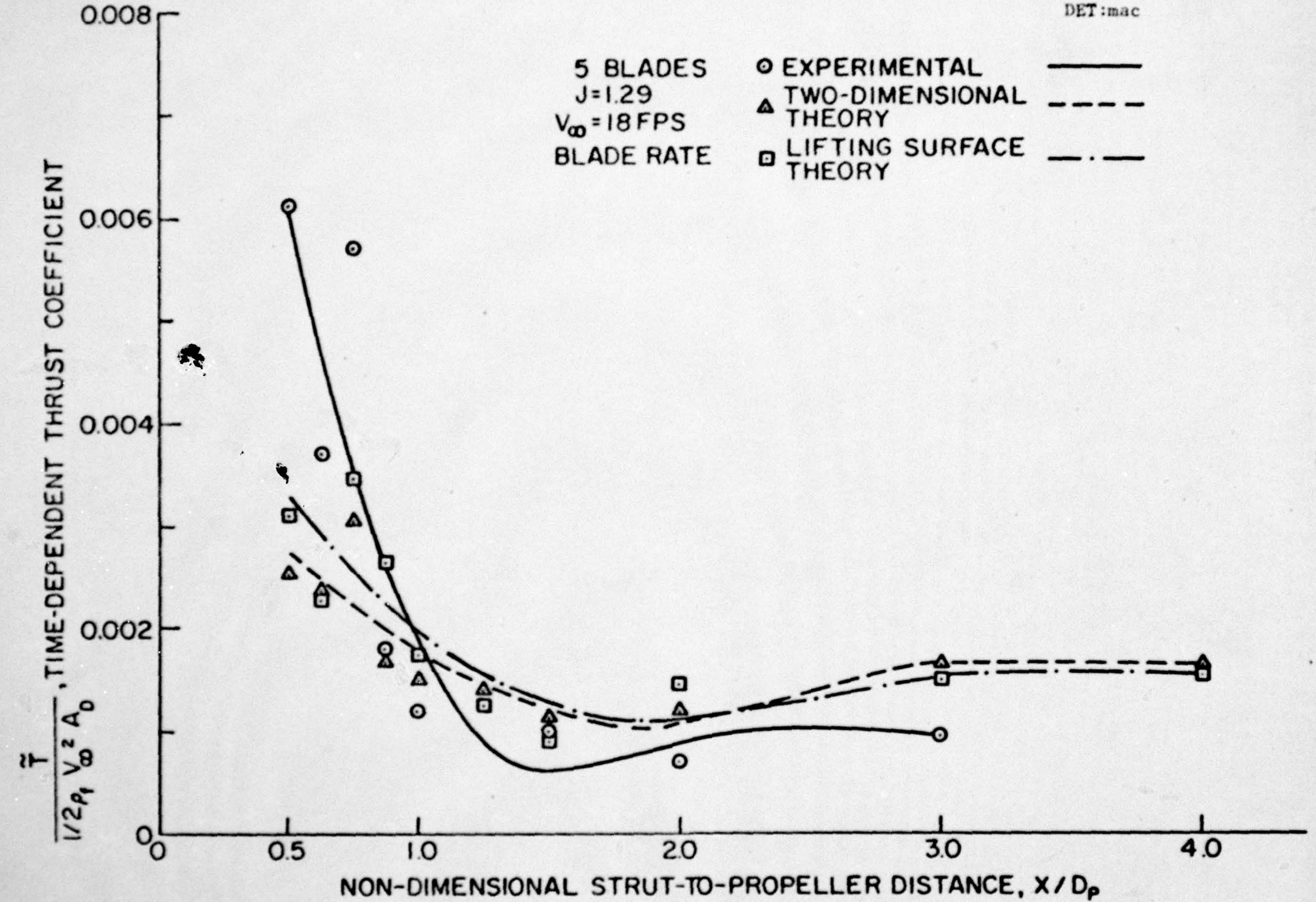

Figure 39 - Single-Amplitude Time-Dependent Thrust Coefficient versus Strut-to-Propeller Distance for Five-Bladed Propeller, J = 1.29, V_∞ = 18 fps

July 10, 1972
DET:mac

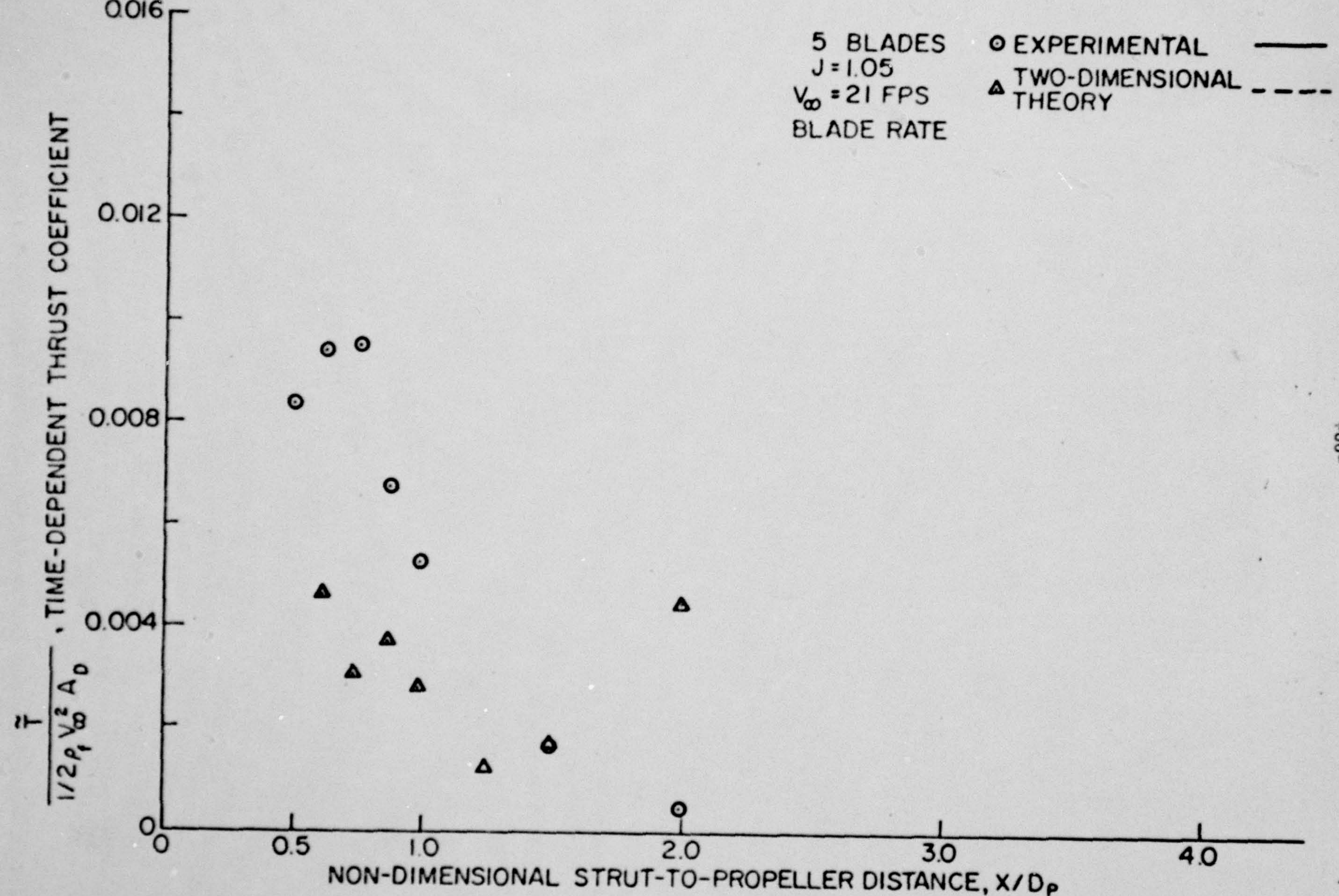

Figure 40 - Single-Amplitude Time-Dependent Thrust Coefficient versus Strut-to-Propeller Distance for Five-Bladed Propeller, J = 1.05, V_∞ = 21 fps

July 10, 1972
DET:mac

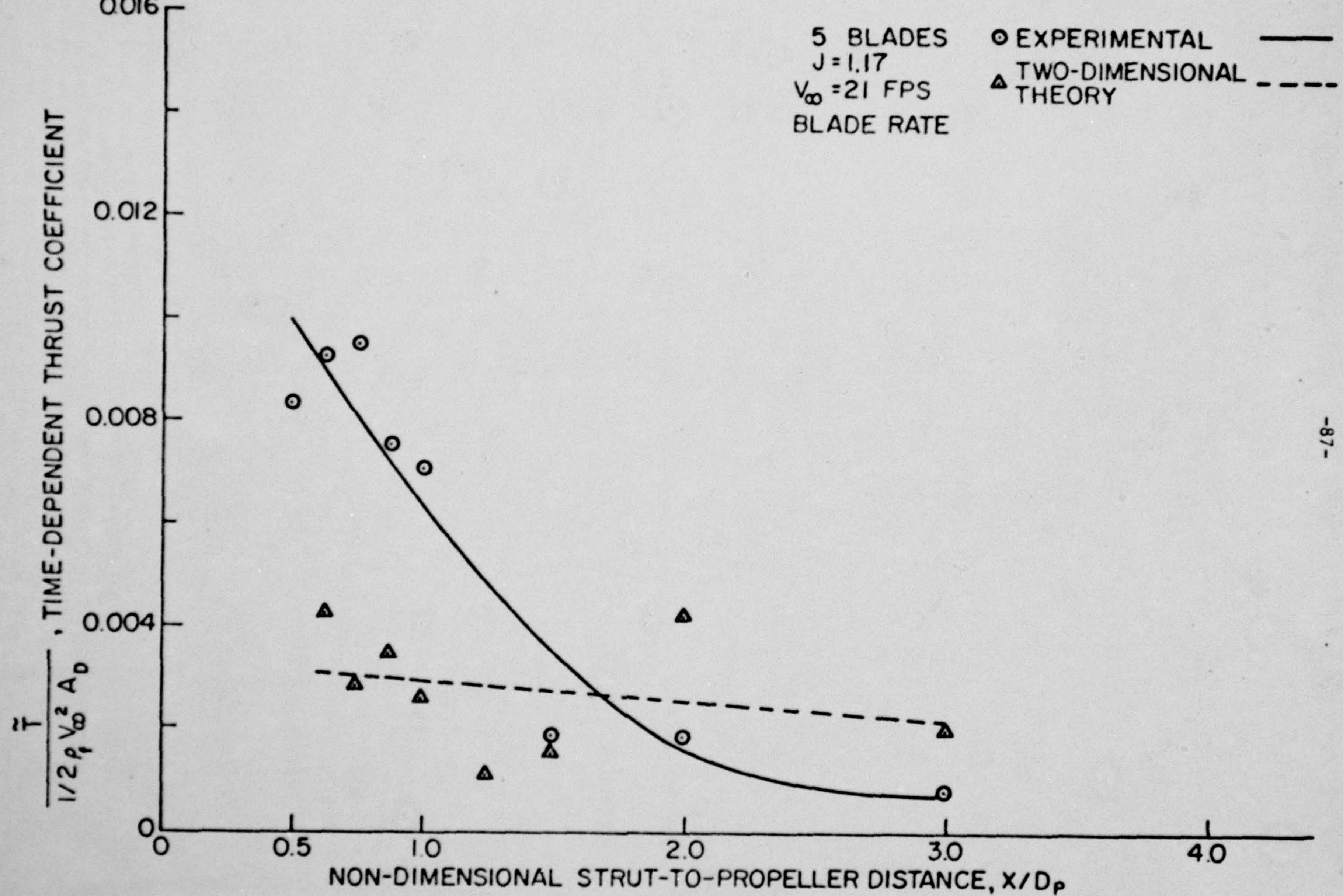

Figure 41 - Single-Amplitude Time-Dependent Thrust Coefficient versus Strut-to-Propeller Distance for Five-Bladed Propeller, J = 1.17, V_∞ = 21 fps

July 10, 1972
DET:mac

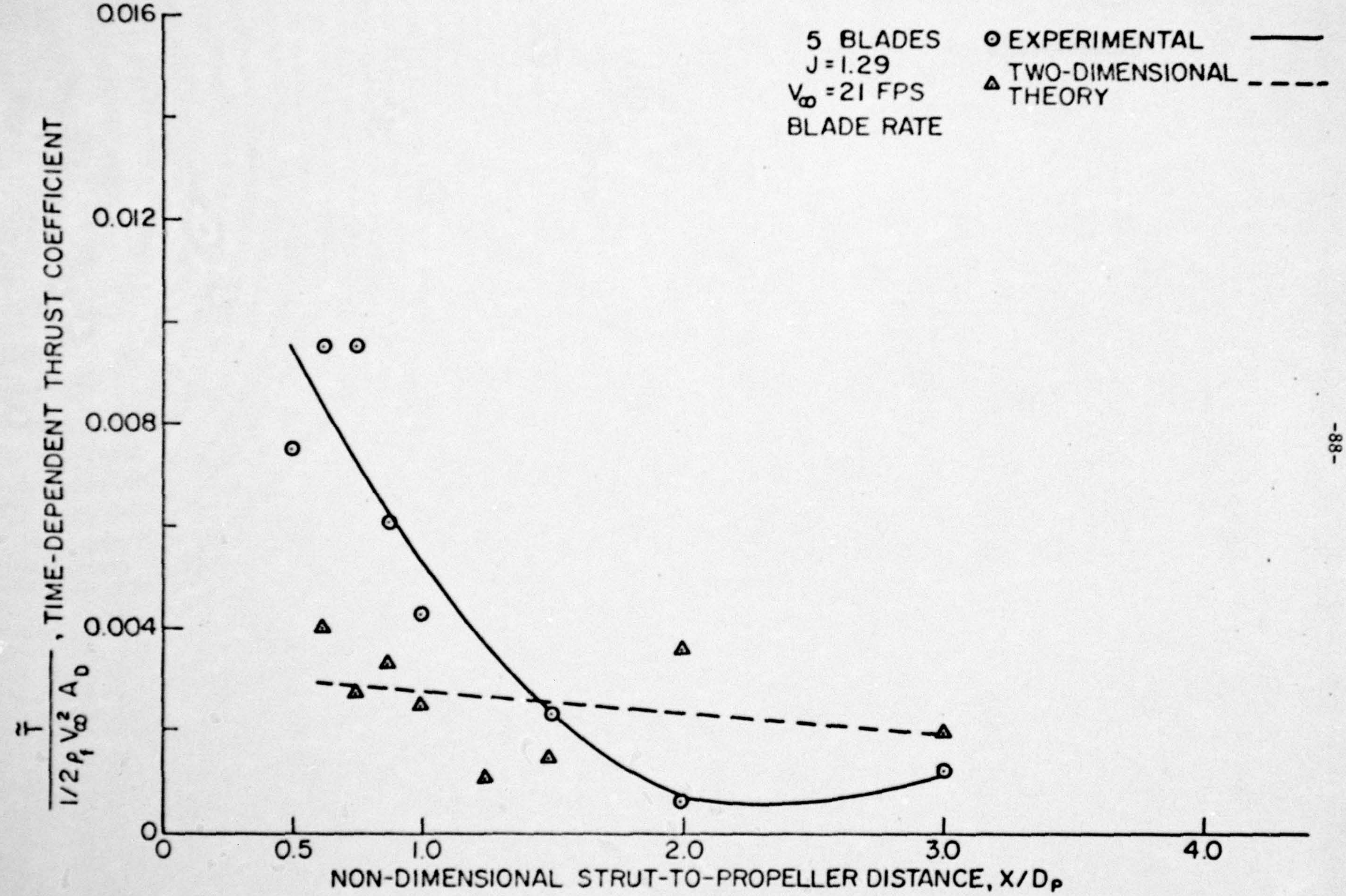

Figure 42 - Single-Amplitude Time-Dependent Thrust Coefficient versus Strut-to-Propeller Distance for Five-Bladed Propeller, $J = 1.29$, $V_\infty = 21$ fps

July 10, 1972
DET:mac

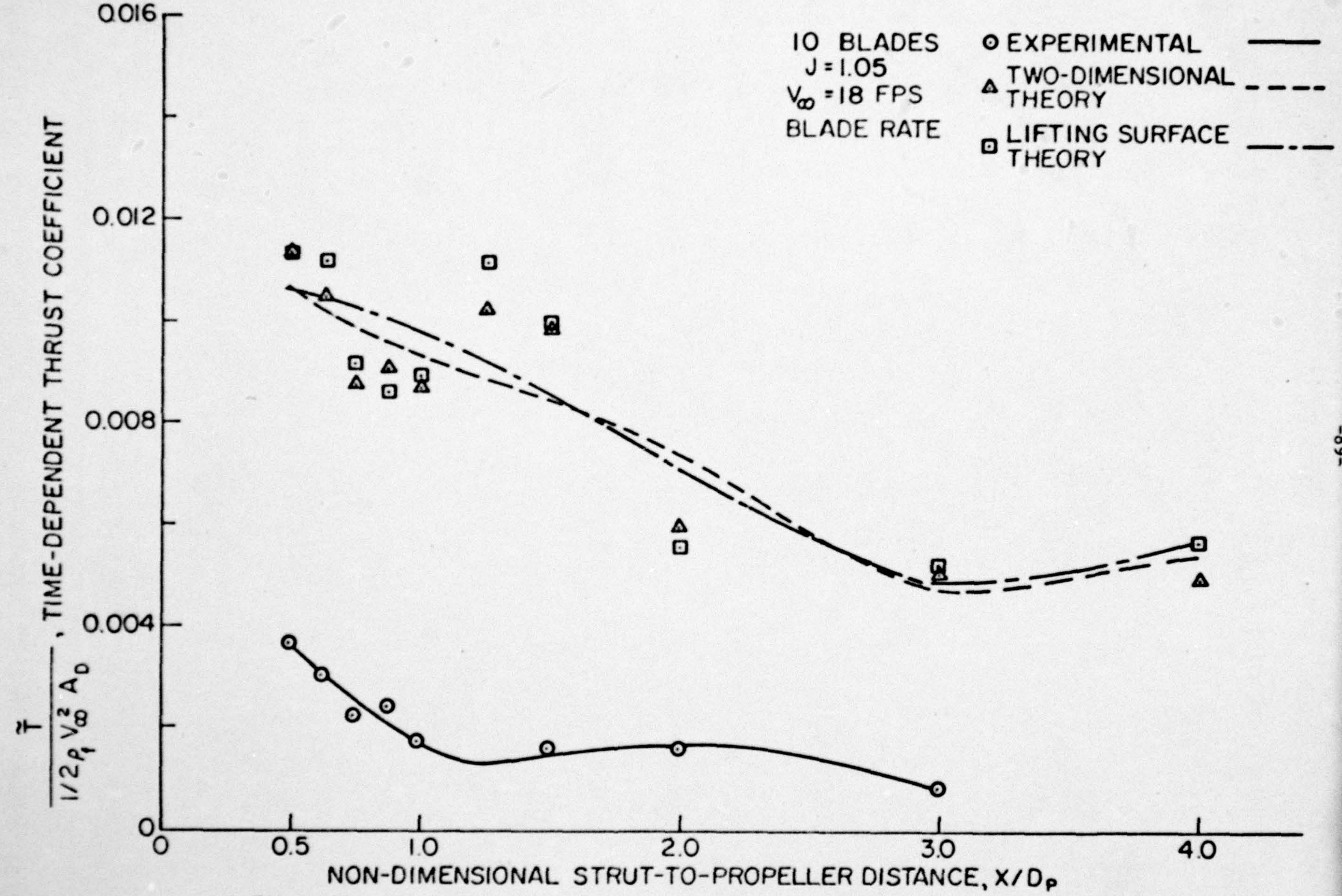

Figure 43 - Single-Amplitude Time-Dependent Thrust Coefficient versus Strut-to-Propeller Distance for Ten-Bladed Propeller, J = 1.05, V_∞ = 18 fps

July 10, 1972
DET:mac

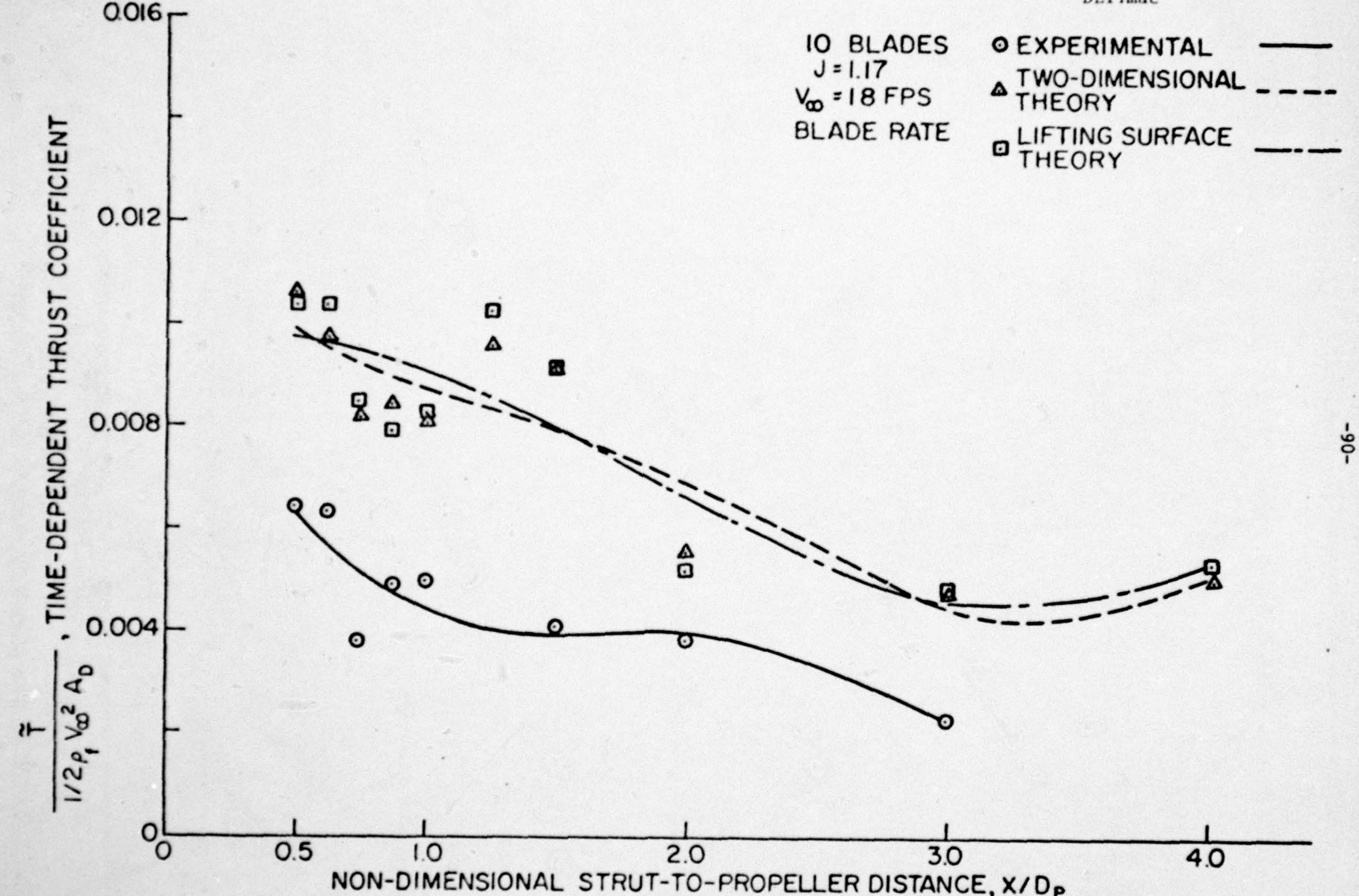

Figure 44 - Single-Amplitude Time-Dependent Thrust Coefficient versus Strut-to-Propeller Distance for Ten-Bladed Propeller, J = 1.17, V_∞ = 18 fps

July 10, 1972
DET:mac

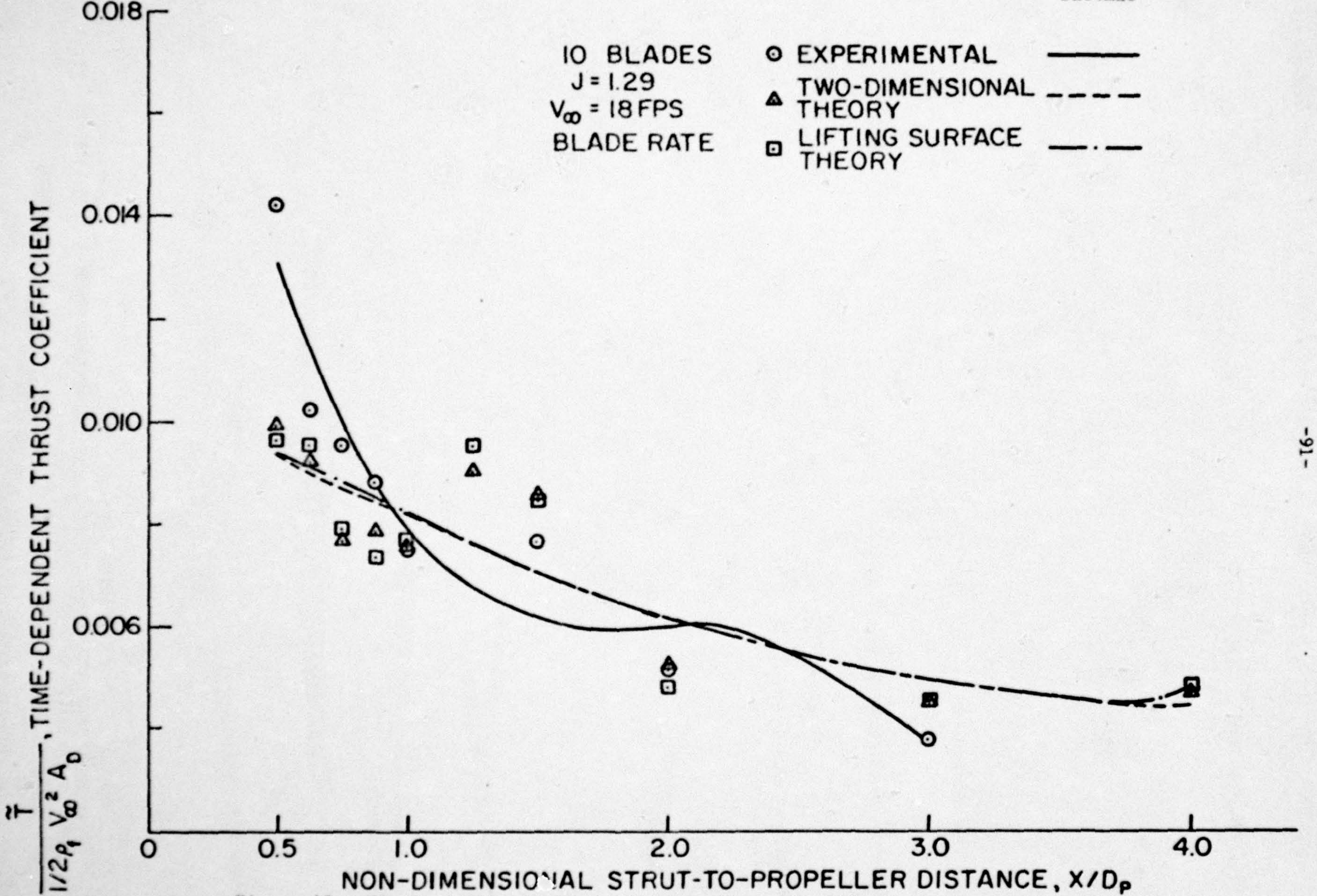

Figure 45 - Single-Amplitude Time-Dependent Thrust Coefficient versus Strut-to-Propeller Distance for Ten-Bladed Propeller, J = 1.29, V_∞ = 18 fps

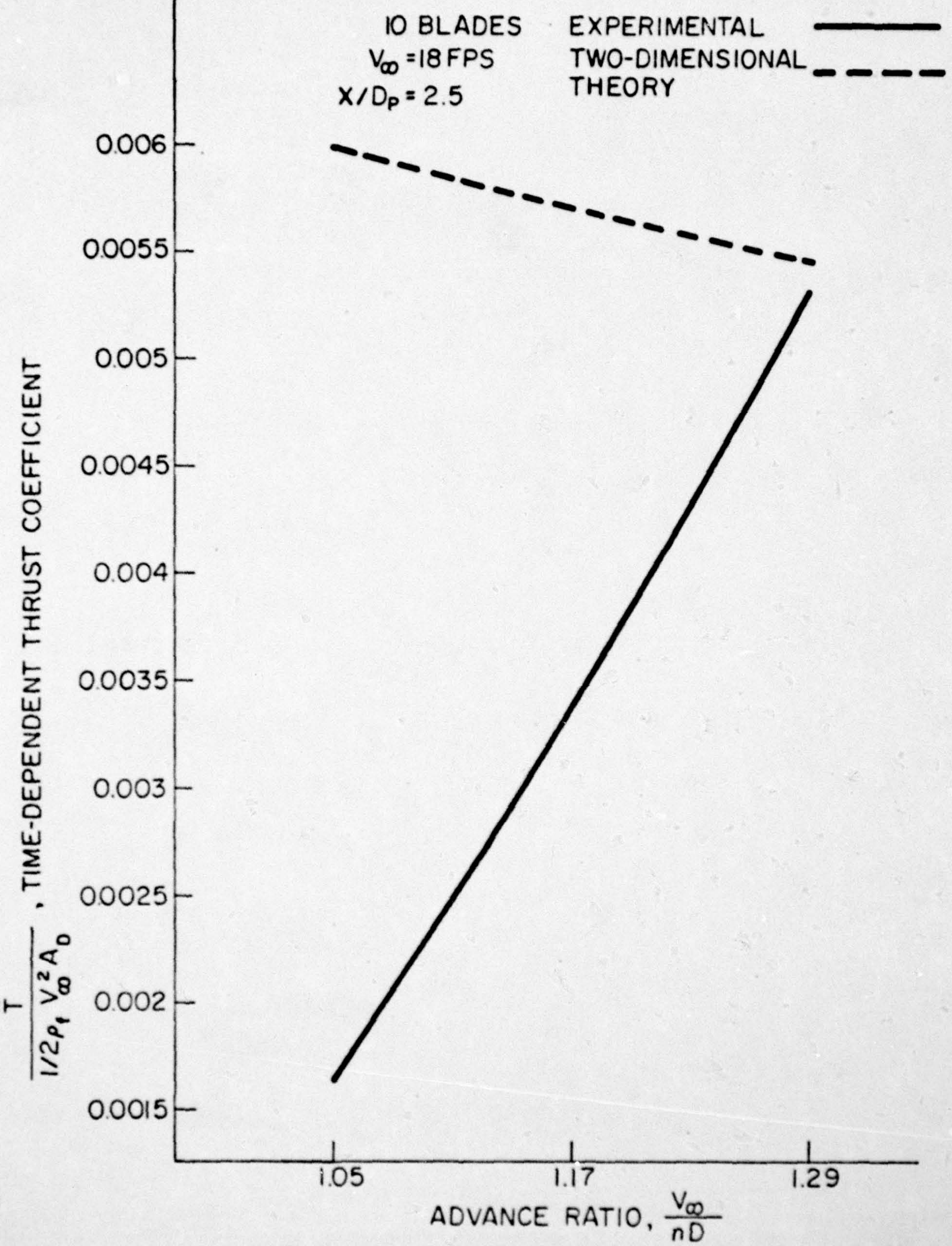

Figure 46 - Single-Amplitude Time-Dependent Thrust Coefficient versus Advance Ratio for Ten-Bladed Propeller, $X/D_p = 2.5$, $V_\infty = 18$ fps

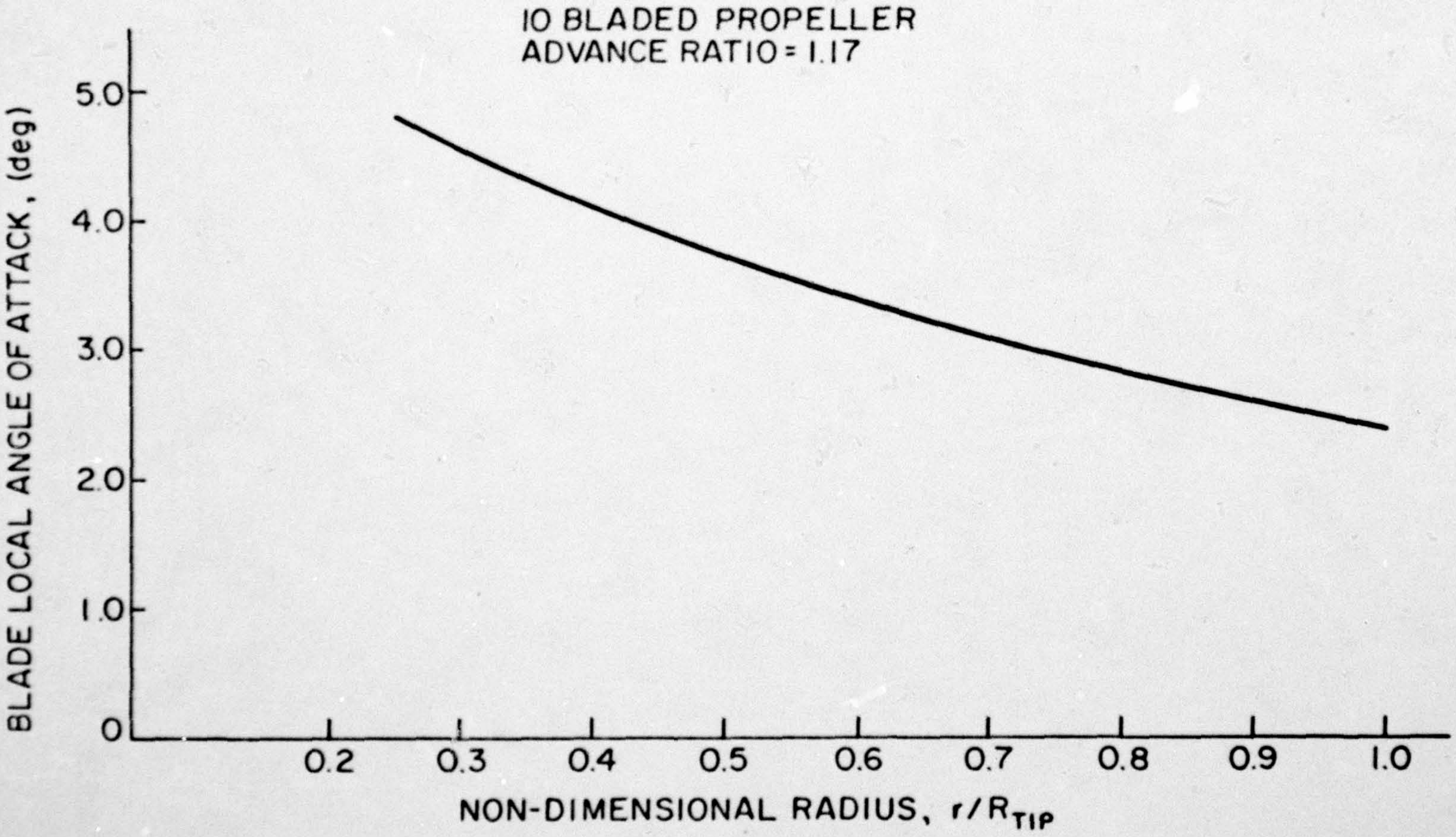

Figure 47 - Local Angle of Attack of Blades on Ten-Bladed Propeller at $J = 1.17$ versus Non-Dimensional Radius

AD-A077 336   PENNSYLVANIA STATE UNIV UNIVERSITY PARK ORDNANCE RES--ETC F/G 20/4
MEASUREMENT OF TIME-DEPENDENT PROPELLER THRUST AND CORRELATION --ETC(U)
JUL 72 D E THOMPSON   N00017-70-C-1407
UNCLASSIFIED TM-72-116   NL

2 OF 2
AD-
A077336

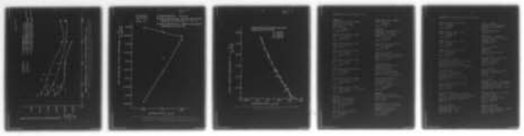

END
DATE
FILMED
12-79
DDC

July 10, 1972
DET:mac

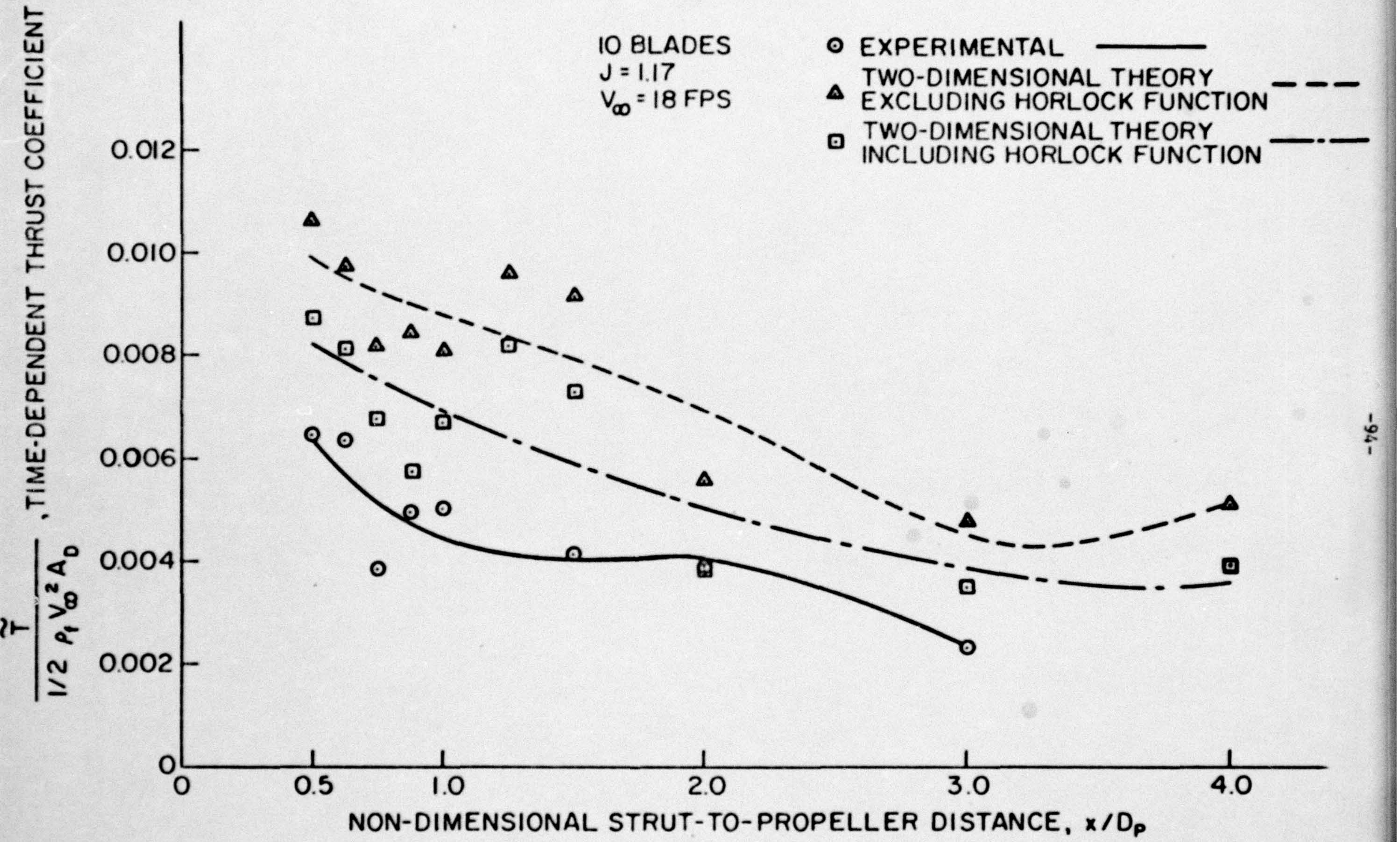

Figure 48 - Single Amplitude Time-Dependent Thrust Coefficient versus Strut-to-Propeller Distance for Ten-Bladed Propeller, $J = 1.17$, $V_\infty = 18$ fps, showing Effect of Velocity Fluctuations Parallel to Blades

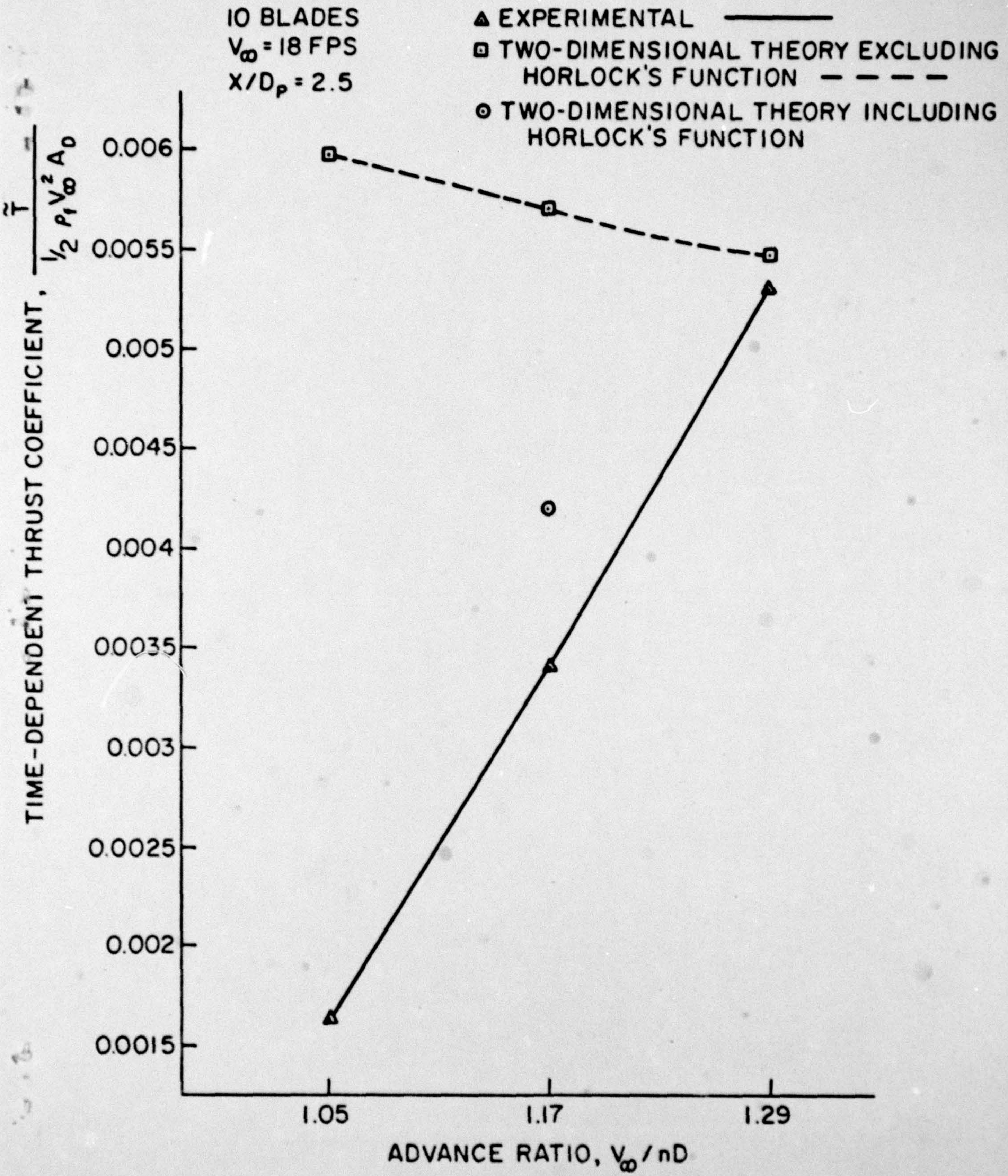

Figure 49 - Single-Amplitude Time-Dependent Thrust Coefficient versus Advance Ratio for Ten-Bladed Propeller, X/D_p = 2.5, V_∞ = 18 fps, showing Effect of Velocity Fluctuations Parallel to Blades

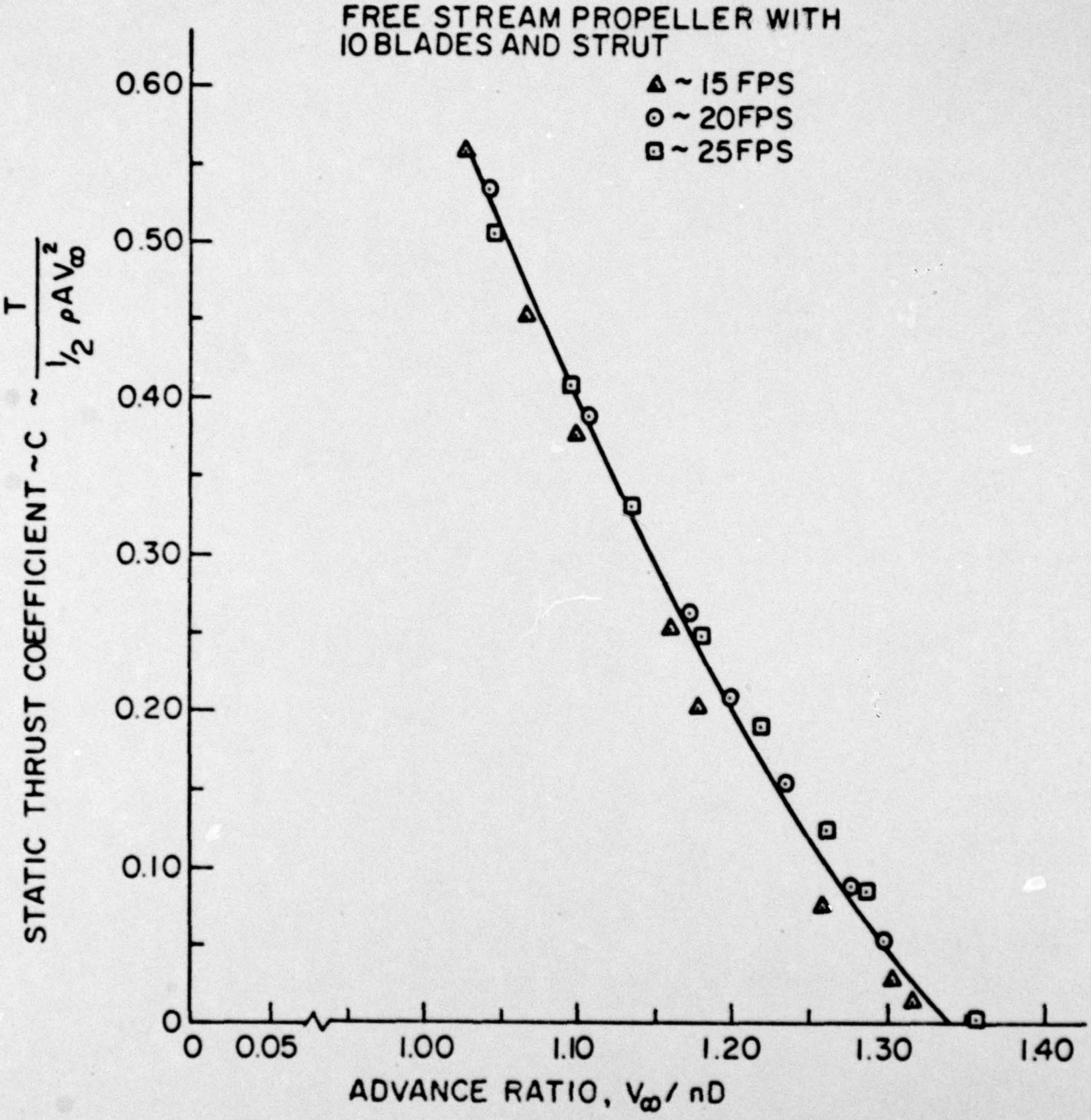

Figure 50 - Static Thrust Coefficient versus Advance Ratio for Ten-Bladed Propeller with Upstream Strut

DISTRIBUTION LIST FOR UNCL TM 72-116

Commander
Naval Ordnance Systems Command
Department of the Navy
Washington, D. C. 20360
Attn: Library
Code ORD-632
(Copies 1 and 2)

Naval Ordnance Systems Command
Attn: S. R. Marcus
Code ORD-03A
(Copy No. 3)

Naval Ordnance Systems Command
Attn: Code ORD-034B
(Copy No. 4)

Naval Ordnance Systems Command
Attn: T. E. Peirce
Code ORD-035B
(Copy No. 5)

Naval Ordnance Systems Command
Attn: G. R. Moltrup
Code ORD-54
(Copy No. 6)

Naval Ordnance Systems Command
Attn: O. Seidman
Code ORD-035
(Copy No. 7)

Naval Ordnance Systems Command
Attn: Chief Technical Analyst
Code ORD-05121
(Copy No. 8)

Naval Ordnance Systems Command
Attn: Chief Analyst, J. J. Bellaschi
Code ORD-03B
(Copy No. 9)

Commander
Naval Ship Systems Command
Department of the Navy
Washington, D. C. 20360
Attn: A. R. Paladino
DIV 037
(Copy No. 10

Naval Ship Systems Command
Attn: R. Sherwood
DIV 037
(Copy No. 11)

Naval Ship Systems Command
Attn: Library
Code 2052
(Copy No. 12)

Commander
Naval Ship Engineering Center
Department of the Navy
Washington, D. C. 20360
Attn: W. L. Louis
Code 6136B
(Copy No. 13)

Naval Ship Engineering Center
Attn: R. M. Petros
Code 6148
(Copy No. 14)

Commanding Officer
Naval Underwater Systems Center
Newport, Rhode Island 02840
Attn: J. F. Brady
(Copy No. 15)

Officer-in-Charge
Naval Undersea Research &
Development Center
Pasadena Laboratory
3202 E. Foothill Boulevard
Pasadena, California 91107
Attn: J. W. Hoyt (Copy No. 16)

Naval Undersea Research &
Development Center
San Diego Laboratory
San Diego, California 92132
Attn: A. G. Fabula
Code 6005
(Copy No. 17)

Commander
Naval Ordnance Laboratory
Silver Spring, Maryland 20910
Attn: Library
(Copy No. 18)

Commanding Officer & Director
Naval Ship Res. & Dev. Center
Department of the Navy
Bethesda, Maryland 20034
Attn: J. B. Hadler
Code 520
(Copy No. 19)

DISTRIBUTION LIST FOR UNCL TM 72-116 (Cont'd)

Naval Ship Res. & Dev. Center
Attn: W. Morgan
Code 526
(Copy No. 20)

Naval Ship Res. & Dev. Center
Attn: M. Strasberg
Code 901
(Copy No. 21)

Naval Ship Res. & Dev. Center
Attn: M. Sevik
Code 019
(Copy No. 22)

Naval Ship Res. & Dev. Center
Attn: R. W. Brown
Code 1942
(Copy No. 23)

Dr. Hsuan Yeh, Director
Towne School of Civil & Mech. Engrg.
University of Pennsylvania
Room 113 Towne, 220 S. 33rd Street
Philadelphia, Pa. 19104 (Copy No. 24)

Dr. Frank Carta
Supervisor, Aeroelastics
United Aircraft Corporation
400 Main Street
E. Hartford, Connecticut 06108
(Copy No. 25)

U. S. Naval Post Graduate School
Monterey, California
Attn: Library
(Copy No. 26)

Dr. A. J. Acosta
Professor of Mechanical Engineering
Division of Engineering & Applied Science
California Institute of Technology
Pasadena, California 91109
(Copy No. 27)

Mr. M. J. Hartmann
NASA Lewis Research Center
21000 Brookpark Road
Cleveland, Ohio 44135
(Copy No. 28)

Dr. C. L. Morfey
Lecturer in Noise Research
University of Southampton
ISVR
Southampton, England
(Copy No. 29)

Professor J. H. Horlock
SRC Turbomachinery Laboratory
Madingley Road
Cambridge, England
(Copy No. 30

Dr. J. D. Van Manen
Haagsteeg 2
Postbox 28
Wageningen, Netherlands
(Copy No. 31)

National Physical Laboratory
Teddington, Middlesex
Feltham, England
Attn: Dr. H. Ritter
(Copy No. 32)

Mr. A. Mitchell
Admiralty Research Laboratory
Teddington, Middlesex,
England
(Copy No. 33)

Dr. P. Leehey
Department of Naval Architecture
Massachusetts Inst. of Technology
77 Massachusetts Avenue
Cambridge, Massachusetts 02139
(Copy No. 34)

Stevens Institute of Technology
711 Hudson Street
Castle Point Station
Hoboken, New Jersey 07030
Attn: S. Tsakonas
(Copy No. 35)

Hamilton Standard
United Aircraft Corp.
Windsor Locks, Connecticut 06096
Attn: Mr. George Rosen
(Copy No. 36)